UNIVERSITÀ DEGLI STUDI DI MILANO

Department of Physics

PhD School in
Physics, Astrophysics and Applied Physics
Cycle XXXIII

Analysis of the STRIP optical system for CMB polarization measurements

Disciplinary Scientific Sector FIS/05

PhD Thesis of:
Sabrina Realini

Director of the School: Prof. Matteo Paris

Supervisor of the Thesis: Prof. Aniello Mennella

Co-supervisor of the Thesis: Dr. Cristian Franceschet

Academic Year 2019-2020

Referees of the thesis:

External Referee:
Dr. Maura SANDRI

External Referee:
Dr. Hiroaki IMADA

Commission of the final examination:

External Member:
Prof. Tomotake MATSUMURA

External Member:
Prof. Bruno MAFFEI

Internal Member:
Prof. Marco BERSANELLI

Final examination:

November 18th, 2020

Università degli Studi di Milano, Dipartimento di Fisica, Milano, Italy

Cover illustration:

Teide Obervatory, Tenerife

MIUR subjects:

FIS/05 - Astronomy and Astrophysics

PACS:

95.55.-n Astronomical and space-research instrumentation

Contents

List of Figures

List of Tables

Introduction

Motivation

Our current understanding of the evolution of the Universe is based on the Hot Big Bang model, which has been so successful that it has become known as the standard cosmological model. Even if cosmology is still far from its aim of understanding the entire Universe and all its contents, it is a fact that recent years have seen astonishing progress towards answering many of the most fundamental questions about the constitution of the Universe. Especially, the study of the Cosmic Microwave Background (CMB) represents one of the most powerful tools in cosmology. Together with the expansion of the Universe and the abundance of light elements, the CMB represents a further confirmation of the Hot Big Bang theory and, through the measurement of its temperature anisotropies, we have been able to establish the value of cosmological parameters with high precision.

Besides its temperature anisotropies, the CMB provides an even more powerful tool: its polarization anisotropies. Nowadays, the detection B-mode polarization anisotropies on large angular scales in the Cosmic Microwave Background polarization pattern is one of the major challenges in observational cosmology, since it would give us an important evidence in favor of the inflationary paradigm and would shed light on the physics of the very early Universe.

Unfortunately, the amplitude of this signal is very low, at the level of fraction of μK. For this reason, the detection requires high sensitivity instruments with tens of thousands of detectors, a rigorous control of systematic effects and a very precise knowledge of the foreground polarized emission produced by our own Galaxy.

After the discovery of the CMB anisotropies by the NASA satellite COBE and the first measurement of its polarized signal by DASI in 2002, several ground-based and balloon-borne experiments have been set up with the purpose of measuring the anisotropies at sub-degree angular scales, by using dedicated reflecting telescopes and interferometer techniques. Even two space missions have been devoted to the observation of CMB polarization. In particular, the Planck Collaboration released full sky polarized maps in seven frequency bands from 30 to 353 GHz, which allowed the reconstruction of the CMB E-modes power spectrum. However, the observation of the CMB anisotropies is far from being an easy task: their extremely weak signal is buried in the noise of both terrestrial and astrophysical origin.

Among the upcoming polarization experiments we find the Large Scale Polarization Explorer (LSPE), a mission devoted to the observation of the CMB polarization on large angular scales, with two independent instruments: the Strip ground-based telescope, observing at 44 GHz, plus a 95 GHz channel for atmospheric measurements, and the SWIPE balloon-borne mission, observing at 145, 220 and 240 GHz during a night Arctic stratospheric long-duration flight.

Besides limiting the ratio of tensor to scalar ratio perturbation amplitudes down to $r = 0.03$, at 99.7% confidence level, LSPE will produce wide maps of foreground polarization generated by synchrotron and interstellar dust emissions in our Galaxy, which will be important to map the Galactic magnetic fields and to study the ionized gas and the diffuse interstellar dust.

Thesis overview

This thesis has been carried out in the context of the development of the Strip instrument and I focused my work mainly on its optical system. Strip is a coherent polarimeter array that will observe the microwave sky from the Teide Observatory in Tenerife in two frequency bands centred at 43 GHz (Q-band, 49 receivers) and 95 GHz (W-band, 6 receivers) through a dual-reflector crossed-Dragone telescope of 1.5 m projected aperture.

CMB polarization experiments like Strip require the use of several feedhorns to obtain high sensitivity measurements and to observe the sky with a sub-degree angular resolution a telescope must be used. Owing to the small amplitude of the CMB anisotropies, an accurate control of systematic effects is necessary to perform high precision measurements. A detailed characterization of the optical system is mandatory, since the optics is one of the major limiting factors, as aberrations of the main beam and sidelobes are two of the main sources of systematic errors. Main beam distortions degrade the angular resolution, limiting the reconstruction of the anisotropy power spectrum at high multipoles, while sidelobes drive unwanted radiation not coming from the boresight direction into the feedhorn (the so-called straylight), contaminating the measurement mainly at large and intermediate angular scales.

Accurate predictions and measurements of the beam shape are essential both during the instrument development phase (to design and positioning properly each feedhorn) and for an in-depth knowledge of the whole-instrument response in the development of the data reduction pipeline to remove systematic effects.

Nowadays, several electromagnetic simulation methods are available, like Physical Optics, Physical Theory of Diffraction, Geometrical Optics, and Geometrical Theory of Diffraction. These methods are widely used to perform robust electromagnetic simulations and can be used for beam prediction of real optical systems. However, when we consider multiple reflections and diffraction between optical elements (reflectors, shields, supporting structures) simulation time can increase exponentially. To overcome this difficulty, an advanced simulation technique based on Geometrical Theory of Diffraction can be used.

The major result of this thesis is the set up of a realistic electromagnetic model of the Strip optical system, which includes the feedhorns in Q- and W-bands, the mirrors, the shielding structure, the IR-filters and the cryostat window. I characterized the performance of the Strip optical system with several steps: (i) main beams analysis taking into account the effect of the IR filters and cryostat window, (ii) modelling and study of the effect of mirrors imperfections, (iii) sidelobes analysis with the effect of the shielding structure, (iv) analysis of the effect of the introduction of a forebaffle and an absorber inside the shielding structure.

An in-depth analysis has been performed in order to characterize the main beam response in terms of angular resolution, ellipticity, cross-polarization level and directivity. Main beam parameters have been verified also in the frequency band and after the introduction of mirrors surface distortions, showing no unexpected degradation in performance.

By means of the Multi–reflector GTD method of GRASP, I have studied also the sidelobes, identifying their major contributions, i.e. sequence of reflections or diffractions. I found that the optics response features at large angles from the beam centre are determined mainly by the rays coming directly from the feedhorn (considered as the source of radiation) and from multiple reflections inside the shielding structure.

Besides the optical simulation activity, I also performed radiation pattern measurements of the six W-band feedhorn in the anechoic chamber of the Physics Department at the University of Milan. I compared all measurements to simulations in order to assess compliance to design requirements.

The implementation of a realistic electromagnetic model of the Strip telescope is essential to assess the impact of the optical response on observations, which I did for four representative channels. I studied the systematic effect of the "effective main beam", defined as the average of all optical beams (those computed with GRASP) that cross a given pixel of the sky map, given the Strip scanning strategy and their actual orientation. The convolution of the effective beams with the true CMB sky produce the observed sky map and we can capture the difference between the true and observed angular power spectra of the sky, both in temperature and polarization.

I have also been involved in a project for the study of possible application of machine learning techniques for the prediction of the main beam parameters of an optical system. If applicable, this would be useful in the case of densely populated focal planes, for which is not feasible an accurate simulation for each receiving antenna. The very first results are briefly reported in Appendix D.

Organizational note

This thesis consists of five Chapters and four Appendices. The first two chapters are introductory and explain the scientific background in which this thesis has been developed. The remaining chapters have the aim to describe the work that I have done in the last three years in the context of the Strip instrument development.

Chapter 1: A brief history of cosmology. In the first chapter, I review the basis of standard cosmology, from the first observations made by Hubble to the discovery of the Cosmic Microwave Background. The main characteristics of the CMB and its temperature and polarization anisotropies are discussed, together with the physical mechanisms of anisotropy formation and the phenomenology of the power spectrum. I also describe the main problems within the Hot Big Bang model and I show how the concept of inflation can solve them.

Chapter 2: The LSPE/STRIP instrument. I introduce the "Large Scale Polarization Explorer" (LSPE) experiment and describe the Strip instrument. Then, I give an introduction to the electromagnetic design of the STRIP telescope, followed by a description of all its optical elements.

Chapter 3: Strip main beams. I report the result of the electromagnetic characterization of the W-band feedhorns. Then, I present the main beam simulations of the optical system taking into account the effect of the IR filters and the cryostat window. At the end of the chapter, I report the analysis of the effect of surface distortions on the telescope mirrors.

Chapter 4: Strip sidelobes. I present the analysis of the telescope sidelobes and the effect of the introduction of a forebaffle. The chapter continues with the analysis of how the radiation pattern is modified with the addition of an absorber inside the shielding structure.

Chapter 5: Impact on observations. In this section, I study the effects of the Strip optics on observations by means of the Strip LevelS pipeline. The result is a first conjecture of the effect of the optical response.

Appendix A: Optics concepts. I briefly summarize some definitions and concepts concerning parameters that are used to describe optical systems.

Appendix B: GRASP simulation software. I present the tool used throughout this thesis to compute the electromagnetic radiation produced by systems consisting of multiple reflectors with several feedhorns.

Appendix C: Zernike polynomials. I report a brief review of Zernike polynomials, which have been used to describe mirror distortions.

Appendix D: Machine learning applications. In this appendix, I report the early promising results obtained on a possible application of neural networks for the prediction of main beam parameters.

CHAPTER 1

A brief history of cosmology

This chapter takes us to the beginning of the last century, when the idea of a non-static Universe began to take shape, together with those brilliant insights that revolutionized the way we understand and describe the Universe. From the first observations of the "distant nebulae" to the discovery of the Cosmic Microwave Background, we briefly review the history of modern cosmology.

1.1 The standard cosmological model

Our modern picture of the Universe dates back to 1924, when the American astronomer Edwin Hubble showed that our Galaxy was not the only one, but there are many others. Even before observations with telescopes, it had been realized that there were "nebulous" objects with a diffuse appearance different from the stars, but Hubble was the first to determine the distances to nine of these different objects using the indirect methods of Cepheid variables. In the years following the demonstration of the existence of other galaxies, Hubble spent his time cataloging their distances and observing their spectra. At that time most people expected galaxies to be moving randomly, and so it was a surprise to find that most galaxies appeared red-shifted, which means that nearly all of them were moving away from us.

In 1929, Hubble made his second fundamental contribution to cosmology: he showed that the velocity v of a receding galaxy is not random, but is directly proportional to the distance d of the galaxy from us (see Fig. 1.1). In other words, the farther a galaxy is, the faster it is moving away. The velocity-distance relation

$$v = H_0\, d \tag{1.1}$$

is known as *Hubble's law* and H_0 is called *Hubble's constant* (Hubble 1929). The consequence of this observation is that the Universe cannot be static, but it is expanding, and the distance between the different galaxies is continuously changing.

This observation was one of the predictions of the general theory of relativity formulated by Einstein in 1915, a theory that enables the construction of self-consistent models of the Universe. Einstein's field equations contain solutions in which the Universe is uniformly expanding; however, he was so sure that the Universe had to be static that he modified his theory to make this possible, introducing a so-called cosmological constant into his equations. As a consequence, in Einstein's model the Universe is static, closed and has isotropic spherical geometry.

In 1922, the Russian physicist and mathematician Alexander Friedmann tried to explain the prediction of a non static Universe. He found solutions that are still isotropic

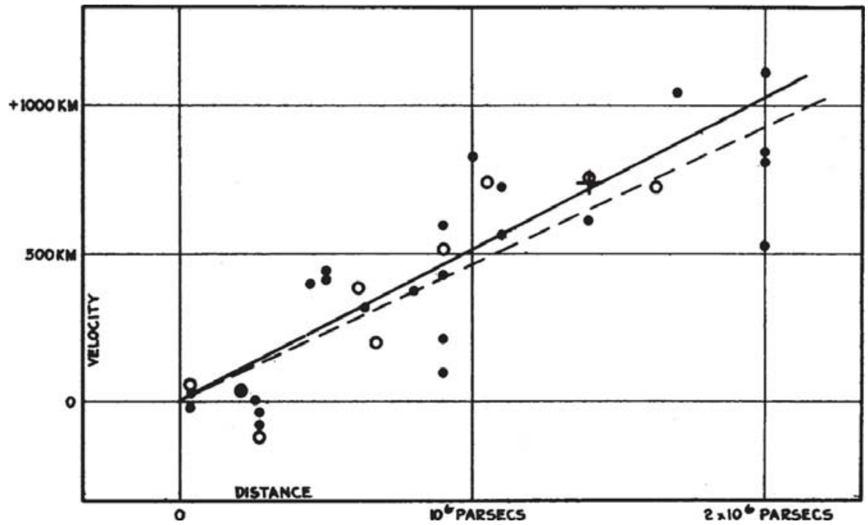

Figure 1.1: Hubble's velocity-distance relation for nearby galaxies (Hubble 1929).

models, but they are expanding solutions and include both spherical and hyperbolic geometries (Friedman 1922) . These solutions correspond to the standard world models of general relativity and are known as Friedman models.

The starting point for the construction of cosmological models is to assume that the Universe is isotropic and homogeneous and that we are not located at any special location in the Universe. This is known as the *cosmological principle*. As a consequence of this principle, any other observer located anywhere in the Universe at the same cosmic epoch would observe the same large-scale features that we observe. Under this assumption, we can define a set of fundamental observers, who move in such a way that the Universe always appears isotropic to them. Each observer measures a proper time τ, also called cosmic time.

We can see how coordinates change in a uniformly expanding Universe. The definition of a uniform expansion is that between two cosmic epochs, τ_1 and τ_2, the distances of any two fundamental observers, i and j, change such that

$$\frac{x_i(\tau_1)}{x_i(\tau_2)} = \frac{x_j(\tau_1)}{x_j(\tau_2)} = \text{constant} = \frac{a(\tau_1)}{a(\tau_2)}. \tag{1.2}$$

In the last term, $a(\tau)$ is a universal function, known as the *scale factor*, which describes how the relative distances between any two fundamental observers change with cosmic time τ. We can set $a(\tau) = 1$ at the present epoch τ_0 and let the value of x at the present epoch be r, so that we can rewrite Eq. (1.2) as

$$x(\tau) = a(\tau)\, r. \tag{1.3}$$

According to this equation, the variation of the proper distance in the expanding Universe depends on the scale factor $a(\tau)$ and the term r is called comoving distance. Robertson and Walker were the first to derive the metric of space-time for all isotropic, homogeneous, uniformly expanding models of the Universe (Robertson (1935); Walker (1937)). We can write the *Robertson-Walker metric* as

$$ds^2 = c^2 d\tau^2 - a(\tau)^2\, [dr^2 + f_k(r)^2\, (d\theta^2 + \sin^2\theta\, d\phi^2)]. \tag{1.4}$$

The metric enables us to define the invariant interval ds^2 between events at any epoch or location in the expanding Universe. It contains the unknown function $a(t)$, which describes the dynamics of the Universe, and an unknown constant k which describes its spatial curvature.

It can be demonstrated that the only isotropic curved spaces are those in which the two-dimensional curvature of any space section is constant through the space and can take positive, zero or negative values, corresponding to spherical, flat and hyperbolic spaces respectively (Wald 1984). Hence, we can write:

$$f_k(r) = \begin{cases} r & \text{if } k = 0 \\ 1/\sqrt{k}\, \sin(\sqrt{k}r) & \text{if } k > 0 \\ 1/\sqrt{k}\, \sinh(\sqrt{k}r) & \text{if } k < 0 \end{cases} \tag{1.5}$$

We can also define the *cosmological redshift* as the shift of spectral lines to longer wavelengths associated with the isotropic expansion. If λ_e is the wavelength of the line as emitted and λ_0 the observed wavelength, the redshift z is defined to be

$$z = \frac{\lambda_0 - \lambda_e}{\lambda_e} = \frac{1}{a(\tau_e)} - 1. \tag{1.6}$$

From Eq. (1.6) we see that the redshift is a measure of the scale factor of the Universe when the radiation was emitted by the source. One important consequence is that we can derive an expression for the comoving radial distance coordinate r as

$$r = \int_{\tau_1}^{\tau_0} \frac{c\, d\tau}{a(\tau)}. \tag{1.7}$$

In terms of proper distance, Hubble's law can be written as $v = \frac{dx}{d\tau} = Hx$. We write H rather than H_0 in Hubble's law since a Hubble's constant H can be defined at any epoch. Substituting $x(\tau) = a(\tau)\, r$, we find that

$$H(\tau) = \frac{\dot{a}(\tau)}{a(\tau)}. \tag{1.8}$$

Hubble's constant at the present time H_0 defines the present expansion rate of the Universe.

According to general theory of relativity, space and time are dynamic quantities: the presence of matter affects the curvature of the space-time and, in turn, matter moves along trajectories in bent space-time (Einstein 1915). This is described by Einstein's field equation

$$G_{\mu\nu} = -\frac{8\pi G}{c^2} T_{\mu\nu}, \tag{1.9}$$

where $T_{\mu\nu}$ is the energy-momentum tensor and $G_{\mu\nu}$ is Einstein's tensor, which is defined starting from the metric tensor $g_{\mu\nu}$ which contains all the information about the intrinsic geometry of the space. Eq. (1.9) tells how the components of the metric tensor are related to the mass-energy distribution in the Universe.

The standard cosmological model is based on solving Einstein's field equation under the assumptions of isotropy and homogeneity. We get a set of equations referred to as *Friedman's equations*

$$\left(\frac{\dot{a}}{a}\right)^2 = \frac{8\pi G}{3}\rho - kc^2 \tag{1.10}$$

$$\frac{\ddot{a}}{a} = -\frac{4\pi G}{3}\left(\rho + \frac{3P}{c^2}\right) \tag{1.11}$$

where ρ is the total mass density content of the Universe and P is the associated total pressure. Eqs. (1.10) and (1.11) show that with the condition $\rho > 0$ the Universe cannot be static: if $k = 0$ or $k < 0$, then we always have $\dot{a}(\tau)^2 > 0$; while, if $k > 0$, we have only one value of τ for which $\dot{a}(\tau) = 0$. This is an inversion point between expansion and contraction (or vice versa).

In order to make these equations solvable and describe the dynamics of the Universe, we need to define also the equation of state $P(\rho)$ for each component we consider, so that we can derive $a(\tau)$. A powerful approximate model for the energy content of the Universe is to divide it into pressureless matter (baryonic and dark matter), radiation and vacuum energy (dark energy). This last component is related to the introduction of a cosmological constant in Friedman's equations, which takes into account the current evidence of the accelerated expansion of the Universe. Under this assumptions, the equation of state has the generic form

$$P(\rho) = w\rho c^2, \qquad \text{where } w = \begin{cases} 0 & \text{matter} \\ 1/3 & \text{radiation} \\ -1 & \text{dark energy} \end{cases} \tag{1.12}$$

We can then find the variation of the density with the scale factor using the relativistic energy conservation equation

$$\frac{d\rho}{da} + 3\left(\rho + 3\frac{P}{c^2}\right)\frac{1}{a} = 0. \tag{1.13}$$

Hence, substituting Eq. (1.12) and integrating, the variation of the density with the scale factor for each component is

$$\rho = \rho_0 a^{-3(1+w)}. \tag{1.14}$$

In the case of cold matter, $w = 0$ and so $\rho \propto a^{-3}$. For photons and ultra-relativistic matter, $w = 1/3$ and so $\rho \propto a^{-4}$. For dark energy, $w = -1$ and $\rho =$ constant. The total density can be written as

$$\rho_{\text{tot}}(a) = \frac{\rho_{m,0}}{a^3} + \frac{\rho_{r,0}}{a^4} + \rho_{\Lambda,0}. \tag{1.15}$$

As we can see, in an expanding Universe, the energy density is initially radiation dominated, than matter dominated and, finally, is dominated by dark energy (see Fig. 1.2).

We get a different evolution of $a(\tau)$ for $k = 0, \pm 1$: a matter or radiation dominated expanding Universe will keep expanding for $k = 0, -1$, with $\dot{a}(\tau \to \infty)|_{k=0} \to 0$. Whereas, if $k = 1$, the initial expansion will be followed by a contraction, ending up in a "Big Crunch" with $a(\tau_{\text{Big Crunch}}) = 0$. On the other hand, a dark energy dominated Universe will keep expanding regardless of the geometry of the space and the expansion will be accelerated ($\ddot{a} > 0$).

Friedmann equation (1.10) can be re-written as

$$\frac{8\pi G}{3H^2(\tau)}\rho_{\text{tot}}(\tau) - \frac{k(\tau)c^2}{a^2(\tau)H^2(\tau)} = 1 \tag{1.16}$$

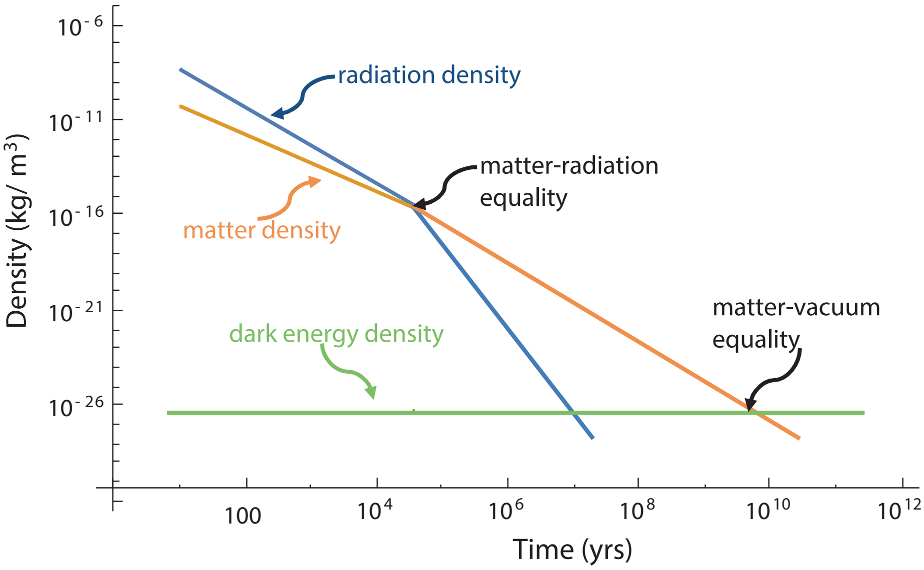

Figure 1.2: The density evolution of the main components of the Universe. The early Universe was radiation-dominated, until the scale factor was enough for matter density to being to dominate. The energy density of dark energy is constant.

and it reveals that there is a direct connection between the density of the Universe and its global geometry. For a given rate of expansion, there is a critical density $\rho_c = \frac{3H_0^2}{8\pi G}$ that will yield $k = 0$. We can conveniently express the density in terms of a critical density and define a density parameter $\Omega_{\text{tot}} \equiv \frac{\rho_0}{\rho_c}$. Substituting in Eq. (1.16), we can explicitly see how the density parameter is related to the spatial curvature

$$k(\tau) = \frac{H^2(\tau)a^2(\tau)}{c^2}\left(\Omega_{\text{tot}}(\tau) - 1\right). \tag{1.17}$$

As a consequence, if $k = 0$ then $\Omega_{\text{tot}} = 1$, if $k > 0$ then $\Omega_{\text{tot}} > 1$, and if $k < 0$ then $\Omega_{tot} < 1$. The density parameter is given by all the cosmological components:

$$\Omega_{\text{tot}} = \Omega_m + \Omega_r + \Omega_\Lambda. \tag{1.18}$$

We can also compute the age of the Universe as

$$\tau_{\text{now}} = \int_0^{\tau_{\text{now}}} d\tau = \int_0^1 \frac{da}{\dot{a}} \simeq \frac{1}{H_0}. \tag{1.19}$$

The parameters H_0, Ω_m, Ω_r, Ω_Λ, which characterize the dynamics of our Universe, are some of the so-called *cosmological parameters* that can be measured with dedicated experiments.

1.2 The early Universe

In 1948 George Gamow realized that, in an expanding Universe, the early stages must have been very hot and the temperature was so high that the dynamics of the expansion were dominated by the energy density of thermal radiation. In the short time-scales available in the hot early phases of the expansion, there was not enough time to synthesize elements heavier than helium. Ralph Alpher and Robert Herman showed that only deuterium, helium-3 and helium-4 were created in significant quantities. They worked out the thermal history of the Universe and predicted that today there should be present in the Universe a diffuse background of blackbody radiation with temperature about 5 K (Alpher & Herman 1948).

1.2.1 Thermal history of the Universe

Because the Universe is expanding, in the past it had to be denser than today. Therefore, if we run the expansion backwards in time the Universe becomes hotter and denser, until we reach the state called Big Bang. George Gamow studied the physics of the early Universe and made many important predictions. The major breakthrough was the realization that the early Universe was not only very dense, but also very hot. This led to two important conclusions. First, there exists a radiation era in the early Universe during which the energy density of radiation exceeds that of matter. Second, this radiation, cooled by the expansion, survives and fills the whole Universe. This radiation is now called the Cosmic Microwave Background Radiation (CMB).

According to current knowledge, when the Universe started its expansion, density and temperature were too high for atoms to exist ($\rho \sim 10^{25}$ g/cm^3 and $T \sim 10^{15}$ K), so that the Universe was a dense sea of free quarks. Structureless particles (quarks, leptons and gluons), all in thermal equilibrium, were continually annihilated and created. What lies before the quark era, when the Universe was younger than 10^{-36} s, is still uncertain because of theoretical and conceptual problems. The question is, how far we can trace the Universe history back in time. If we do not consider quantum phenomena, we obtain a cosmic singularity at zero time when density is infinite. However, we cannot neglect quantum phenomena that occur in strong gravitational fields. Since we do not yet have a complete consistent theory that unifies general relativity and quantum mechanics, very little is known at present about these phenomena.

Few nanoseconds after the Big Bang, as the temperature dropped ($T \sim 10^{12}$ K), the first elementary particles (protons and neutrons) formed. This phase is called quark-hadron transition. At this stage, the Universe was still too hot and dense for neutral atoms or even bound nuclei to exist. The vast amount of radiation in such a hot environment ensured that any atom or nucleus produced would be immediately destroyed by a high energy photon. As a result of the high temperature, interactions among particles occurred much more frequently than they do today. These multiple interactions kept the equilibrium in the electronic and neutrino capture reactions

$$p + e^- \leftrightarrows n + \nu_e$$

$$n + e^+ \leftrightarrows \bar{\nu}_e + p$$

Neutrino capture reactions ended 1 s after the Big Bang, when neutrinos decoupled from the primordial plasma ($T \sim 10^{10}$ K). Hence, we expect today a background of neutrinos at ~ 2 K.

After neutrino decoupling, the electronic capture and neutron β-decay reactions were still in chemical equilibrium. This condition lasted until electrons had enough energy to fill the energy gap between the neutron and proton rest energy, which means $T > 8 \cdot 10^9$ K. After the equilibrium break, the ratio $\frac{n_p}{n_n}$ was fixed at ~ 7, according to Saha equation. This value is the same today and the combined proton plus neutron density is called the baryon density.

Until the photon energy was greater than the rest energy of the electron-positron couple ($T > 5 \cdot 10^9$ K), the reaction

$$2\gamma \leftrightarrows e^+ + e^-$$

was in equilibrium. However, for $T < 5 \cdot 10^9$ K, the complete annihilation of positrons occurred. Because of this reaction, matter warmed up.

As the Universe cooled below the binding energies of typical nuclei, light elements began to form, with the *Big Bang Nucleosynthesis*. When $T \sim 10^9$ K, deuterium could be synthesized through neutron capture ($p+n \leftrightarrows d+\gamma$), and its interactions with protons led to the formation of $^4\mathrm{He}$. Heavier elements could not be produced because the reaction rate became too low. Since we expect the proton-neutron ratio to be 7, we can infer the mass fraction of the light elements produced within the Hot Big Bang model: $\sim 25\%$ He and $\sim 75\%$ H. The current estimates for the light elements abundances are consistent with the predictions.

At this stage, the primordial plasma was made of photons, light nuclei and electrons; however, photons had still enough energy to ionize neutral atoms. The number density of free electrons was so high that the Universe was opaque to photons. This means that the mean free path for photons to Thomson scatter off electrons was extremely short. Consequently, the photons and baryons could be considered as a single tightly coupled fluid.

Only when the temperature dropped far below the one required for hydrogen ionization ($k_B T << 13.6$ eV, that is $T << 10^5$ K) *recombination* took place and photons were free to propagate in a neutral and transparent Universe. Decoupling of photons from matter occurred roughly when the scattering rate of photons on electrons became smaller than the expansion rate, i.e. during recombination and roughly 380000 years after the beginning of expansion.

Because of radiation decoupling, we expect a background of photons, called *Cosmic Microwave Background* (CMB), coming from the so-called last scattering surface at $z \simeq 1100$. This radiation offers us a look at the Universe at the time of decoupling, and so it is a powerful tool for cosmological studies.

We do expect that, at some late time, the electrons were reionized due to the ignition of the first stars and the consequent emission of UV radiation. In fact, the Universe we observe back to redshift $z \sim 6$ appears to be ionized. As we will see, this process, called *reionization*, has an effect on the polarization of the Cosmic Microwave Background.

1.3 The Cosmic Microwave Background

By early 1960s, as the sensitivity of receivers for centimetre wavelengths improved, it became feasible to search for the cool background radiation left over from the early stages of the Universe. The predicted remnant of the Big Bang was discovered accidentally by Arno Penzias and Robert Wilson in 1965 while they were working on a receiver system for centimetre wavelengths at the Bell Telephone Laboratories. They found a diffuse background radiation, which was remarkably uniform over the sky.

At roughly the same time at Princeton University, Bob Dicke and Jim Peebles were also taking an interest in microwaves. They argued that we should still be able to see the glow of the early Universe, because light from very distant parts of it would only just be reaching us now. However, the expansion of the Universe meant that this light should be so greatly red-shifted that it would appear to us now as microwave radiation.

To understand this, we should consider that, from the Big Bang to the recombination, photons were strictly coupled with matter and they were in thermal equilibrium. The numerical density of photons and the spectral radiance were

$$n_r = AT^3, \tag{1.20}$$

$$I_\nu = B_\nu(T) = \frac{2h\nu^3}{c^2}\frac{1}{\exp\left(\frac{h\nu}{k_B T}\right) - 1}, \tag{1.21}$$

where A is a constant and T is the blackbody temperature at thermal equilibrium. Combining Eq. (1.20) with collisionless Boltzmann equation we get

$$AT^3(a) = n_r(a) = \frac{n_{r0}}{a^3} \quad \Longrightarrow \quad T(a) \propto \frac{1}{a} \tag{1.22}$$

which means that $T(a_{\text{now}}) = T(a_{\text{rec}})a_{\text{rec}}$. As a consequence of the expansion, there is also a cosmological redshift that acts on photons according to $\nu(a_{\text{now}}) = \nu(a_{\text{rec}})\nu_{\text{rec}}$. Hence, the CMB photons that are reaching us today have still a blackbody spectrum, the same they had at the recombination, but redshifted. Therefore, we expect to see this radiation in the microwave frequency range. Dicke and Peebles were preparing to look for this relic radiation when Penzias and Wilson heard about their work and realized that they had already found it. For this, Penzias and Wilson were awarded the Nobel Prize in 1978.

During the 1970s and 1980s several high-altitude balloon experiments carrying millimetre and submillimetre spectrometers were flown and many ground based experiments were performed; however, it was only the launch of the Cosmic Background Explorer (COBE) satellite in 1989 that allowed a measurement of the spectrum and isotropy of the CMB. This mission was dedicated to studies of the background radiation, not only in the millimetre and submillimetre wavebands, but also throughout the infrared waveband from 2 to 1000 μm. The final spectrum shown in Fig. 1.3 is that of a blackbody with a radiation temperature $T = 2.72548 \pm 0.00057$ K (Fixsen 2009).

Another fundamental observation of COBE is the isotropy of the distribution of the Cosmic Microwave Background over the sky. The prime instrument for this measurement was the Differential Microwave Radiometers which operated at frequencies of 31.5, 53 and 90 GHz. The result is that the CMB is extremely uniform over the whole sky. At a sensitivity level of about one part in 1000 of the total intensity, a large-scale anisotropy of dipolar form was observed over the whole sky. This global dipole anisotropy is attributed to effects associated with the Earth's motion through an isotropic radiation field. It was inferred that the Earth is moving at about 350 km s^{-1} with respect to the frame of reference in which the radiation would be perfectly isotropic.

After the removal of the dipole anisotropy, the analysis of the complete microwave data set obtained over the four years of the COBE mission revealed significant fluctuations at a level of only about 1 part in 100,000 of the total intensity.

1.3.1 Introducing fluctuations

When we observe the distribution of galaxies around us, we find that they are not arranged randomly, but they cluster together in coherent patterns. We see a large-scale structure that formed through the action of gravity on initially small amplitude perturbations in density.

A region of space that was initially overdense would give rise to a larger than usual gravitational potential and surrounding matter would fall into this potential, increasing

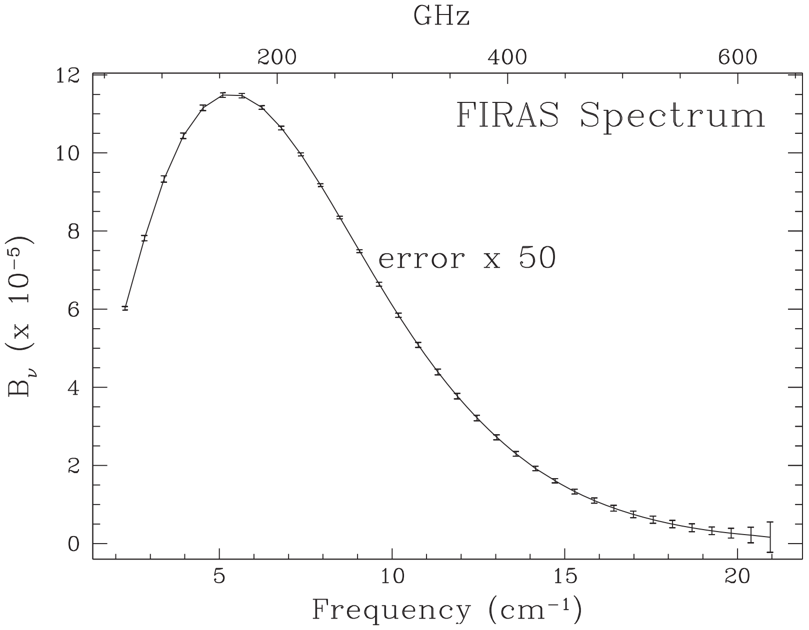

Figure 1.3: CMB spectrum as measured by COBE/FIRAS (Fixsen et al. 1996). It is well described by a blackbody spectrum with temperature $T = 2.275$ K. Brightness is measured in erg s^{-1} cm^{-2} sr^{-1} Hz^{-1}.

the overdensity. Therefore, the next step in developing a more realistic model of the Universe is to include small density perturbations into the homogeneous, isotropic models and study their development.

The best ways to learn about the evolution of structure and to compare theory with observations are to look at anisotropies in the CMB, which are a snapshot of the conditions when the Universe was 380000 years old, i.e. on the surface of last scattering. The anisotropies in the Cosmic Microwave Background are of particular interest because they contain information fundamental to reconstruct what the basic parameters of the Universe are and what must have happened in the very distant past.

The fundamental measurement in microwave background studies is its temperature seen in a given direction on the sky $T(\theta, \phi)$, so we write deviations from the mean value as

$$\frac{\Delta T(\theta,\phi)}{\bar{T}} = \frac{T(\theta,\phi) - \bar{T}}{\bar{T}}, \tag{1.23}$$

where $\theta \in [0, \pi]$ and $\phi \in [0, 2\pi)$. Density fluctuations are traced by CMB temperature differences across the sky ($\Delta T/\bar{T} \propto \Delta\rho_m/\bar{\rho}_m$). Since the CMB temperature is a two-dimensional field, it is useful to expand its anisotropies in spherical harmonics[1]

$$\frac{\Delta T}{\bar{T}}(\theta,\phi) = \sum_{\ell=2}^{\infty} \sum_{m=-\ell}^{m=\ell} a_{\ell m} Y_{\ell m}(\theta,\phi). \tag{1.24}$$

As there are no preferred directions cosmologically, theories predict only statistical information about the sky, not that the temperature in a certain direction should have a

---

[1] The largest anisotropy is a fluctuation of about 1 part in 1000 that forms a dipole pattern across the sky due to a Doppler shift in the CMB temperature owing to our relative motion. This dipole is clearly of local rather than primordial origin, and so we generally subtract it before dealing with the CMB anisotropy.

particular value. For this reason, we are interested only in the statistics of the observed temperature pattern. The most common and useful statistic is known as the 2-points correlation function of the temperature field $C(\beta)$, which is given by the average across all pairs of points in the sky (θ, ϕ) separated by an angle β

$$C(\beta) \equiv \langle \frac{\Delta T}{\bar{T}}(\theta_1, \phi_1) \frac{\Delta T}{\bar{T}}(\theta_2, \phi_2) \rangle. \tag{1.25}$$

Under the assumptions that our theory has no preferred direction in the sky (statistical isotropy) and that the fluctuations in temperature have Gaussian statistics, the correlation function encodes all of the physical information in the CMB anisotropies. Introducing the multipole expansion (Wilson & Silk 1981), we can write

$$C(\beta) = \frac{1}{4\pi} \sum_{\ell} (2\ell + 1) P_{\ell}(\cos\beta) C_{\ell}, \tag{1.26}$$

where $P_{\ell}(\cos\beta)$ are the Legendre polynomials and the C_{ℓ} are the quantities of interest known as the *power spectrum*, which are defined in terms of the $a_{\ell m}$ as

$$C_{\ell} \equiv < a_{\ell m} a^*_{\ell m} > = \frac{1}{2\ell + 1} \sum_{m} a_{\ell m} a^*_{\ell m}. \tag{1.27}$$

One can think of ℓ as the variable "Fourier" conjugate to the angle, hence $\ell \simeq \pi/\beta$. Anisotropy on a given angular scale is related to density perturbations on the last scattering surface of a given wavelength and the relevant wavelengths correspond to the length projected by that angle on the last-scattering surface: $\lambda \sim 200$ Mpc (θ/deg). This means that multipole moment ℓ receives its dominant contribution from Fourier mode k, where $\ell = kr$ and r is the comoving distance to last scattering.

Fig. 1.4 shows the anisotropy angular power spectrum as measured by the Planck satellite. We can distinguish three different parts: at low-ℓ (large angular scales) there is a flat plateau that rises into a series of bumps that then damp quasi-exponentially on small angular scales. These regions are separated by two angular scales: the first at about 1 degree and the second at a few arcminutes. The shape of the power spectrum is strictly related to the spectrum of primordial fluctuations, the dynamics of their evolution and the values of cosmological parameters.

To understand the origin of the features in the power spectrum let us go back in time to just before recombination. At this time the Universe contained the tightly coupled photon-baryon fluid and dark matter, with perturbations in the densities on a wide range of scales. While perturbations in the dark matter grow continuously as the Universe expands, the collapse of a perturbation in the baryon-photon fluid, which is driven by gravity, is opposed by the pressure of the photons. As an overdensity falls into a gravitational potential it becomes more compressed. Eventually, photon pressure halts the collapse and the mode rebounds, becoming increasingly rarefied. Then, the expansion is slowed and halted because gravity becomes again dominant over radiation pressure, causing the mode to recollapse once more. This process sets up an acoustic wave, where gravity is the driving force and pressure is the restoring force. Therefore, fluctuation dynamics is governed by a harmonic-oscillator-like equation.

At large angular scales ($\ell < 100$), whose projection in the sky today has an angular scale $\beta > 2°$, perturbations had periods longer than the age of the Universe at last scattering, i.e. larger than the horizon[2]. These perturbations increase according to a power

---

[2] Maximum distance that a sound wave could travel within a given time τ and undergo coherent oscillations. It sets an upper limit to the wavelengths that acoustic waves could have at the epoch of recombination.

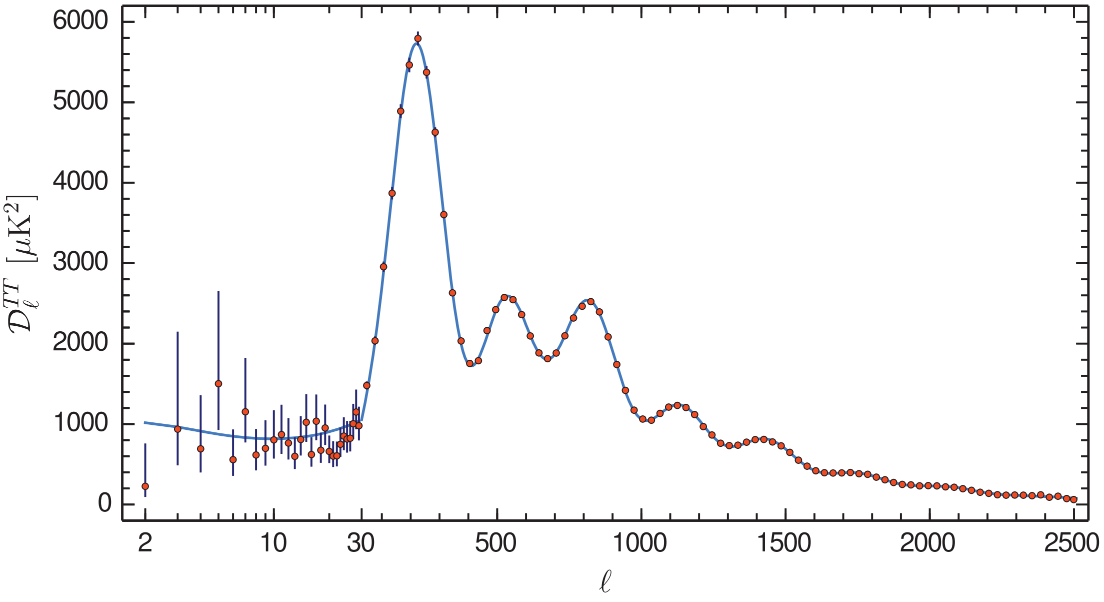

Figure 1.4: CMB temperature angular power spectrum as a function of the multipole moment as measured by the Planck satellite (Planck Collaboration et al. 2018a). Roughly, one degree on the sky today corresponds to $\ell \sim 100$, one arcminute to $\ell \sim 1000$. It is conventional to plot $\mathcal{D}_\ell = \ell(\ell+1)C_\ell$ rather than C_ℓ because this is approximately the power per logarithmic interval in ℓ. Also, in the model of scale-invariant fluctuations from the Sachs-Wolfe effect (see below) $\ell(\ell+1)C_\ell$ is constant.

law, as a result of the action of gravity without pressure. These waves are essentially frozen in their initial configuration and provide a probe of the physics that created them. Since CMB photons lose energy climbing out of the potential wells (*Sachs-Wolfe effect*), the temperature differences seen on the sky reflect the gravitational potential differences on the last-scattering surface. If the density fluctuations are approximately scale-invariant, the plateau in the angular power spectrum is flat.

At scales smaller than the horizon, fluctuations that produce anisotropy on sub-degree angular scales ($10^2 < \ell < 10^3$, corresponding to $0.1° < \beta < 2°$) undergo oscillation. At maximum compression (rarefaction) the CMB temperature is higher (lower) than average. Neutral compression corresponds to velocity maxima of the fluid, which leads to a Doppler shift. Since last-scattering is nearly instantaneous, the CMB provides a snapshot of these acoustic oscillations, with different wavelength modes being caught in different phases of oscillation. This leads to the presence of peaks and valleys in the angular power spectrum: peaks are modes that were maximally under or overdense at last-scattering and the troughs are velocity maxima, which are $\pi/2$ out of phase with the density maxima. After decupling the pressure effect disappears and fluctuations grow once again as a power law under the gravitational effect.

On shorter scales ($\ell > 10^3$, corresponding to $\beta > 2°$) the finite duration of recombination has an observable effect. We expect an exponential damping of the spectrum, know as *Silk damping* (Silk 1968), due to the fact that photons can only diffuse out of any overdensity on scales smaller than the mean free path times the square root of the number of scatterings. This washes out density fluctuations.

Anisotropies created before recombination are called primary anisotropies. However, several processes, generally known as secondary anisotropies, occurred after recombination and altered the anisotropy power spectrum. As the photons travel through the Universe from the surface of last scattering, they can interact gravitationally with the

Parameter	Value
$\Omega_b h^2$	0.02233 ± 0.00015
$\Omega_c h^2$	0.1198 ± 0.0012
$100\Theta_{MC}$	1.04089 ± 0.00031
τ	0.0540 ± 0.0074
$\ln(10^{10} A_s)$	3.043 ± 0.014
n_s	0.9652 ± 0.0042

Table 1.1: The six fundamental cosmological parameters determined by Planck (Planck Collaboration et al. 2018a). The h factor is related to the Hubble constant through $h = H_0/(100)$ km s^{-1} Mpc^{-1}.

matter (integrated Sachs-Wolfe effect and gravitational lensing). Due to reionization[3], there must be a finite optical depth τ for Thomson scattering between the epoch of recombination and the present epoch. Therefore, photons can scatter off free electrons and the effect of this scattering is to attenuate temperature fluctuations originating from the last scattering layer by a factor $e^{-\tau}$. Finally, once structures are well formed, photons can interact with hot gas in the intergalactic medium. The CMB photons can either be upscattered in energy when interacting with hot gas (“thermal” Sunyaev-Zel’dovich effect) or have their temperature altered by Doppler scattering from moving gas (the “kinetic” S-Z effect).

The Wilkinson Microwave Anisotropy Probe (NASA, 2001) (Bennett et al. 2003) was the first experiment to define in detail the power spectrum of temperature fluctuations in the CMB and its results enabled precise estimates of the cosmological parameters. The mission created a full-sky map of the CMB with a 13 arcminute resolution via multi-frequency observation (five frequency bands in the range 23–94 GHz). These results were further improved by the Planck satellite (ESA, 2009) (Planck Collaboration et al. 2018a), which had an improved angular resolution (up to 5 arcminute) and a wider frequency coverage (nine frequency bands in the range 30–857 GHz). The current standard model describing the evolution of the Universe is called Λ cold dark matter (ΛCDM) model since it is based on the presence of dark energy and cold dark matter. This model is based on six fundamental cosmological parameters, which can be constrained by fitting the shape of the power spectrum of the CMB anisotropies. The main parameters are the baryonic matter density Ω_b, the dark matter density Ω_c, the acoustic scale angle Θ_{MC}, the amplitude of scalar fluctuations A_s (Sect. 1.4), the scalar spectral index n_s (Sect. 1.4) and the reionization optical depth τ. Their values, as measured by Planck, are listed in Table 1.1. All the other parameters, such as the Hubble constant H_0 or the dark energy density Ω_Λ, can be inferred from these. The Planck full-sky map of CMB temperature anisotropies is shown in Fig. 1.5.

As we have seen, observations show that the large-scale geometry of the Universe is close to flat ($\Omega_0 \approx 1$) and that $\Omega_m \sim 0.28$ and $\Omega_\Lambda \sim 0.72$. These results are also consistent with many independent astronomical estimates of the cosmological parameters.

---

[3] At some epoch well after the epoch of recombination, the intergalactic gas must have been heated and reionised with the ignition of the first stars.

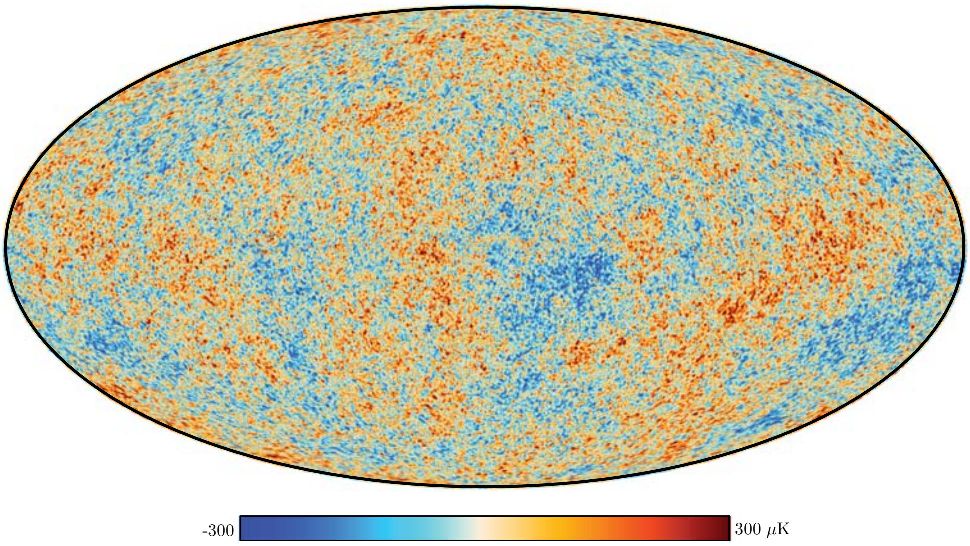

Figure 1.5: Planck full sky map of CMB temperature anisotropies at $5'$ resolution on which are based the analyses of the statistical character of the fluctuations (Planck Collaboration et al. 2018b).

1.4 Inflation

The standard Hot Big Bang model has an undoubted success as it provides a reliable and tested account of the history of the Universe from the synthesis of light elements until today. However, it raises also many questions that are not answered within the model. Hereafter we report the main problems:

The horizon problem. The problem is: why is the Universe so isotropic? We can compute how far light could have travelled along the last scattering surface since the Big Bang as

$$r_H(\tau) = \int_0^\tau \frac{c d\tau'}{a(\tau')} = \frac{c}{H_0} \int_0^a a^{\frac{(3w-1)}{2}} da, \tag{1.28}$$

where we used the Friedmann's equation (1.10), $k = 0$ and the general equation of state (1.12). In matter-dominated models, this distance is $r \sim 3ct$, corresponding to an angle $\theta_H \approx 2^\circ$ on the sky. Thus, regions of the sky separated by greater angular distances could not have been in causal communication, so there is apparently no reason why the CMB should be so isotropic.

The flatness problem. The problem arises from the fact that, if the Universe were set up with a value of the density parameter slightly different from the critical value $\Omega_{\text{tot},0} = 1$, it would diverge very rapidly. To get a value close to 1 today requires a fine tuning of Ω_{tot} in the past. From Eq. (1.17) we get

$$\Omega_{\text{tot}}(\tau) = \frac{k(\tau)c^2}{H^2(\tau)a^2(\tau)} + 1. \tag{1.29}$$

Using Eqs. (1.11) and (1.12), we find that the rate at which the value of Ω_{tot} changes with respect to the change of the scale factor is

$$\frac{d\Omega_{\text{tot}}}{d\ln a} = \Omega_{\text{tot}}(\Omega_{\text{tot}} - 1)(1 + 3w). \tag{1.30}$$

From Eq. (1.30) we see that, if $w > -1/3$ like for matter and radiation, then the condition $\Omega_{\text{tot}} = 1$ is unstable. Thus, since $\Omega_0 \sim 1$ at the present epoch, it must have been extremely close to the critical value in the remote past. However, there is nothing in the standard model that would lead us to prefer any particular value of Ω. This is sometimes referred to as the *fine-tuning problem*.

The primordial fluctuations problem. This problem refers to the origin of the density fluctuations from which galaxies and large-scale structures formed. There must have been some physical mechanism that generated finite amplitude perturbations, $\delta\rho/\rho \sim 10^{-5}$, with power spectrum $P(k) \propto k$ in the early Universe, but this is left unexplained by the Big Bang model.

As if these problems were not serious enough, we have to deal with the fact that the nature of dark matter and dark energy is unknown. Thus, one of the consequences of precision cosmology is the remarkable result that we do not understand the nature of about 95% of the energy which drives the large-scale dynamics of the Universe.

An important development in cosmological studies came in 1981, when Alan Guth proposed the inflationary model for the very early Universe (Guth 1981). He showed that, if the Universe went through an early exponential expansion phase, this would solve both the problem of the isotropy on a large scale and would drive the Universe towards a flat spatial geometry, however curved it might have been in its initial stages.

Let us consider a tiny region of the early Universe expanding under the influence of the exponential expansion. Particles within the region were initially very close together and in causal communication with each other. Before the inflationary expansion began, the region had physical scale less than the particle horizon, and so there was time for it to reach a uniform and homogeneous state. The region then expanded exponentially so that neighbouring points were driven to such large distances that they could no longer communicate by light signals. At the end of the inflationary epoch, the Universe transformed into the standard radiation-dominated Universe.

The timescale 10^{-34} s is taken to be the characteristic e-folding time for the exponential expansion. Over the interval from 10^{-36} s to 10^{-34} s, the radius of curvature of the Universe increased exponentially by a factor of about e^{60}.

The exponential expansion also had the effect of straightening out the geometry of the early Universe. From Eq. (1.11) follows that the condition $\ddot{a} > 0$ is equivalent to $w < -1/3$, which means $P < 0$. Moreover, Eq. (1.30) implies that, if $\Omega_{\text{tot, in}} > 1$, than $d\Omega_{\text{tot}}/d\ln a < 0$, and viceversa. Thus, the final state always has $\Omega_{\text{tot}} = 1$.

Inflation is also a mechanism for generating primordial perturbations over the homogeneous Universe: it predicts that quantum-mechanical perturbations, responsible for the variations around smoothness, in the very early Universe were first produced when the relevant scales were causally connected. It also makes quantitative predictions about the intensity and spectrum of primordial gravitational waves which are accessible through experimental validation.

The underlying concepts of inflation have been used to define the necessary properties of the inflaton potential needed to create the Universe as we know it. An accelerated expansion can be achieved with a scalar field $\phi(\tau)$, which is assumed to be homogeneous at a given epoch. Associated with this field there are a kinetic energy $\dot{\phi}^2/2$ and a potential energy $V(\phi)$, which allow us to write the expressions for the density and pressure of the scalar field

$$\rho c^2 = \frac{1}{2}\dot{\phi}^2 + V(\phi), \tag{1.31}$$

$$P = \frac{1}{2}\dot{\phi}^2 - V(\phi). \tag{1.32}$$

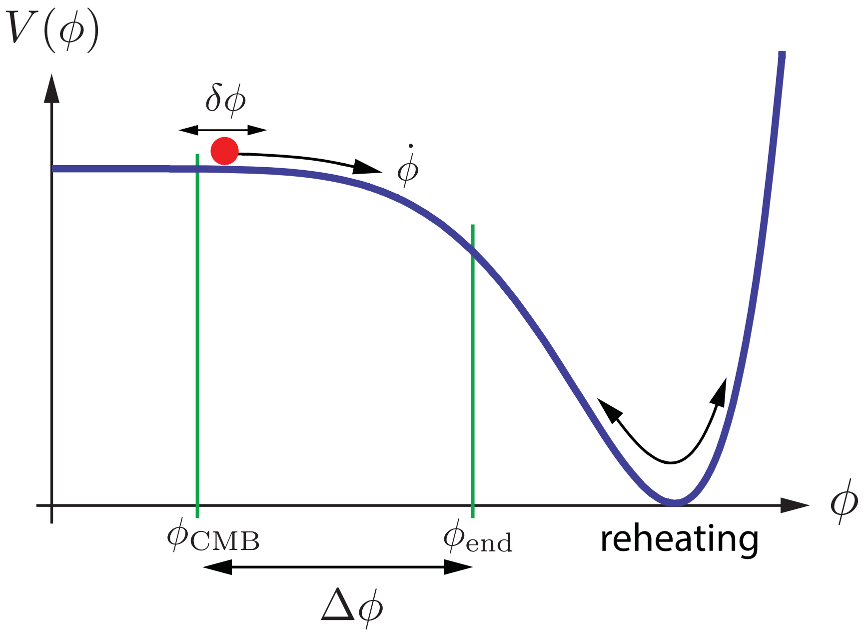

Figure 1.6: Example of an inflaton potential. Acceleration occurs when the potential energy of the field, $V(\phi)$, dominates over its kinetic energy, $\frac{1}{2}\dot{\phi}^2$. Inflation ends at ϕ_{end} when the kinetic energy becomes comparable to the potential energy, $\frac{1}{2}\dot{\phi}^2 \approx V$. CMB fluctuations are created by quantum fluctuations $\delta\phi$ about 60 e-folds before the end of inflation. At reheating, the energy density of the inflaton is converted into radiation.

The scalar field can provide an equation of state with a negative pressure provided that the potential energy of the field is very much greater than its kinetic energy. Combining Eqs. (1.31) and (1.32) with Einstein equation, we find the time evolution of the scalar field

$$\ddot{\phi} + 3H\dot{\phi} + V'(\phi) = 0. \tag{1.33}$$

Thus, to obtain the inflationary expansion over many e-folding times, the kinetic energy term must be very small compared with the potential energy, $V(\phi) \gg \frac{1}{2}\dot{\phi}^2$, and the potential energy term must be very slowly varying with time (overdamped motion), $|\ddot{\phi}| \ll |3H\dot{\phi}|$. These relations are known as *slow-roll* conditions. Under these conditions, we obtain the exponential expansion we need for inflation, i.e. $a(\tau) \propto e^{H\tau}$.

At the end of the inflationary expansion, when slow-roll conditions are no longer satisfied, the scalar field decays into the types of particles which dominate our Universe at the present epoch, releasing a vast amount of energy which reheats the contents of the Universe to a very high temperature.

Eventually, quantum fluctuations in the scalar field ϕ can result in primordial density perturbations: if ϕ can vary in time, then it can also vary in space. Since the energy density is determined by ϕ, fluctuations in ϕ will induce fluctuations in the energy density which will then induce fluctuations in the space-time metric. We can write the expression for the evolution of fluctuations in the inflationary expansion decomposing the inflaton field into a uniform homogeneous background and a perturbed component

$$\phi(\mathbf{x}, \tau) = \phi^{(0)}(\tau) + \delta\phi(\mathbf{x}, \tau). \tag{1.34}$$

The homogeneous term drives the background expansion while the perturbed term generates fluctuations. The quantum fluctuations perturb both the matter distribution and the space-time metric.

The spatially flat, homogeneous and isotropic background space-time possesses symmetries, which allow a decomposition of the metric and the stress-energy tensor perturbations into independent scalar, vector and tensor components. The importance of this decomposition is that the perturbations of each type evolve independently and can therefore be treated separately (Baumann 2009). Vector perturbations decay with the expansion of the Universe, while the primordial power spectra of scalar and tensor fluctuations are

$$P_s(k) = A_s k^{n_s - 4}, \tag{1.35}$$

$$P_t(k) = A_t k^{n_t - 3}, \tag{1.36}$$

where we theoretically expect $n_s \simeq 1$ and $n_t \simeq 0$. Tensor fluctuations are often normalized relative to the amplitude of scalar fluctuations, that is why we can define the *tensor-to-scalar ratio*

$$r \equiv \frac{A_t}{A_s}. \tag{1.37}$$

Scalar perturbations to the metric couple to the density of matter and radiation and ultimately are responsible for most of the inhomogeneities and anisotropies in the Universe. In addition, inflation also predicts the existence of a stochastic background of tensor fluctuations, the so-called gravitational waves, that induce a specific pattern in the polarization of the CMB. These fluctuations, if measured, would be a unique signature of inflation and would offer the best window on the physics driving inflation.

The simplest and canonical model for inflation, the single-field slow-roll inflation, makes a number of predictions that have been confirmed by a sequence of increasingly precise experiments over the past decades. These include the prediction that primordial perturbations are adiabatic, the spectrum of primordial perturbations should be nearly scale invariant, the distribution of primordial perturbations should be nearly Gaussian, and there should be primordial perturbations at the time of CMB decoupling.

The simplest predictions of inflationary theory is that the spectrum of gravitational waves should be scale invariant with spectral index similar to that of the scalar perturbations $n \approx 1$. This is expected to be observed at multipoles less than about 100, or angular scales greater than $\beta \approx 2^\circ$, corresponding to the horizon scale at the epoch of recombination. For higher multipoles, the primordial gravitational waves decay adiabatically.

It is difficult to distinguish the contributions of scalar and tensor perturbations at multipoles $\ell \leq 100$ on the basis of their power spectra alone. Their polarisation signatures are, however, quite different (see Sect. 1.5.2).

1.5 Polarization of the CMB

The measurement of the power spectrum of temperature fluctuations in the cosmic microwave background radiation is a great achievement. However, the study of the CMB polarization, both theoretically and experimentally, has the potential to produce unique information about the primordial fluctuations and, hence, about inflation.

1.5.1 The polarization mechanism

The mechanism for creating polarisation of the cosmic microwave background radiation is Thomson scattering of the radiation by free electrons. A beam of unpolarised radiation incident upon a free electron causes an oscillation of the electron in the plane perpendicular to the direction of the beam. The Thomson scattering cross section can be written as

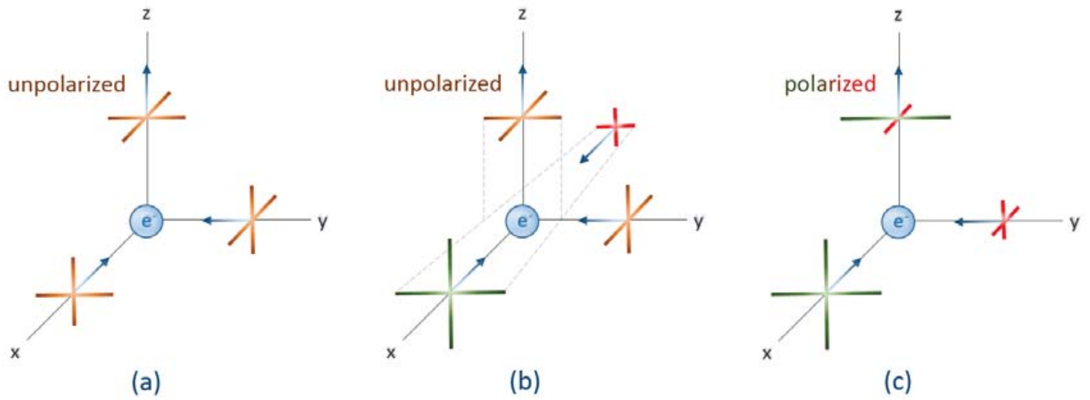

Figure 1.7: (a) For an isotropic incident radiation, the scattered radiation is not polarized; (b) a dipolar pattern gives an averaged contribution to the scattered radiation in the y direction; (c) a quadrupolar distribution produces a net polarization in the scattered radiation.

$$\frac{d\sigma_T}{d\Omega} = \frac{1}{2} r_e^2 (1 + \cos^2\theta) \propto |\hat{\varepsilon}' \cdot \hat{\varepsilon}|^2, \tag{1.38}$$

where θ is the angle between the incident and scattered direction, r_e is the classical electron radius and $\hat{\varepsilon}$ and $\hat{\varepsilon}'$ are the incident and scattered polarization directions. The cross section is frequency independent, so the scattering is equally effective at all frequencies, under the hypothesis of $h\nu \ll m_e c^2$. The degree of polarization of the scattered wave then is

$$\Pi = \frac{1 - \cos^2\theta}{1 + \cos^2\theta}. \tag{1.39}$$

Since $\Pi > 0$, the scattering of a completely unpolarized incident radiation produces a scattered radiation with some degree of polarization, the degree depending on the viewing angle with respect to the incident direction. The accelerated electron radiates with a dipole pattern so that the scattered radiation is 100% polarised when the electron is viewed perpendicular to the direction of propagation of the beam.

In the case of the CMB, however, the distribution of the radiation is highly isotropic and, in the case of complete isotropy, there would be exact cancellation of the polarised signals. Even in the case of a dipole distribution of the radiated field, there is no net polarisation because of the dipole symmetry of the Thomson scattering process. The only way of creating a net polarised signal is if the radiation field incident upon the electron has a quadrupole anisotropic distribution of intensity. Therefore, the detection of polarised signal in the Cosmic Microwave Background radiation is the evidence for a quadrupole component in its intensity.

Before the decoupling, during the tight coupling epoch, photons had a distribution which mirrored that of the electrons. An immediate consequence is that the angular dependence of the radiation field at a given point can only possess a monopole (corresponding to the temperature) and a dipole (corresponding to a Doppler shift from a peculiar velocity) component, and that the radiation field is unpolarized. Any higher multipole moment will rapidly damp away as the electrons scatter off the free electrons, and no net polarization can be produced through scattering. A quadrupole is produced only at decoupling as free streaming of the photons begins.

We are interested in the polarisation arising from scattering in the last scattering layer. Hence, let us consider the behavior of the free streaming at times near decoupling. At later times, the number density of free electrons which can Thomson scatter has dropped to negligible levels and no further polarization can be produced. On length scales large compared to the thickness of the surface of last scattering, the quadrupole moment and thus the polarization couples much more strongly to the velocity of the baryon-photon fluid than to the density and the maximum of the polarised signal occurs at wavelengths which are of the same order as the mean free path of the photons in the last scattering layer.

It is crucial that these process takes place in the last scattering layer; otherwise, if there were many scatterings, the polarisation would be washed out. It is the fact that the photons stream freely from the last scattering layer that results in the finite quadrupole anisotropy in the photon distribution.

1.5.2 Description of polarization

The Cosmic Microwave Background is characterized completely by its temperature and polarization in each direction on the sky. However, the mathematical characterization of CMB polarization anisotropies is slightly different from the description of temperature fluctuations we made in Sect. 1.3.1, because polarization is not a scalar field, so the expansion in terms of spherical harmonics is not applicable.

The polarization state of the radiation is described in terms of Stokes parameters (Jackson 1975). For a monochromatic wave propagating in the z-direction, the components of the wave's electric field vector at a given point in space can be written as

$$E_x = a_x(t)\cos[\omega t - \theta_x(t)], \qquad E_y = a_y(t)\cos[\omega t - \theta_y(t)]. \tag{1.40}$$

If these two components are correlated, then the wave is said to be polarized. The Stokes parameters are defined as the time averages

$$I \equiv \langle a_x^2 \rangle + \langle a_y^2 \rangle, \tag{1.41}$$

$$Q \equiv \langle a_x^2 \rangle - \langle a_y^2 \rangle, \tag{1.42}$$

$$U \equiv \langle 2 a_x a_y \cos(\theta_x - \theta_y) \rangle, \tag{1.43}$$

$$V \equiv \langle 2 a_x a_y \sin(\theta_x - \theta_y) \rangle. \tag{1.44}$$

The parameter I gives the radiation intensity which is positive definite. The other three parameters can take either sign and describe the polarization state: the polarization magnitude and angle are $P = \sqrt{Q^2 + U^2}$ and $\alpha = \frac{1}{2}\tan^{-1}(U/Q)$. The parameter V describes circular polarization, but in cosmology it is usually ignored because it cannot be generated through Thomson scattering. Q and U describe orthogonal modes of linear polarization and depend on the axes in relation to which the linear polarization is defined. When the coordinate system is rotated by an angle ψ, the same radiation field is described by the parameters

$$Q' = Q\cos(2\psi) + U\sin(2\psi),$$
$$U' = -Q\sin(2\psi) + U\cos(2\psi),$$

while the temperature is invariant under the same rotation. This means that Q and U transform as a spin-2 field under rotation by an angle ψ; i.e. if we represent the polarization by a complex number $P = Q + iU$, then $P \to Pe^{2i\alpha}$ under a rotation of the coordinate axes by an angle α. Therefore, once the polarization Q and U has been measured for each direction in the sky (θ, ϕ), we can construct the polarization tensor field.

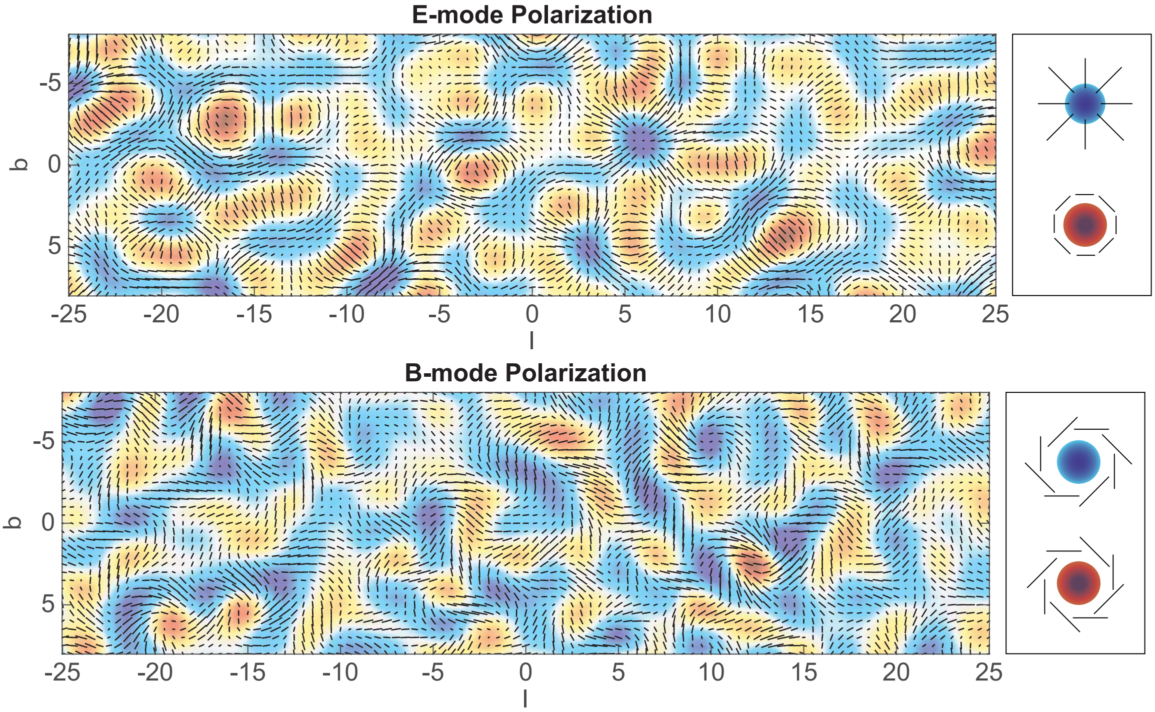

Figure 1.8: The top panel shows a polarization pattern composed only of E modes and the bottom panel one composed only of B modes (Kamionkowski & Kovetz 2016). As reported on the right, around hot spots (red) the polarization pattern of the E mode is tangential and radial around cold spots (blue). The polarization pattern surrounding hot and cold spots of the B mode show a characteristic swirling pattern (with different orientation around hot and cold spots).

Anything we say about Stokes parameters Q and U is tied to the coordinate system we choose. It is, therefore, useful to find a coordinate-system independent representation of this tensor field.

Any 2×2 tensor field on the sphere can be written as the gradient of some scalar field $E(\theta, \phi)$ plus the curl of some other scalar field $B(\theta, \phi)$ (Kamionkowski et al. 1997). Since any scalar field on the sphere can be expanded in spherical harmonics, it follows that the polarization tensor can be expanded in terms of basis functions that are gradients and curls of spherical harmonics. Therefore, we can define gradient ("E modes") and curl ("B modes") components of the tensor field that are independent of the orientation of the coordinate system and that completely specify the linear polarization field

$$E(\theta, \phi) = \sum_{l,m} a_{E,lm} Y_{lm}(\theta, \phi), \tag{1.45}$$

$$B(\theta, \phi) = \sum_{l,m} a_{B,lm} Y_{lm}(\theta, \phi). \tag{1.46}$$

Although E and B are both invariant under rotations, they are oriented at 45° with respect to one another and they behave differently under parity transformations. Note that when reflected about a line going through the center, the E-mode patterns remain unchanged, while the B-mode patterns change sign. Fig. 1.8 gives an example of E- and B-mode pattern.

The cosmological significance of the E/B decomposition of CMB polarization is reported in Zaldarriaga & Seljak (1997), and we sum up the remarkable facts:

1. scalar (density) perturbations create only E-modes and no B-modes;
2. vector (vorticity) perturbations create mainly B-modes; however, vectors decay with the expansion of the Universe;
3. tensor (gravitational wave) perturbations create both E-modes and B-modes.

The fact that scalars do not produce B-modes while tensors do is the basis for the statement that the detection of B-modes would be a smoking gun of tensor modes, and therefore of inflation.

The symmetries of temperature and polarization (E- and B-mode) anisotropies allow four types of correlations: the autocorrelations of temperature fluctuations and of E- and B-modes denoted by TT, EE, and BB, respectively, as well as the cross-correlation between temperature fluctuations and E-modes: TE. All other correlations (TB and EB) vanish for symmetry reasons. The angular power spectra are defined as before

$$C_\ell^{XY} \equiv \frac{1}{2\ell+1}\sum_m a^*_{X,\ell m} a_{Y,\ell m}, \qquad X, Y = T, E, B \tag{1.47}$$

where the power spectrum C_ℓ^{TT} coincides with the power spectrum in Eq. (1.27) for the CMB temperature anisotropies.

The polarisation signal is expected to be much weaker than the intensity fluctuations and it is a considerable challenge to measure this signal experimentally, but this was first achieved by the ground-based Degree Angular Scale Interferometer (DASI) in 2002 (Kovac et al. 2002). Subsequent ground-based experiments including the CBI and Boomerang projects reported detection of the polarised background signal. From space, both WMAP and Planck experiments detected a positive polarisation signal.

The total intensity fluctuations, which were shown in Fig. 1.4, are displayed as filled dots at the top of Fig. 1.9 and are labelled TT. The polarisation power spectrum is labelled EE. The points and curve labelled TE are the cross-correlation power spectrum between the total intensity and the polarised intensity. The polarised component of the radiation is $\pi/2$ out of phase with the temperature perturbations and so the cross-correlation power spectrum has twice as many minima as the either the TT or the EE spectra. The blue line labelled BB shows the expected power spectrum of B-mode gravitational waves if the primordial ratio of tensor to scalar perturbations was $r = 0.3$. The "recombination peak" at $\ell \sim 100$ arises from gravitational waves that enter the horizon around the time of CMB decoupling. The "reionization bump" at $\ell \leq 10$ arises from re-scattering of the CMB by free electrons that were reionized by radiation from the first stars. The wiggles at higher ℓ arise from the difference in phases of gravitational waves at different wavelengths at the time of CMB decoupling. The overall amplitude scales with the tensor-to-scalar ratio r.

The extraction of the polarisation signal is particularly challenging because it has to be detected in the presence of the polarised Galactic radio emission, which has to be removed from the sky maps to reveal the polarisation associated with the primordial perturbations (see Sect. 1.6.1).

1.6 Future perspectives in observations

Since the discovery of the CMB, several ground-based and balloon-borne experiments, as well as three space missions, have studied its properties. Currently, only the gravitational lensing B-mode signal has been detected and measured, while B-modes at degree

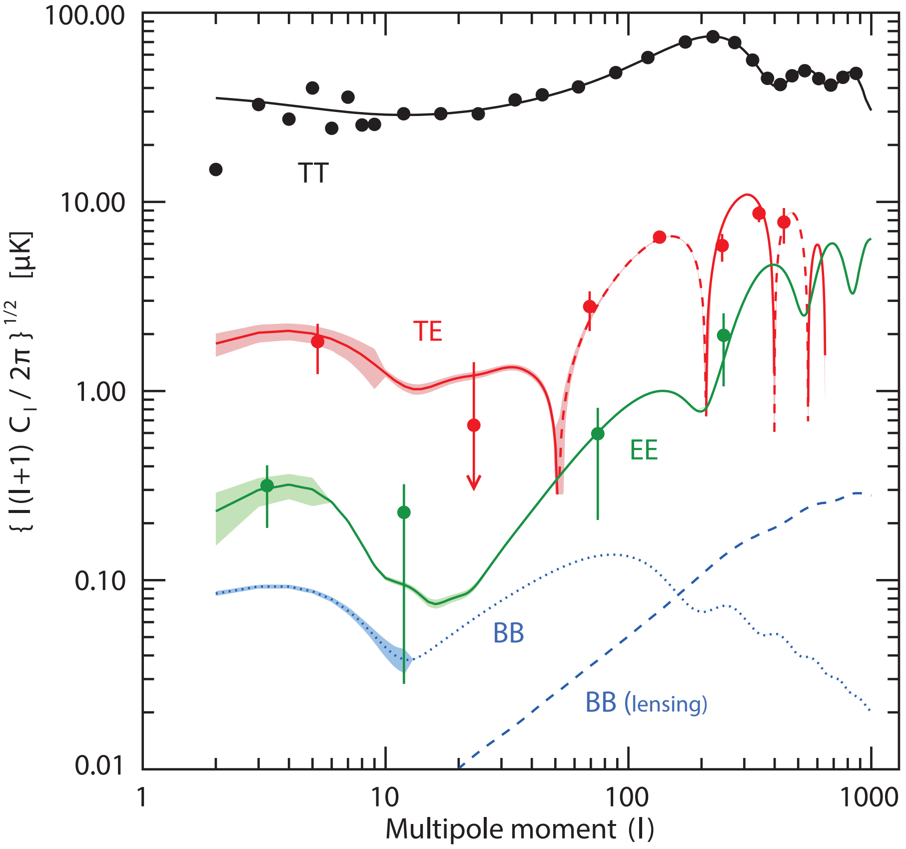

Figure 1.9: Power spectrum of fluctuations in the intensity and polarisation of the Cosmic Microwave Background radiation. Plots for the total intensity, the polarised intensity and the cross-correlation between the total intensity and the polarised intensity are labelled TT, EE and TE respectively. The dashed sections of the TE curve indicates multipoles in which the polarisation signal is anticorrelated with the total intensity. The blue line labelled BB shows the expected power spectrum of B-mode gravitational waves if the primordial ratio of tensor to scalar perturbations was $r = 0.3$. The B-mode signal due to gravitational lensing of the E-modes is shown as a dashed blue line. The upturn in the polarised signal at $\ell \leq 10$ is associated with polarisation originating during the reionisation era.

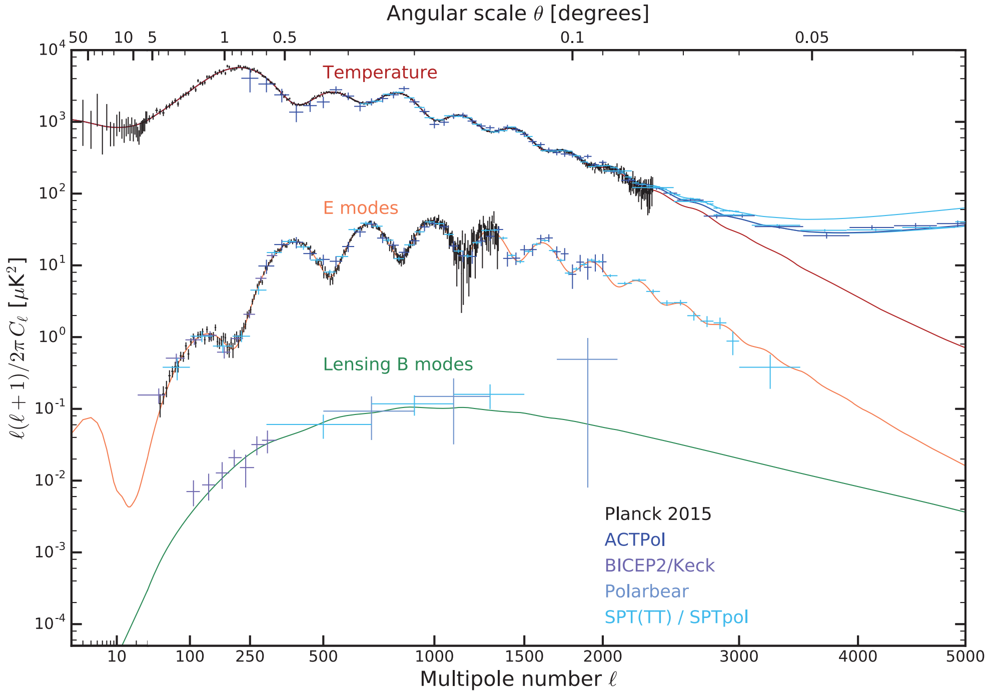

Figure 1.10: Current measurements of the angular power spectrum of the CMB temperature and polarization anisotropy.

angular scales, whose detection would be a direct evidence for primordial gravitational waves from the inflationary epoch, are still out of reach. Results from BICEP2 Collaboration et al. (2018) set an upper limit for the value of the tensor-to-scalar ratio $r < 0.07$ (68% CL).

The largest B-mode signal allowed by current observational limits is of the order of 10 nK, and a sensitivity to a tensor-to-scalar ratio as small as $r \sim 10^{-3}$ implies a B-mode signal four orders of magnitude smaller. Therefore, detecting a primordial CMB signal of this amplitude is a very hard task.

In the last decade, several ground based experiments have been proposed and deployed, mostly in Antarctica, as BICEP/Keck Array (Ade et al. 2016) and SPT (Carlstrom et al. 2011), and in the Atacama Desert in Chile, like Polarbear (Polarbear Collaboration et al. 2014), CLASS (Dahal et al. 2020), QUIET (Bischoff et al. 2013), and ACT (Thornton et al. 2016). Moreover, several balloon experiments as EBEX (Reichborn-Kjennerud et al. 2010) and SPIDER (Gualtieri et al. 2018) in the last years. All these experiments have increased their sensitivities following a scaling law, which depends on the total number of bolometers. To maintain this scaling, more focal plane pixels and more telescopes are required. Fig. 1.10 shows the current state of the temperature and polarization anisotropy measurements.

Nowadays, several experiments are being designed in order to detect the B-mode signal. In particular, the Simons Observatory (Ade et al. 2019), QUBIC (Tartari et al. 2016) and the LSPE (see Sect. 2). Furthermore, a new satellite mission, named LiteBIRD (Suzuki et al. 2018), has been recently approved by the japanese space agency JAXA.

Unfortunately, between us and the last-scattering surface at $z \sim 1100$, there is a long line of foregrounds which interfere with our ability to make accurate measurements. Measurements from the ground are hidden by atmospheric noise, which contribute at all frequencies. In nearby outer space, the emission from the interplanetary dust cloud generates pollution on frequencies > 100 GHz. Further out, there are various sources

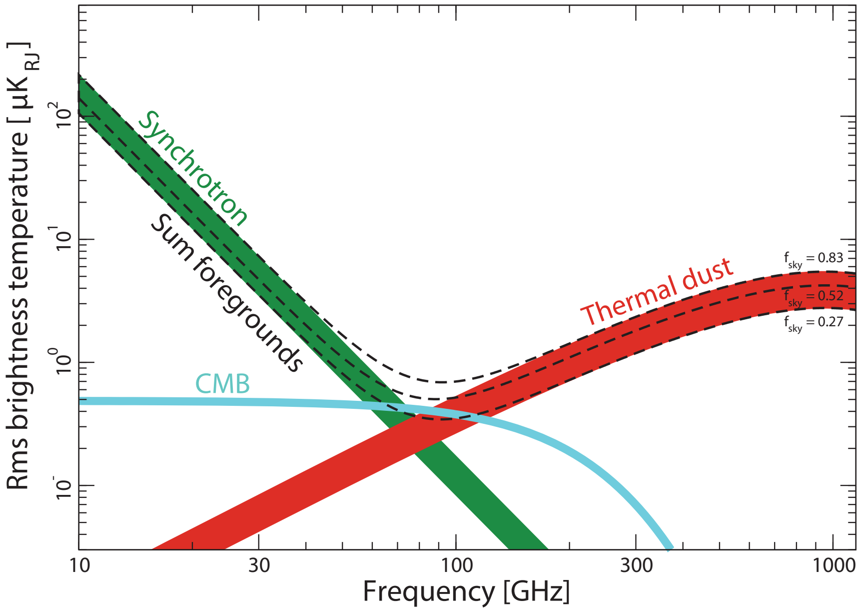

Figure 1.11: Frequency dependence of the main components of the sub-millimetre sky in polarization. The rms is calculated on maps at angular resolution of 40 arcmin on sky fraction between 73% and 93%, corresponding to the lower and upper edges of each line (Planck Collaboration et al. 2018b).

of contamination from localized objects, including inverse-Compton scattering of CMB photons from hot electrons in intracluster gas, synchrotron emission from active galactic nuclei, as well as extra-galactic dust emission.

Controlling systematic effects and astrophysical foregrounds represents one of the greatest challenge in the measurements of the CMB B-modes.

1.6.1 Galactic foregrounds

For large angular scale polarization measurements, the dominant foregrounds are of Galactic origin, mainly in the form of diffuse synchrotron and thermal dust emissions (free-free emission from accelerated electrons in the ionized gas), both of which involve the Galactic magnetic field. An overview of the frequency dependence of the major components (free-free emission, synchrotron, and dust) is given in Fig. 1.11.

Synchrotron. Synchrotron emission results from the acceleration of cosmic ray electrons in the Galactic magnetic field. If we consider a power law spectrum $\propto E^{-p}$ for the energy distributions of electrons propagating in a uniform magnetic field, the resulting emission is partially polarized with linear polarization fraction

$$f_s = \frac{p+1}{p+7/3},$$

and aligned perpendicularly to the magnetic field (Rybicki & Lightman 1979). The frequency spectrum of the synchrotron emission can be described by a power law $T(\nu) \propto \nu^{\beta_s}$ (where T is the brightness temperature) with spectral index

$$\beta_s = -\frac{p+3}{2}.$$

Galactic synchrotron emission is dominant at frequencies below 100 GHz, and both WMAP and Planck have observed its polarization signature at frequencies from 30 to 90 GHz. These multi-frequency measurements have been used to fit a spectral brightness temperature index $\beta_s \sim -3$ above 20 GHz (Planck Collaboration et al. 2016). Many of the upcoming CMB polarization experiments intend to take data at frequencies below 90 GHz, because improving the understanding of this foreground is essential.

Dust. Above 100 GHz, thermal emission from asymmetric dust grains in the interstellar medium, which align themselves with the Galactic magnetic field, induces a strong polarization signal, which depends on the composition, shape and size of the grains. The frequency spectrum of thermal dust is well described by a modified blackbody with functional form $I_d(\nu) \propto \nu^{\beta_d} B_\nu(T_d)$. The Planck High Frequency Instrument (HFI) has recently provided full-sky temperature and polarization maps at frequencies ranging from 100 to 857 GHz. While no region of sky was found to be clean enough to enable gravitational waves detection without foreground subtraction, Planck identified several patches of sky with considerably lower foreground amplitudes, which can be possible targets for future B-mode searches.

Both synchrotron and thermal dust emissions are partially linearly polarized with a variable polarization level from point to point in the sky. This makes the foreground emission a source of contamination even far from the Galactic plane and, for this reason, the separation between cosmological and Galactic signals represents a great challenge. With a multi-frequency coverage of the sky, the polarized foregrounds can be removed. Therefore, for forthcoming experiments, a wide selection of instrumental frequency bands is essential to a successful separation between cosmological and Galactic components.

1.6.2 Control of systematic effects

Rigorous control of systematic effects is an essential requirement for any experiment aiming at measuring the CMB polarization. Systematic effects include, for example, spurious signals due to temperature drifts, as well as inaccurate beam shapes, unknown cross-polarization leakage, and sidelobes in the optical response. Minimizing such systematic effects requires both a very careful instrument design and the capability to measure instrumental imperfections.

Extensive simulation of the impact of systematic effects on measurements is also an invaluable tool that accompanies every step of the experiment, from the initial concept of the instrument to the final design and realization phases. Simulations are also key tools to properly take into account for systematic effects on acquired data.

As a concrete example, an analysis of the LSPE-Strip optics is performed in this thesis, in order to evaluate its response and its effect on observations.

CHAPTER 2

The LSPE-Strip instrument

The *Large Scale Polarization Explorer* (LSPE) is an experiment dedicated to the observation of the CMB polarization on large angular scales and funded by "Agenzia Spaziale Italiana" (ASI) and "Istituto Nazionale di Fisica Nucleare" (INFN). The aim of this experiment is to constrain the B-modes produced by tensor perturbations, limiting the ratio of tensor-to-scalar perturbation amplitudes down to $r = 0.03$ at 99.7% confidence level, and improving the current upper limit on the ratio $r = 0.01$ (68% CL).

A second target is to produce maps of polarized emissions generated by synchrotron and interstellar dust in our Galaxy, enabling us to map the Galactic magnetic fields and study the properties of the ionized gas. LSPE will also play an important role as a pathfinder for future space CMB polarization missions like LiteBIRD.

LSPE will observe a fraction of the northern sky with two independent instruments: SWIPE (Short-Wavelength Instrument for the Polarization Explorer) and Strip[1]. The two instruments will survey the same sky region in five frequency bands between 43 and 240 GHz. The wide frequency coverage is essential to achieve the required sensitivity at the low-ℓ side of the power spectrum, and to monitor the foregrounds and subtract them from the cosmological signal. The combined scanning strategies of the two instruments will produce a full-frequency coverage over 25% of the sky.

Strip is a ground-based instrument based on an array of coherent polarimeters with cryogenic HEMT amplifiers working at 43 and 90 GHz (Franceschet et al. 2018), which will observe the sky from the Teide Observatory in Tenerife. The SWIPE instrument (de Bernardis et al. 2012) will survey the sky at 140, 220 and 240 GHz from a spinning stratospheric balloon, launched from Svalbard Islands, using large throughput multimode bolometers and a rotating Half Wave Plate (HWP). The 43 GHz channel of Strip will be used to measure the polarized synchrotron emission, while the 90 GHz channel will be exploited for atmospheric measurements. The 220 and 240 GHz channels of SWIPE will be used to check the level of the dust polarized emission, while the 140 GHz channel will be the one used for CMB measurements. In the following sections, I will describe the Strip instrument, which represents the background in which I developed my thesis.

2.1 Strip instrument description

The Strip instrument is a ground-based telescope that will operate from "Observatorio del Teide" in Tenerife, starting from mid 2022. Its main goal is the characterization of the Galactic synchrotron emission in the Q-band.

---

[1] Formerly it stood for STRatospheric Italian Polarimeter as it was supposed to fly together with SWIPE. After a change in the instrument configuration it is no longer an acronym.

Feature	Q-band	W-band
Feed diameter	50 mm	22.16 mm
Total feed length	136 mm	101.8 mm
Circular waveguide diameter	6.8 mm	2.62 mm
Matching over bandwidth	< -30 dB	< -30 dB
Cross-polarization over bandwidth	< -30 dB	< -30 dB
Frequency range	39 - 48 GHz	85 - 104 GHz

Table 2.1: Q-band and W-band feedhorn design requirements.

Strip consists of an array of forty-nine coherent polarimeters operating in a 18% frequency band centred at 43 GHz (Q-band) and six polarimeters operating in a frequency band centred at 95 GHz (W-band). The Q-band channel is the one devoted to astrophysical measurements, while the 95 GHz channel will be used to monitor and study the atmospheric emission at the Izana site, both in intensity and polarization. Besides, its data will be used for cross-checking purposes as well as to assess the feasibility of future W-band CMB experiments from Tenerife.

Each channel consists of a corrugated feedhorn, a polarizer, an orthomode transducer (OMT) and a polarimeter module. The whole array of receivers is actively cooled down to 20 K by a two-stage Gifford-McMahon cooling system, facing to a dual-reflector telescope through a dielectric window. The cryostat main window must have a very high transmittance to microwave radiation to reduce unwanted reflections inside the optical system and spurious polarization effects. The polarimeters design allows to directly measure the Stokes Q and U parameters through a double-modulation scheme. This design guarantees an excellent rejection of $1/f$ noise from amplifier gain fluctuations.

The feedhorn design is based on dual-profiled corrugated feedhorns which are the most performing antennas for CMB polarization measurements, given their high cross-polarization discrimination, beam symmetry and impedance matching over wide frequency bands. Table 2.1 summarizes some mechanical specifications, such as aperture diameter and total length of the feedhorn, and performance requirements, such as cross-polarization level and impedance matching. The final design is a $\sin^2 - \exp$ dual-profiled corrugated horn, which is the best compromise between specifications and compactness.

The forty-nine Q-band feedhorns of the array have the same profile and they are arranged in a honeycomb lattice of seven hexagonal modules, each including seven feedhorns. The W-band single feedhorns are placed around the Q-band modules in the focal plane of the telescope, as shown in the left panel of Fig. 2.1. In the right panel, we can see a cutaway of one of the Q-band modules and a detailed view of one of the W-band feedhorns.

The modules have been realized with the platelet technique, i.e. by overlapping thin metallic plates suitably machined to reproduce the feedhorn corrugated profile. Metallic plates have been verified with a metrological measuring machine, resulting to be compliant with the required mechanical tolerances (within 0.03 mm). The realization and testing of the modules have been performed at the Physics Department of the Università degli Studi di Milano (Del Torto et al. 2015).

Each feedhorn is connected to a polarizer system that converts the two orthogonal components of the electric field into right- and left-circular polarization components,

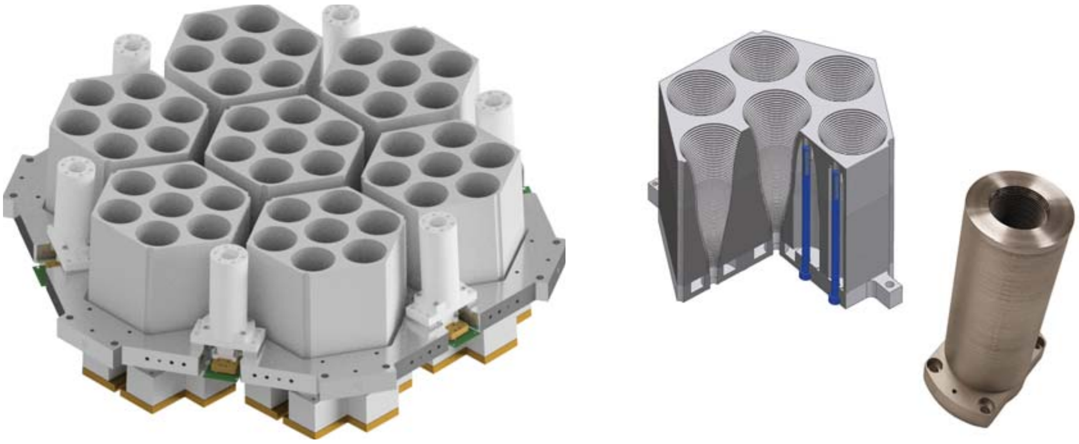

Figure 2.1: *Left*: Sketch of the focal plane with the 49 feedhorns at 43 GHz, the 6 feedhorns at 95 GHz and the other components of the detection chain. *Right*: Highligth of a Q-band module and a W-band feedhorn.

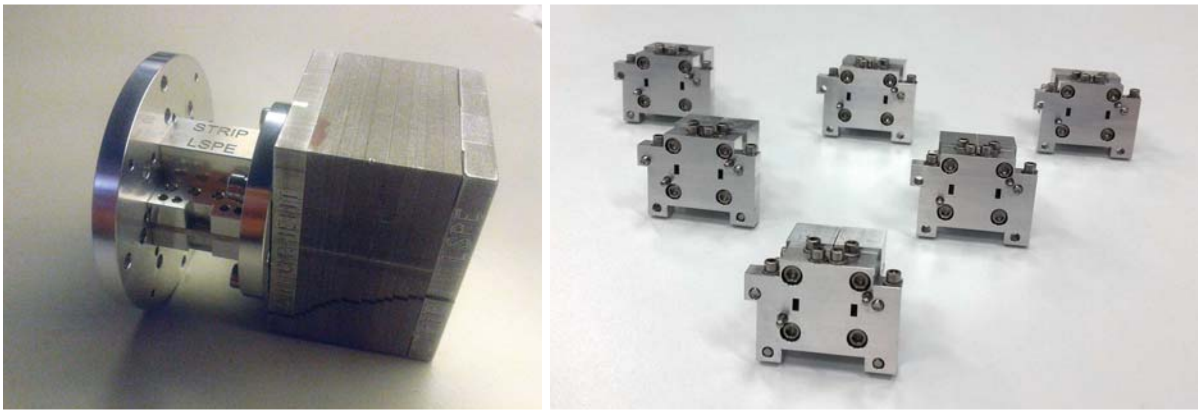

Figure 2.2: *Left*: Picture of the Q-band polarizer and the orthomode transducer assembly. *Right*: The six W-band septum polarizers.

which propagate through the polarimeter module. For the Q-band, a turnstile-junction orthomode transducer routes the two circular polarized signals to two different rectangular waveguides; whereas, for the W-band, each channel incorporates a septum polarizer. Fig. 2.2 shows one of the Q-band polarizer/OMT assembly (left panel) and the complete set of W-band septum polarizers (right panel). The Q-band turnstile-junction orthomode transducers are based on the layout reported in Virone et al. (2014), and have been manufactured using the platelet technique with 1 mm-thick layers. This architecture shows a very good measured performance in terms of transmission (≥ -0.5 dB), reflection (< -25 dB), cross-talk (~ -40 dB) and leakage from intensity to polarization (~ -30 dB). The W-band septum polarizers are characterized by a reflection of < -20 dB and a leakage of intensity to polarization of the order of ~ -13 dB (Chen et al. 2014).

The polarimeters are based on the design developed for the QUIET ground-based experiment (Cleary 2010). They rely on cryogenic High Electron Mobility Transistor (HEMT) low noise amplifiers and on high-performance waveguide components cooled to 20 K and integrated in Monolithic Microwave Integrated Circuits (MMIC). The polarimeter design implements a double modulation scheme to minimize residual systematic effects. This strategy allows to recover both Q and U Stokes parameters from a single measurement, after combining the two linearly polarized components of the input field

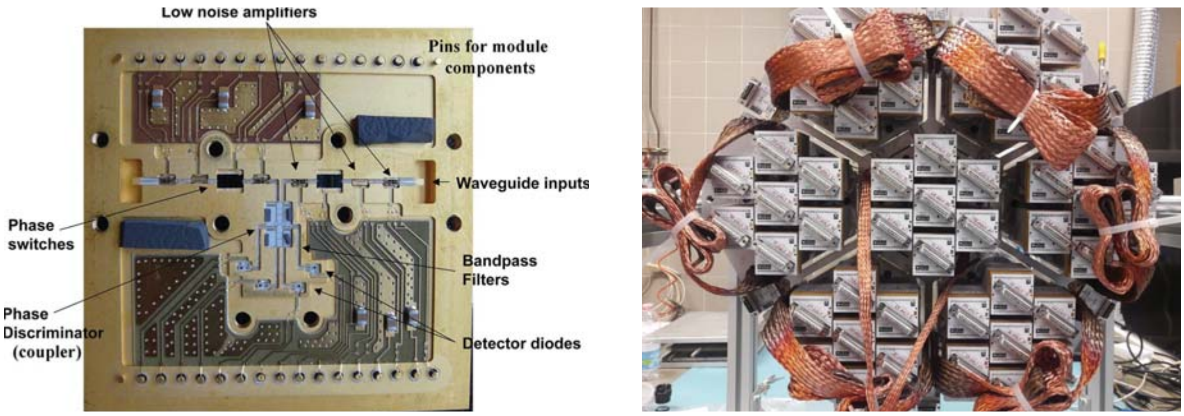

Figure 2.3: *Left*: Internal view of a Q-band polarimeter module. Each correlation unit is packaged into square brass modules about 1 cm thick with a footprint of 5×5 cm^2 in Q-band. *Right*: Polarimeters integrated in the focal plane unit during system level tests. The picture shows also the Copper thermal harness.

into left and right circular polarization components using phase switches and hybrid couplers. There are two different kinds of demodulation: a fast (~ 4 kHz) demodulation, which allows to remove effectively the effect of amplifier gain fluctuations, and a slow (~ 50 Hz) demodulation, which removes any $I \rightarrow Q, U$ leakage arising from asymmetries in the phase switches attenuation. Fig. 2.3 shows the details of a correlation unit and the full set of polarimeters integrated in the focal plane unit at OAS-INAF in Bologna during system level tests.

The Strip electronics provides the full biasing and acquisition of the 55 polarimeters on the focal plane. It consists 7 pairs of boards that drive and acquire data from 8 polarimeters each. Each pair contains one bias board and one Data AcQuisition and logic board (DAQ). The DAQ boards interact with the main computer via telemetry telecommands and acquire the data generated by the four detectors of each polarimeter. They acquire data from 32 detectors at a rate of 1 MHz, demodulate the scientific data at 4 kHz, and send the data via Ethernet to the main computer for storage.

Each complete polarimetric chain, from the feedhorn to the detectors, is placed inside a dewar surrounded by a radiative shield cooled to 80 K. Copper thermal straps connect the focal plane and the cooler cold head allowing the polarimeter chain to be cooled down to 20 K. The cryostat aperture is an ultra-high molecular weight polyethylene (UHMWPE) window followed by 13 IR filters at 150 K (one filter for each horn at 95 GHz and one filter for each 7-horns module at 43 GHz) to reduce the radiative load from the 300 K environment. The cryostat is placed in the focal region of the telescope.

Strip will use the same telescope that was originally designed and built for the CLOVER experiment (North et al. 2008): a Dragonian side-fed dual-reflector system with a projected diameter aperture of 1.5 m. The telescope is surrounded by a co-moving baffle made of aluminum plates coated with a millimetre-wave absorber, which reduces the contamination due to straylight. The optical assembly is installed on top of an alt-azimuth mount, which allows the rotation of the telescope around two perpendicular axes to change the azimuth and elevation angle. An integrated rotary joint will transmit power and data to the telescope and the instrument, and will allow a continuous spin as required by the scanning strategy. The telescope is provided also with a star tracker that will be used to determine the instantaneous pointing direction of the telescope by looking at stars in the sky. Fig. 2.4 shows a general view of the Strip telescope.

The telescope will scan the sky at a constant zenith angle, nominally 20°, with 1 r.p.m.

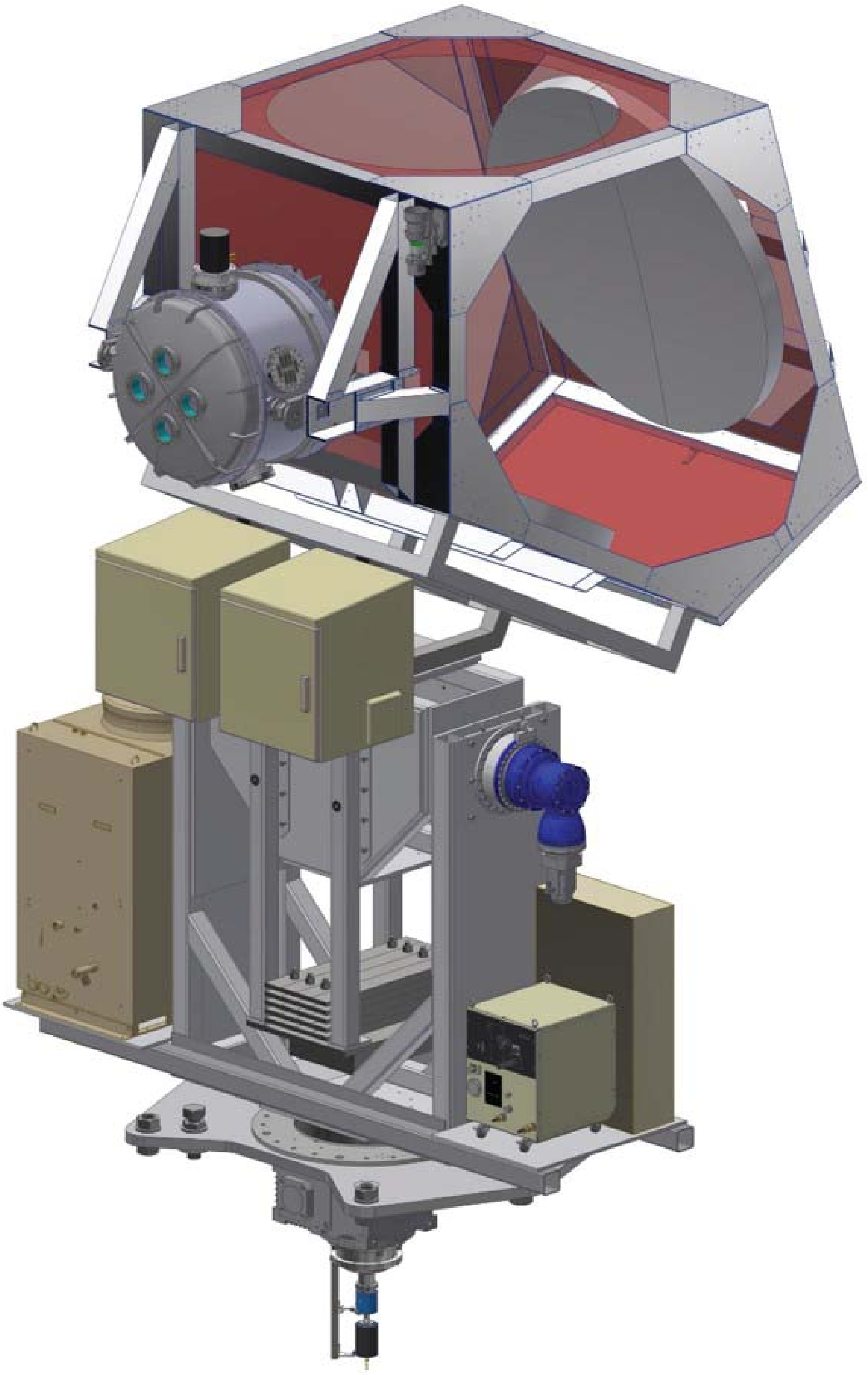

Figure 2.4: Model of the Strip telescope. The mirrors are held inside a co-moving baffle which is lined with absorber to reduce the effect of sidelobes. A counter balance will be mounted on the opposite side of the elevation axis from the telescope. All of the instrument hardware shown here is either built or under construction.

	43 GHz	95 GHz
Atmospheric emission at Zenith (K_{RJ})	16.3	19.0
CMB (K_{RJ})	1.8	1.1
Mirror emission (K_{RJ})	3.0	3.0
Cryostat window (K_{RJ})	3.0	8.0
IR Filters (K_{RJ})	2.0	3.0
Feed system (K_{RJ})	0.5	0.5
Polarimeter noise (K_{RJ})	34.0	104.2
System temperature (K_{RJ})	61.7	140.0

Table 2.2: White noise sensitivity budget of Strip receivers.

spin rate. This strategy will allow the minimization of atmospheric effects and a coverage of about 38% of the Northern sky, thus ensuring a large overlap with the SWIPE observations.

The ambitious science goal of Strip means that the requirements on sensitivity and control of systematic errors are extremely stringent. To reach the necessary sensitivity across the survey areas in a reasonable integration time, the system noise must be reduced to the minimum level. This results in stringent requirements on the detector noise, the instrument efficiency and on the spillover from the optics. The main source of noise when Strip will observe the sky are fluctuations in the receiver gain and variations in the atmospheric load. Table 2.2 reports the contributions that lead to our current estimate of the average receiver white noise performance. Assuming a constant azimuthal angle of 20° during the whole survey, we get a sensitivity per polarimeter per second of 514.6 $\mu K_{RJ}\ s^{1/2}$ (Q-band) and 1139.5 $\mu K_{RJ}\ s^{1/2}$ (W-band).

2.2 Strip telescope design

The Strip telescope is a Dragonian side-fed dual-reflector system with a projected diameter aperture of 1.5 m. This design gives exceptionally low aberrations and cross-polarization across a large focal plane, allowing a large number of detectors to be fed directly without requiring additional focusing optics that may introduce aberrations, cross-polarization or a complex curved focal plane. The Dragonian configuration is the best in terms of polarization purity and symmetry over a wide focal region[2]. The primary mirror has an offset parabolic shape, with a 1500 mm diameter. The secondary mirror is an offset concave hyperboloid, with a 859.88 mm $\times$ 829.35 mm wide elliptical rim. The telescope provides an angular resolution of $\sim$ 20 arcmin in the Q-band and $\sim$ 10 arcmin in the W-band.

The entire dual-reflector system has an equivalent focal length of 2700 mm, resulting in an F-number 1.8 (for a definition of the telescope descriptive parameters see Appendix A.1). This is a typical value for Dragone-Mizuguchi crossed configurations because of the specific design that imposes a long equivalent focal length in order to have the secondary focus accessible.

---

[2] We recall that the Dragone-Mizuguchi condition ensures that it is always possible to arrange an arbitrary number of confocal reflectors (paraboloids, ellipsoids, hyperboloids) so that they guarantee circular symmetry and absence of cross-polarization in the antenna far-field (Dragone 1978), neglecting effects due to edges diffraction. This condition is satisfied by a feedhorn placed in the focal point of the optical system: an off-axis placement (as in the case of an array of feedhorns) will divert the system from the ideal case.

The whole feedhorn array is placed in the focal region of the telescope, ensuring no obstruction of the field of view. All the modules are optimally oriented according to the shape of the focal surface, with illumination centred on the primary mirror. The two mirrors determine the main beam shapes of the Strip detectors, while the shielding structure that surrounds the mirrors affects the near and far sidelobes.

Mirrors have been designed and manufactured by University of Oxford. Each mirror is machined from a single piece of aluminium and the back of the mirror is lightweighted by machining away most of the backing material, leaving some ribs to provide structural strength and location for three adjustable mounting points per mirror. Both mirrors are attached to the optical assembly by three attachment interface points. The typical roughness of the mirror surface is designed to have a peak-to-peak error within $\pm 50\ \mu$m.

Besides the mirrors, the Strip optics includes also the feedhorn array, the cryostat vacuum window, the IR filter, the co-moving shielding structure and the alt-azimuth mount. By definition, the mount moves around the vertical axis (azimuth) and around the horizontal axis, the elevation (alt-axis). It can move endlessly around the vertical axis with a speed of 6°/s, while the elevation angles can range between 5° and 50° of zenith angles.

2.2.1 Optical requirements

The quality of an antenna as direction measuring device depends on how well the power pattern is concentrated in the main lobe peak direction, i.e. the electrical boresight (IEEE Std 145-2013). Ideally, we would like to have the radiation coming from the line of sight direction as the unique contribution to the measured signal; however, due to diffraction effects and unwanted multiple reflections, we receive a signal also from angular regions far from the pointing direction of the instrument. These regions are called sidelobes. The received power coming from the regions outside the main beam is one of the major sources of systematic effects concerning the optics.

The optical system introduces systematic errors, due to its imperfection or its configuration. It introduces also beam distortions associated with aberrations. These effects affect the angular resolution. We would like to have a symmetric beam, possibly Gaussian in shape, to avoid effects due to distortions and without spillover to avoid straylight entering the receiver from the sidelobes. Moreover, the main beam shape is expected to be frequency dependent within the bandwidth of each detector because of the different response of feedhorns with the frequency and the different telescope diameter with respect to the wavelength. For these reasons it is important to simulate the optics response and optimize its performance.

The main requirements on the Strip optics are a cross-polarization discrimination better than -30 dB and a sidelobe rejection level better than -55 dB in the near lobes region ($0.5^\circ < \theta < 5^\circ$) and better than -65 dB in the far sidelobe region ($\theta > 5^\circ$).

We simulated the performance of the optical system with the software GRASP, developed by TICRA. The electromagnetic model I have developed and used for the simulations of the optical response is presented in the next section.

2.3 Electromagnetic modelling

Strip optics have been modelled with the software GRASP, developed by TICRA, which is the standard design tool for reflector antennas. A detailed description of its functions and simulation methods can be found in Appendix B.

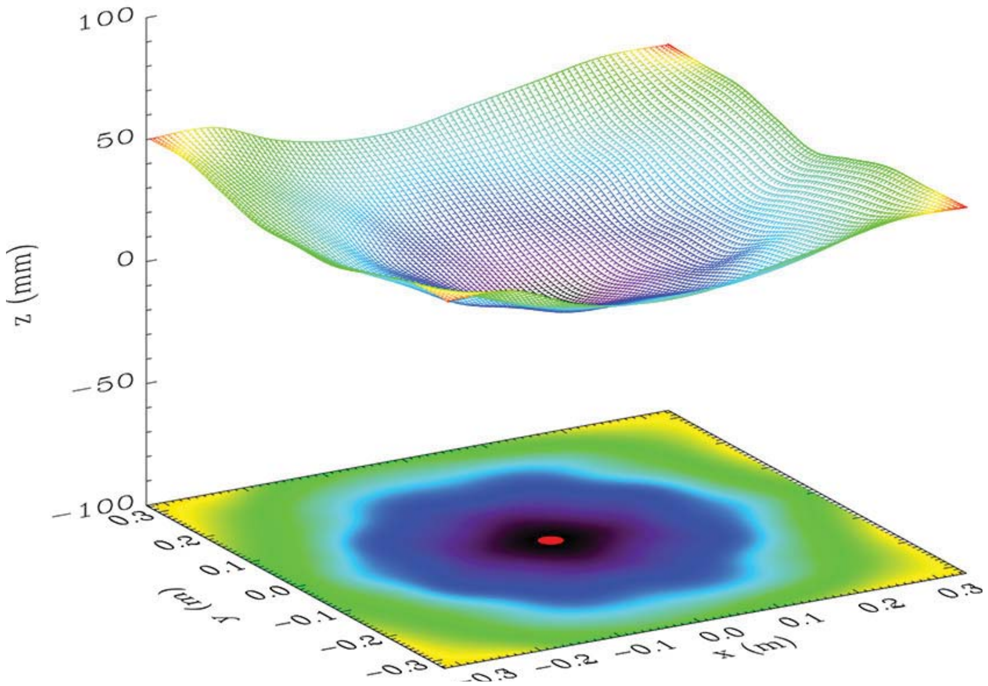

Figure 2.5: Focal surface of the Strip dual-reflector telescope.

The simplest model includes the two reflectors described by their nominal surface and illuminated by the forty-nine Q-band and six W-band feedhorns. A detailed analysis with this configuration had already been performed. However, within this simple model there are some non-negligible approximations: it considers an ideal optics and neglects the obstruction caused by the optical shields.

During my PhD, I tried to upgrade the simplest model by including other elements that affect the angular response of the optics. More specifically, I added to the model the shielding structure with its circular aperture, the IR-filters, the cryostat window and the effect of possible distortion of the mirrors surfaces (refer to Fig. 2.7 for the sketch of the model). Hereafter, I report a description of each electromagnetic element constituting the complete electromagnetic model.

2.3.1 Feedhorns

The telescope is illuminated by the array of dual-profiled corrugated feedhorns, where the corrugation profile is a mixture of a sine-squared section, starting from the throat, and an exponential section near the aperture plane. The feedhorns are placed on the telescope focal surface (see Fig. 2.5), which has been retrieved using the software package WaFER (Wave Front Error evaluatoR). WaFER implements a method to define and characterize the focal surfaces of millimeter wave telescopes by minimizing the variance of the optical path lengths weighted with a feedhorn pattern. It can be used to define the focal surface of any reflector antenna system that can be studied with GRASP (Sandri et al. 2012).

The feedhorns are oriented to center the telescope illumination on the primary mirror, so that an optimum spillover is obtained while guaranteeing low level of cross-polarization contamination. The feedhorn modules are also focused along their axis to

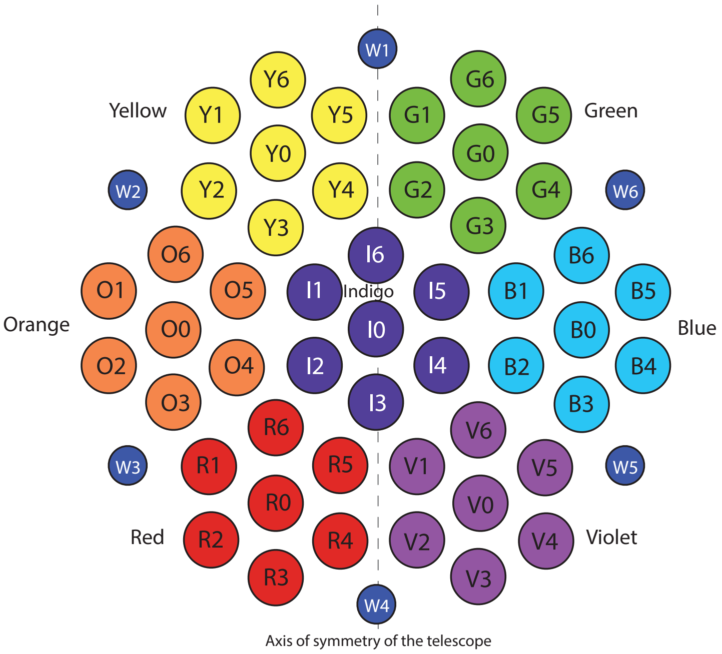

Figure 2.6: Strip feedhorns naming convention. Each Q-band feedhorn is identified by the capital letter of the module color, followed by a number from 0 to 6 in the specified order. Each W-band feedhorn is identified by W followed by a progressive number from 1 to 6. The plane of symmetry of the telescope passes through the vertical axis of the array.

optimize the near sidelobe response, i.e. we searched for the position with the lowest near lobes level.

We decided to use a naming convention in order to identify each feedhorn on the focal plane. We identify the seven modules with a color of the rainbow (Red, Orange, Yellow, Green, Blue, Violet, Indigo), and we associate a number to each feedhorn in a module, so that each horn antenna is identified by the capital letter of the color, followed by a number from 0 to 6; e.g. the central horn of the central module is called I0. The reference focal plane layout is reported in Fig. 2.6.

We performed simulations of the feedhorn radiation pattern with the software SRSR-D, which provides a rigorous simulation of the electromagnetic performance of any structure with symmetry of revolution. For a detailed description see Section 3.1. The Q-band feedhorns have already been fully characterized in terms of their radiation pattern with simulations and measurements performed in the anechoic chamber at the University of Milan. All co-polar radiation patterns agree with simulations within 0.5 dB in the main beam region (in the angular range $\pm 15°$) with sidelobe level < -25 dB and cross-polarization level < -35 dB over the whole frequency band (Franceschet et al. 2018). The measurement of the W-band feedhorns has been part of my work and a more detailed analysis is reported in Section 3.1.1. Each feedhorn is defined in GRASP as a far field tabulated pattern, which allows an accurate description of the radiation pattern.

2.3.2 Mirrors

As we said in Section 2.2, the mirrors of the Strip telescope are arranged according to a Dragonian design, and placed so that their foci coincide. The Dragonian configuration is the best telescope design for high-accuracy CMB measurements in term of flatness of the

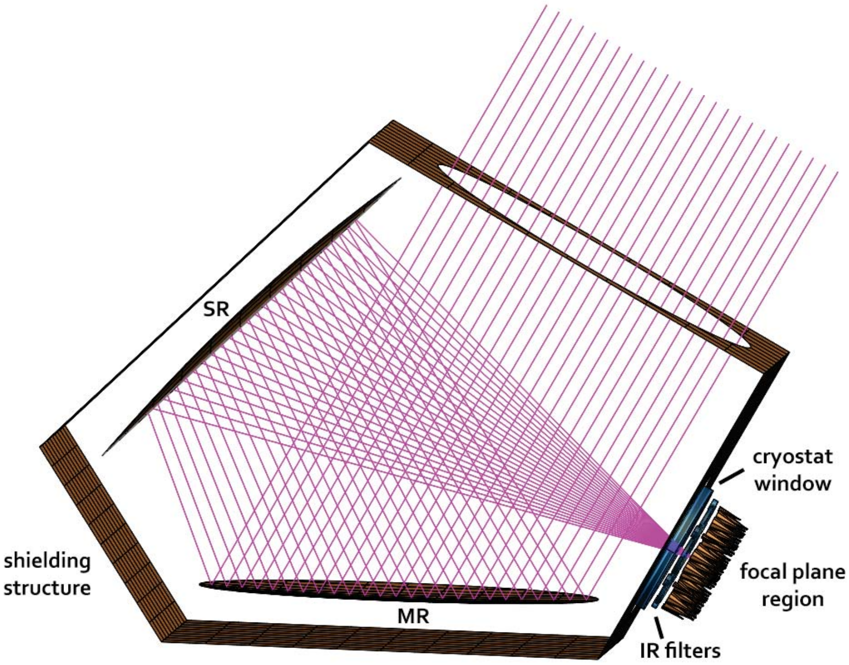

Figure 2.7: Electromagnetic model of the Strip telescope implemented with GRASP. It includes the parabolic main reflector (MR), the hyperbolic sub-reflector (SR), the forty-nine Q-band, the six W-band feedhorns, the shielding structure with the circular aperture, the cryostat vacuum window and the IR filters. The rays show the ideal optical path of radiation when the central feedhorn is considered as the source.

focal surface, feed tilting, extension of the field of view, cross-polarization and sidelobes level. That is because the Dragone-Mizuguchi condition (Dragone 1978) ensures that it is always possible to arrange an arbitrary number of confocal reflectors so that they guarantee circular symmetry and absence of cross-polarization in the antenna far-field. This condition is satisfied by a feedhorn placed in the focal point of the optical system, instead an off-axis position will divert from the ideal case. Therefore, this configuration guarantees low sidelobes and low cross-polarization over a large and flat focal plane (with respect to the telescope dimensions). However, the limitation of this layout is the constraint on the focal ratio, which cannot practically be lower than 2. As shown in Fig. 2.7, the incoming radiation is reflected from the primary mirror, then from the secondary mirror and finally reaches the feedhorns placed in the focal plane of the optical system.

The main reflector surface is a paraboloid of revolution with a projected diameter of 1.5 m. The surface is defined by the equation

$$z_p = \frac{(x-x_0)^2 + (y-y_0)^2}{4f} + z_0, \tag{2.1}$$

where x and y are given in the reference frame of the primary mirror. The primary mirror is not considered as the aperture stop because of the presence of a circular aperture with the same diameter on the top of the shielding structure which surrounds the mirrors (see Fig. 2.7). The sub-reflector surface is an hyperboloid, defined as

$$\frac{(z_h - c)^2}{a^2} - \frac{x^2+y^2}{b^2} = 1, \qquad \text{with} \quad b = \sqrt{c^2-a^2}, \tag{2.2}$$

where a is the distance between one of the vertices and the centre, and c is the distance

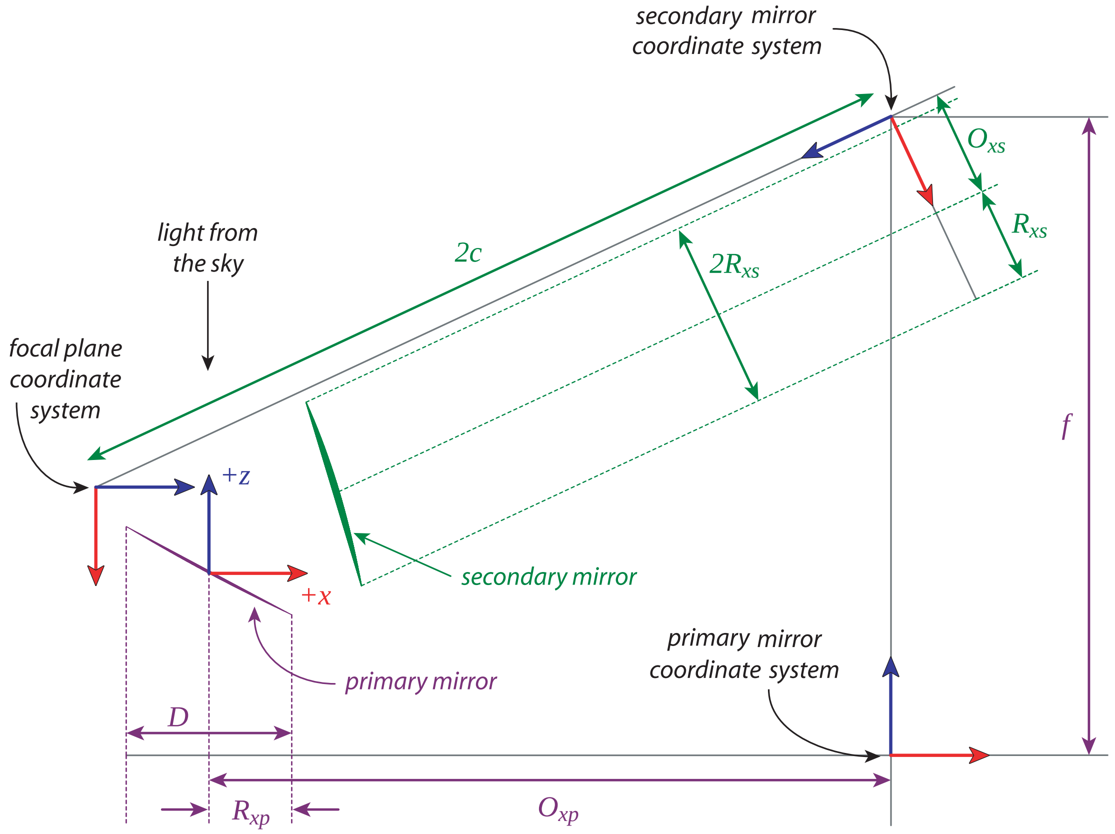

Figure 2.8: Cross-sectional view of the telescope mirrors. Various coordinate systems and construction parameters are defined in this figure. All coordinate systems are right handed. The values of the construction parameters are given in Table 2.3.

between one of the foci and the centre. Here, x and y are given in the reference frame of the secondary mirror. For clarity, various parameters and coordinate systems are defined in Fig. 2.8. The eccentricity of the hyperboloid is given by $\varepsilon = c/a$ and it was selected to satisfy the Mizuguchi condition.
The mirror rims are ellipses defined in the reference frame of each mirror as

$$\frac{(x - \mathcal{O}_x)^2}{\mathcal{R}_x^2} + \frac{(x - \mathcal{O}_y)^2}{\mathcal{R}_y^2} = 1. \tag{2.3}$$

The key parameters of the design of the telescope are given in Table 2.3.

The shielding structure which surrounds the reflector is made of aluminum plates coated by a millimetre-wave absorber. It has been modelled as a series of plane reflectors with the appropriate rim, except for the top panel, which is characterized by the presence of a circular aperture. The aperture has a radius of 770 mm and it has been modelled in GRASP as an “Aperture in Screen” object. This class defines an aperture in an infinite conducting screen and it is useful for modelling an optical aperture stop. The scattering from the aperture is determined by means of Babinet’s principle (Pontoppidan 2008).

2.3.3 IR filters and cryostat window

The 13 IR filters at 150 K (one filter for each horn at 95 GHz and one filter for each 7-horns module at 43 GHz) and the cryostat vacuum window are made of ultra-high molecular weight polyethylene (UHMWPE) to have a very low absorption coefficient. They have

Parameters	Value
Projected aperture D	1500 mm
Equivalent focal length	2700 mm
F/#	1.8
Primary-secondary angle	$65°$
Feed-secondary angle	$25°$
Primary focal length f	5790 mm
Primary offset $\mathcal{O}_{xp}$	-6180 mm
Secondary foci distance $2c$	7950 mm
Secondary vertex distance $2a$	-3845 mm
Secondary eccentricity	-2.0674419

Table 2.3: Parameters of the Strip telescope.

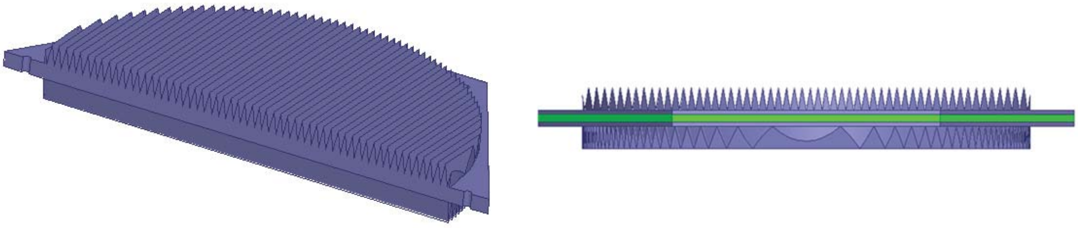

Figure 2.9: IR filter including the perpendicular triangular AR coating and the core homogeneous slab (in green).

been designed at the Universidad de Chile (UdC), which provided the model, the geometrical and electrical parameters of these optical elements. The dielectric constant, ϵ_r, of UHMWPE is 2.32, while the loss tangent, $\tan\delta$, is 10^{-4} in the Q-band and $1.3 \cdot 10^{-4}$ in the W-band.

All the filters and the window are designed with a triangular coating, which is used to increase the throughput and reduce reflections. Each filter consists of a core homogeneous slab with a triangular coating on both sides (see Fig. 2.9). The optimized coating for the filters shows reflection losses lower than -31 dB and -27 dB for Q and W bands, respectively. The window is designed to have return losses lower than -25 dB for both frequency bands and a cross-polarization lower than -50 dB with an average of -72 dB.

These objects are modelled in GRASP as "Simple Lens" objects, which specify a homogeneous dielectric scatterer, with rotationally symmetric surfaces. The geometrical parameters used in the model are reported in Table 2.4.

A detailed analysis of the effect of the filters and window is presented in Section 3.3.

Parameter	Q-band filter	W-band filter	Window
Diameter (mm)	170	52	586
Dielectric constant	2.32	2.32	2.32
Refractive index	1.52	1.52	1.52
Loss tangent	10^{-4}	$1.3 \cdot 10^{-4}$	10^{-4}
Thickness (mm)	6	17.32	43

Table 2.4: Parameters used to define the IR filters and the cryostat window.

CHAPTER 3

Strip main beams

CMB polarization experiments like Strip require the use of several feedhorns coupled to a telescope to obtain high sensitivity measurements with sub-degree angular resolution. However, non-idealities in the optical system may introduce limitations in achieving high degree of accuracy, if not well understood and controlled. For this reason, I used electromagnetic simulations to study the optical design of Strip, its characteristics in terms of angular resolution, main beam symmetry, polarization purity and feedhorns orientation.

In this chapter, I introduce the electromagnetic characterization of the Strip feedhorns, which is essential to assess the optical response of the telescope when they are placed on its focal surface. Then, I present the characterization of the Strip optical system in terms of main beams. The analysis takes into account also the effect of the IR filters and the cryostat window on the shape of the feedhorn radiation pattern. Eventually, I analyse the effect of possible imperfections of the mirrors on the main beams descriptive parameters.

3.1 Strip feedhorns

The electromagnetic design of Strip feedhorns, resulting in a corrugated profile, has been already discussed in Section 2.1. Here we recall only that the Q-band feedhorns operate in the frequency range 39–48 GHz, while the W-band feedhorns operate in the frequency range 85–104 GHz.

The mechanical design of the 7-elements module is based on the array presented in Del Torto et al. (2013), whereas the W-band feedhorns have been designed to have approximately the same length of the Q-band modules, i.e. the same beam width. This choice has been made due to mechanical constraints, since we want to avoid possible mechanical interference with the IR filters. This leads to a telescope angular resolution in the W-band which is approximately the half of the resolution in the Q-band. Both the electromagnetic design and mechanical drawings have been provided by IASF-BO.

All the feedhorns have been realized using the platelet technique, which consists in constructing the mechanical profile of the horn by stacking up metallic plates. Each plate is properly machined so that it represents a tooth and a groove of a corrugation of the feedhorn. The main advantages of this technique are the reduced manufacturing costs and time when compared to traditional techniques such as electroforming. This makes platelet technique attractive for the production of large arrays of feedhorns. As an example, Fig. 3.1 shows the geometry of the W-band dual-profiled corrugated horns. Each plate has been measured by means of a CNC metrology machine *Werth Scope Check 200* (1.8 μm accuracy in xyz axes) in order to verify the machining tolerance.

Figure 3.1: Corrugation profile of the W-band Strip feedhorns, composed by a squared-sine section joined to an exponential one towards the horn aperture.

Frequency (GHz)	FWHM (°)	$\mathcal{D}$ (dBi)	XPD (dB)	RL (dB)
43	6.1526	23.93	-42.19	-66.81
95	6.3172	23.58	-52.91	-28.82

Table 3.1: Main parameters of the feedhorn radiation pattern at their central working frequency. The full-width half- maximum (FWHM) is the average value between the minimum and maximum of the beam width at -3 dB. We report also the directivity ($\mathcal{D}$), the return loss (RL) and the cross-polarizarion discrimination factor (XPD).

We performed the simulations of the radiation pattern with the software SRSR-D developed by Orange Telecom. The software provides a rigorous simulation of the electromagnetic performances of any structure with symmetry of revolution consisting of conducting parts and homogeneous dielectric domains. It provides reliable and accurate simulations and it has been successfully used in the design of Planck LFI corrugated feedhorns.

Figures 3.2 and 3.3 show the radiation pattern simulation at 43 GHz (Q-band horn) and 95 GHz (W-band horn), respectively. Each plot includes the expected radiation pattern on the co-polar principal planes (E-plane, H-plane and 45°-plane) and cross-polar 45°-plane. The main parameters that characterize the radiation patterns are reported in Table 3.1. These radiation patterns are used to define the feedhorns in the GRASP simulation software.

The Q-band feedhorns have already been fully characterized in terms of their radiation pattern and return loss with measurements performed in the anechoic chamber at the Physics Department of the University of Milan, showing a remarkable agreement between measurement and simulation (Franceschet 2016). The W-band feedhorns have been measured in the context of this thesis. The test procedure and results of the measurements are reported in the following section.

The performance of the Strip focal plane unit has been optimized by positioning the feedhorn modules according to the evaluated focal surface. We settled the modules and horns of the Strip focal plane on the telescope focal surface, with the corresponding

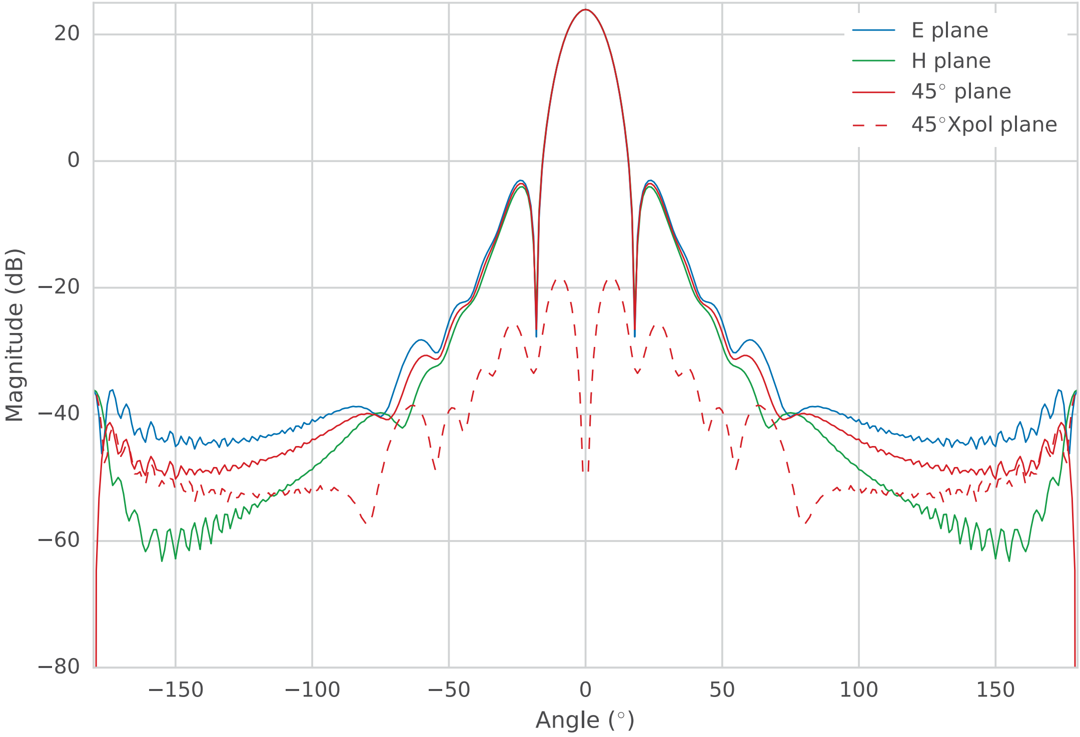

Figure 3.2: Simulated radiation pattern of the Strip Q-band feedhorn at 43 GHz.

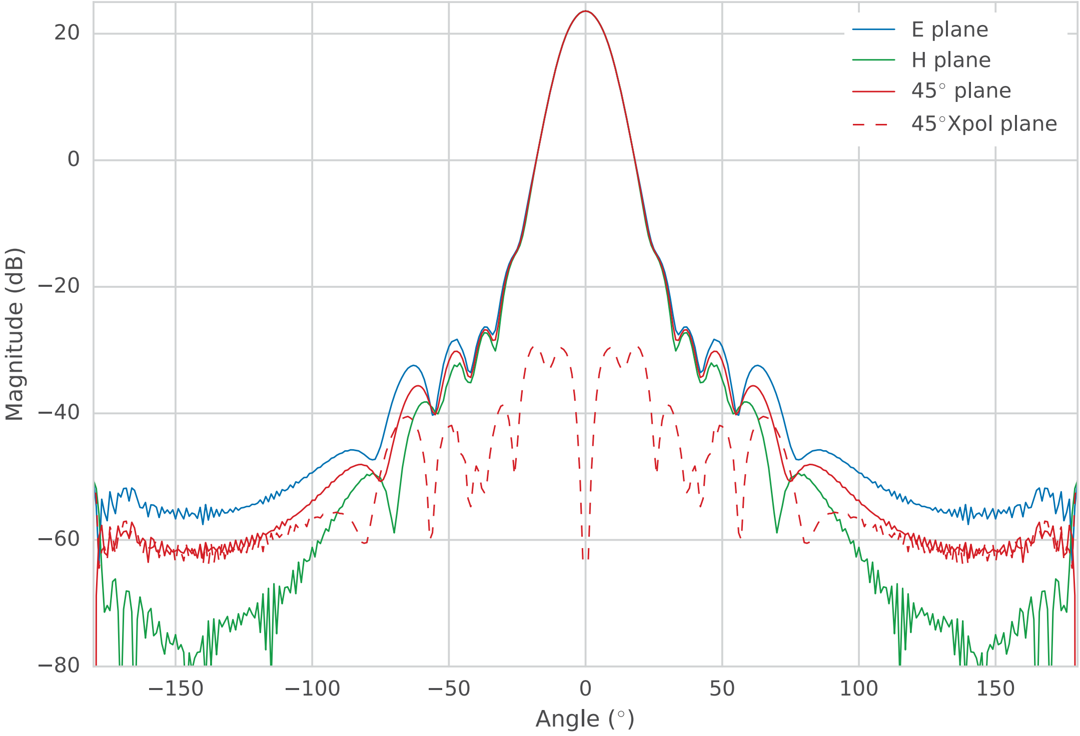

Figure 3.3: Simulated radiation pattern of the W-band feedhorn at 95 GHz.

Module	Location			Orientation		
	x_{RDP} (mm)	y_{RDP} (mm)	z_{RDP} (mm)	θ_{RDP} (°)	ϕ_{RDP} (°)	ψ_{RDP} (°)
I	0.00	0.00	14.34	0.00	0.00	0.00
B	0.00	-177.82	16.75	2.25	90.32	0.10
Y	153.99	88.91	14.76	2.28	-150.16	-0.31
O	0.00	177.82	16.75	2.25	-90.32	-0.10
V	-153.99	-88.91	15.37	2.23	30.17	-0.24
R	-153.99	88.91	15.37	2.23	-30.17	0.24
G	153.99	-88.91	14.76	2.28	150.16	0.31

Table 3.2: Location and orientation of the Q-band modules with respect to the RDP and according to GRASP angle definition.

Horn	Location			Orientation		
	x_{RDP} (mm)	y_{RDP} (mm)	z_{RDP} (mm)	θ_{RDP} (°)	ϕ_{RDP} (°)	ψ_{RDP} (°)
W1	238.70	0.00	23.93	3.05	-120.31	0.11
W2	119.35	206.72	24.60	3.05	-120.31	59.99
W3	-119.35	206.72	22.76	3.00	-60.32	120.00
W4	-238.70	0.00	24.53	2.97	0.00	-179.79
W5	-119.35	-206.72	22.76	3.00	60.32	-120.00
W6	119.35	-206.72	24.60	3.05	120.31	-59.99

Table 3.3: Location and orientation of the W-band feedhorns with respect to the RDP and according to GRASP angle definition.

average orientation towards the main reflector center, so that an optimum spillover level is obtained while guaranteeing low level of cross-polarization contamination.

In the electromagnetic model, each main beam coordinate system is defined starting from the line of sight in the following way: the z-axis points towards the center of the beam, the x-axis points towards the principal polarization axis defined as the projection on the sky of the x-axis of the feedhorn coordinate system. The final position of the Q-band modules and W-band horns and the corresponding z-unit vector components, giving the orientation of each module in the focal plane, is reported in Tables 3.2 and 3.3. The angles and locations are given with respect to the Reference Detector Plane (RDP) system and according to GRASP angle definition (for more details see Appendix B.1).

3.1.1 W-band measurements

During my PhD, I performed a characterization of the six W-band feedhorn array (plus a spare unit), which has been developed by the Physics Department workshop of the University of Milan. The test plan involves the characterization of the antenna return loss and radiation pattern.

We measured antenna radiation patterns for five frequencies over the W-band:

- 85 GHz (f_0-10%)
- 90 GHz (f_0-5%)
- 95 GHz (f_0%)

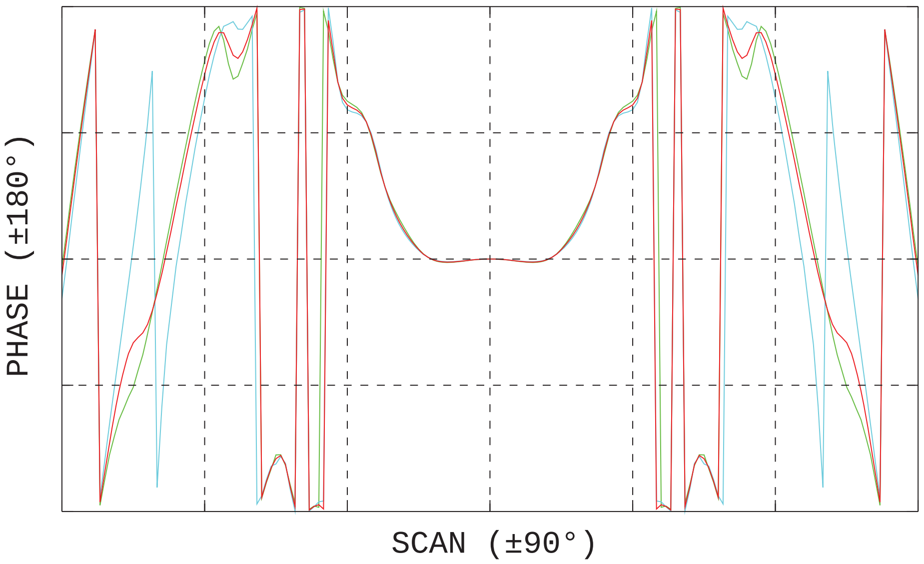

Figure 3.4: Simulated phase diagram at 95 GHz, when the phase center is placed at 11.8 mm from the aperture plane of the feedhorn. E plane phase is shown in green, the H plane in blue and the $45°$ plane in red.

- 100 GHz (f_0+5%)
- 105 GHz (f_0+10%)

Each horn has been characterized on three co-polar planes and one cross-polar plane:

- Copolar E plane (nominal and flipped)
- Copolar H plane (nominal and fliped)
- Copolar $+45°$ plane
- Cross-polar $+45°$ plane

We collected a total amount of 210 radiation patterns: 6 planes at 5 frequencies for all seven feedhorns (six nominal and one spare). In the following, we report an analysis of the measurements performed at the central (f_0) and side-band frequencies ($f_0\pm$ 5% and $f_0\pm$ 10%), comparing measurement and simulation.

Electromagnetic simulations have been used to find the position of the center of phase at the central frequency, by minimizing the phase diagrams variations (relevant to the three planes E, H and $45°$) in the angular region of the main beam, while moving the phase center location. We found that the phase center is placed 11.8 mm from the aperture plane of the horn for the central frequency 95 GHz[1]. Fig. 3.4 shows the corresponding phase diagram in the angular range $\pm 90°$. As we can see, the phase is stable in the main beam angular range (about $\pm 15°$) in all co-polar planes.

We performed beam pattern measurements in the far-field regime (distance between receiver and transmitter is about 1850 mm) in the anechoic chamber at the Physics Department of the University of Milan. The antenna under test has been positioned in the

---

[1] In principle, since the phase center changes with the frequency and with the azimuthal cut of the radiation pattern, a unique definition does not exist and in the real case it is an extended region rather than a well defined point.

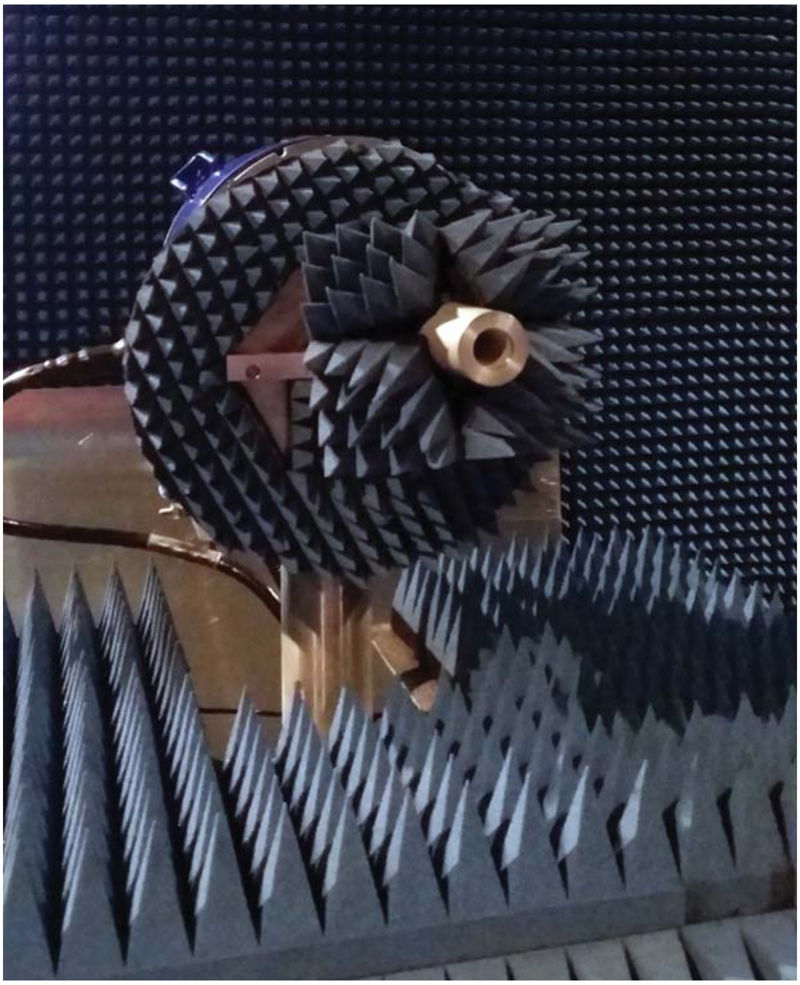

Figure 3.5: The antenna under test is mounted on the DUT mechanical support of the anechoic chamber. We used several Eccosorb panels as shields to get a cleaner measurement of the radiation pattern, without altering the feedhorn response with spurious reflections of the incoming signal.

facility with its phase center aligned to the azimuthal axis. The readout is performed by means of the vector scalar network analyzer MS4647B by Anritsu with Millimeter Wave extension modules. Fig. 3.5 shows the experimental setup, where one of the feedhorns is mounted on the DUT[2] mechanical support of the anechoic chamber.

We measured the return loss of the seven feedhorns in the frequency range 60-130 GHz, in order to increase the measurement resolution. We used a time gate starting from 6 mm in order to avoid the waveguide transitions effects. Fig. 3.6 shows the return loss measured for the seven horns compared with the simulation and it gives an indication of the repeatability of the device development.

From Fig. 3.7 to Fig. 3.9, we show a comparison between a limited set of measured radiation patterns for a single feedhorn at different frequencies compared with the corresponding simulations.

Measurements show that the main beams agree with the simulation, whereas the sidelobes show significant deviations. Moreover, analysing the results, we found that the beam peak deviates from the axis of the feedhorn, even if the mechanical alignment is optimized. Fig. 3.10 shows the dispersion of the beams pointing directions. In order

---

[2] Device Under Test

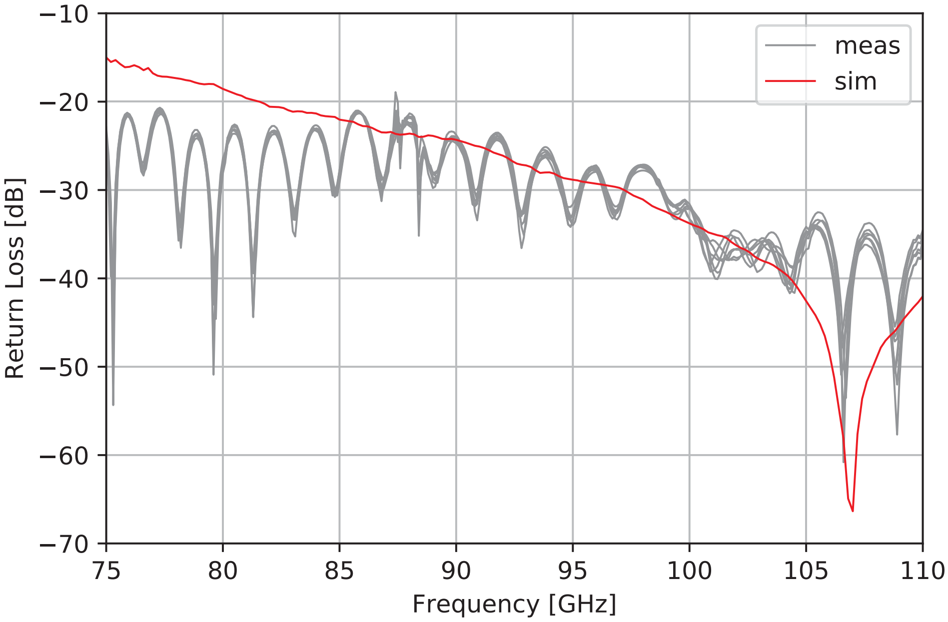

Figure 3.6: The seven grey lines show the return loss measurement for the seven W-band antennas. The red line shows the expected values from the simulation. The measurement shows a good agreement with one another, suggesting a good repeatability.

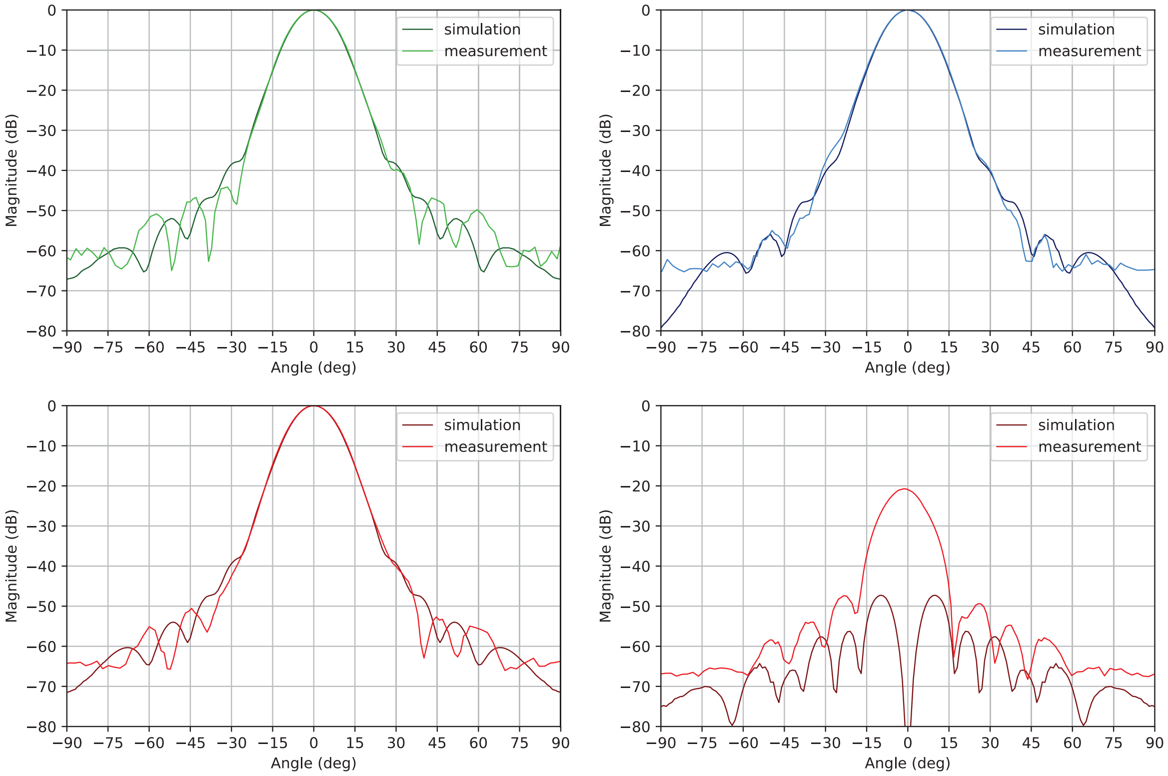

Figure 3.7: Measured beam patterns at 90 GHz compared with the simulation. *Top left*: copolar E-plane, *top right*: copolar H-plane, *bottom left*: copolar 45-plane, *bottom right*: cross-polar 45-plane.

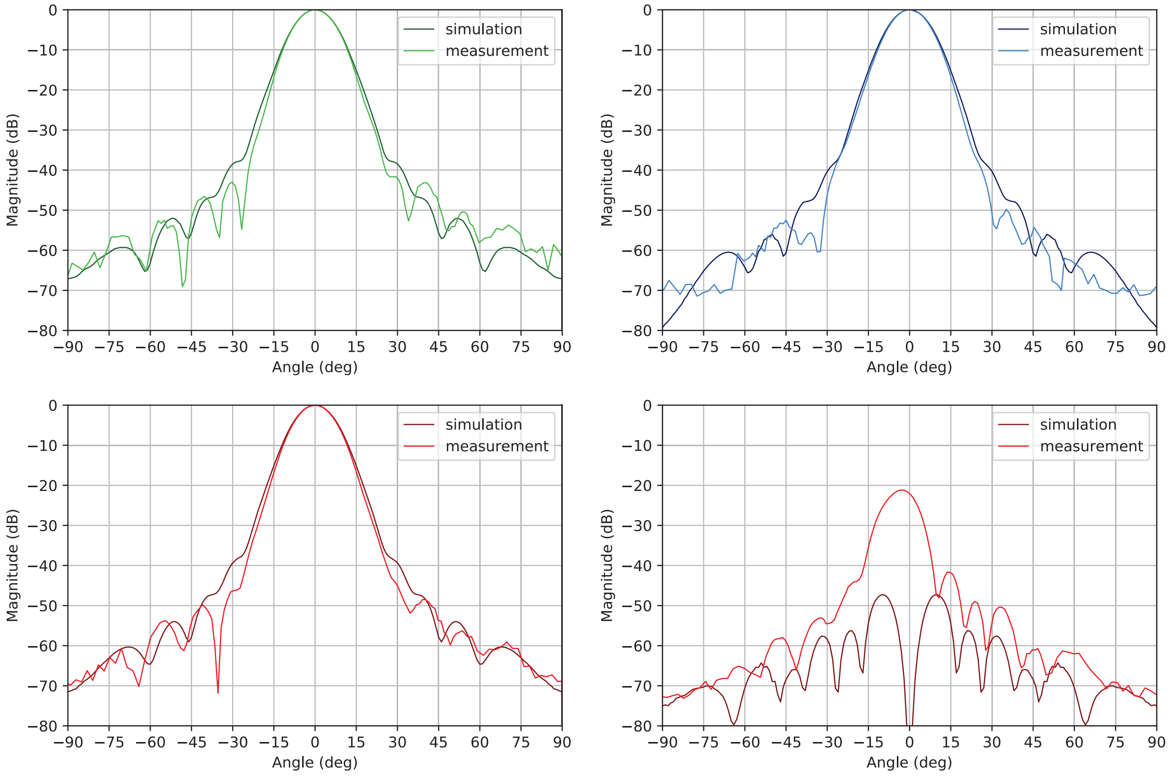

Figure 3.8: Measured beam patterns at 95 GHz compared with the simulation. *Top left*: copolar E-plane, *top right*: copolar H-plane, *bottom left*: copolar 45-plane, *bottom right*: cross-polar 45-plane.

to understand and check this problem, we made two measurements of the same plane flipping the feedhorn and this resulted in a change in the beam pointing direction. Fortunately, this problem will not affect significantly the pointing performance of the feedhorn when coupled with the telescope. This has been verified by means of electromagnetic simulations considering the worst case.

At the end of the test campaign, we found three non-compliances within the W-band feedhorns:

(i) co-polar radiation patterns differ from the simulation in the sidelobe angular region, i.e. $|\theta| > 30°$;

(ii) cross-polar radiation patterns differ from the simulation because of the presence of a strong (approx. -20 dB) co-polar component;

(iii) the feedhorns and their co-polar radiation patterns are not aligned with their nominal axis.

One of the possible causes could be the homemade circular to WR10 transition that we used in our setup. Moreover, we are comparing measurements with the simulation of the nominal design, which is slightly different from the built one due to thinner plates. Due to the manufacturing technique of the plates (chemical etching), each feedhorn is 2.25 mm shorter than expected, leading to a slightly different beam. This could justify the first non-compliance. The remaining problems might be due to the feedhorn plates misalignment. Eventually, we should also recall that cross-polarization measurements are very sensitive to systematic effects of the experimental setup, such as the non-ideal

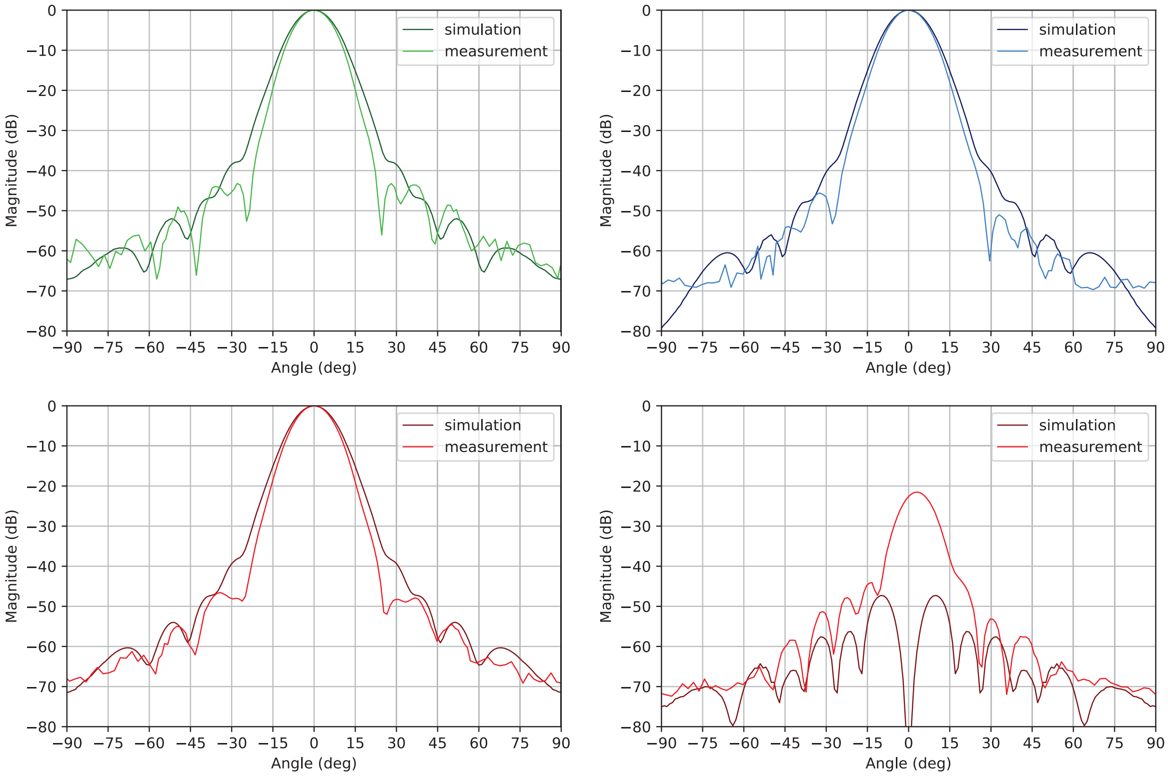

Figure 3.9: Measured beam patterns at 100 GHz compared with the simulation. *Top left*: copolar E-plane, *top right*: copolar H-plane, *bottom left*: copolar 45-plane, *bottom right*: cross-polar 45-plane.

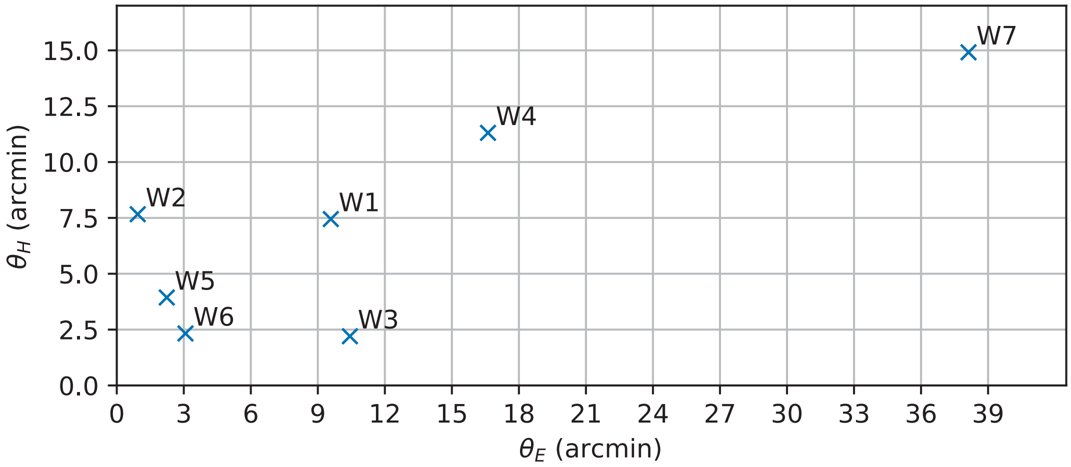

Figure 3.10: Angular dispersion of the beam pointing directions for the seven beams at 95 GHz. The W7 horn is the spare one.

alignment of the TX and DUT antennas polarization planes, and the polarization purity of the circular-to-rectangular waveguide transition downstream the antenna circular interface.

However, the overall performance of the W-band feedhorns is still acceptable to exploit this channel for atmospheric measurements: the sidelobe level is lower than -30 dB and the cross-polarization level is below -20 dB. Moreover, even if measurements differ from simulations, we accurately characterized the main beam so that we can use this information in the data analysis and remove or take into account the non-idealities.

3.2 Main beam definition and analysis method

To describe the performance of an antenna, we need to define some parameters. One of the most important is the radiation pattern, which is a measure of the response of the antenna to radiation as a function of space coordinates. It is a dimensionless quantity and it can be normalized so that the maximum value is unity. According to the reciprocity theorem, the radiation pattern is the same for both receiving and transmitting conditions. The power pattern is usually plotted in a logarithmic scale, i.e. in decibels (dB). This scale is usually desirable because a logarithmic scale can accentuate the details of those parts of the pattern that have very low values.

The pattern commonly consists of a number of lobes. The lobe containing the direction of maximum radiation is called main lobe or *main beam*. The smaller lobes are referred to as minor lobes or *sidelobes*. An in-depth description of radiation pattern properties is given in Appendix A.

The quality of an antenna as direction measuring device depends on how well the power pattern is concentrated in the main beam. Minor lobes usually represent radiation in undesired directions, and they should be minimized. The light that travels through paths different from the designed one is called straylight. Usually, it is the received power coming from regions outside the main beam and it is one of the major source of systematic effects in CMB observations. A detailed characterization of the main beam is indispensable to determine the performance of the optics in terms of angular resolution, beam symmetry, polarization purity and feedhorns orientation.

We performed optical simulations considering the horn as a source and computing the pattern scattered by both reflectors on the far-field using GRASP, a software developed by TICRA (Copenhagen, DK) for the analysis of general reflector antennas.

The main beam simulations have been performed using Physical Optics (PO) and Physical Theory of Diffraction (PTD) on both reflectors (for a detailed description of GRASP analysis method see Appendix B.2). Physical Optics is a simple method that gives an approximation to the surface currents valid for perfectly conducting scatterers which are large in terms of wavelengths and represents the most accurate method to predict a radiation pattern.

3.3 Effect of filter and window

As we said in the previous chapter, the Strip focal plane array of corrugated feedhorns will be placed inside a cryostat, whose aperture is made of ultra-high molecular weight polyethylene (UHMWPE). In front of each Q-band module and W-band horn there will be also IR filters made of the same material. Both the filters and the window are designed with a central homogeneous core and an anti-reflection coating made of a series

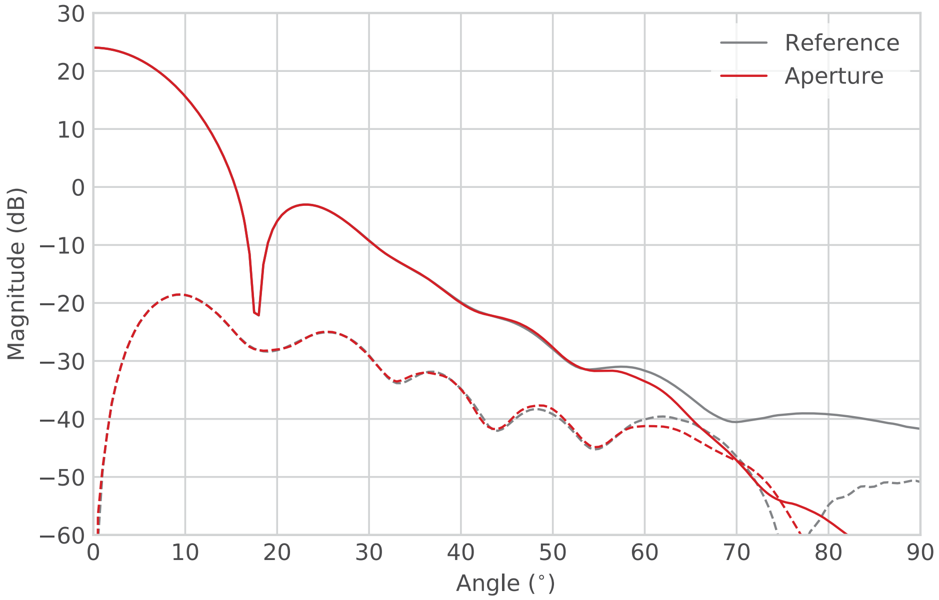

Figure 3.11: Comparison of the feedhorn nominal radiation pattern (grey) and the radiation pattern as it is modified by the introduction of a circular aperture in front of the horn (red). The plot shows the co-polar (solid) and cross-polar (dashed) component for $\phi = 45°$.

of pyramids on both sides of the core. The AR coating is supposed to reduce reflections that travel backwards through the system.

We expect these optical elements to modify the nominal feedhorn radiation pattern by introducing distortions. For this reason, we performed several simulation to understand how the nominal pattern is modified. We considered also different modelling approaches.

First of all, since the filters are supported by a metallic structure, we modelled the effect of a circular aperture on the radiation pattern using GRASP, which allows to define an aperture in an infinite conducting screen and computes the scattering by means of Babinet's principle (Pontoppidan 2008). Fig. 3.11 shows the effect of the introduction of a circular aperture on the feedhorn radiation pattern at 43 GHz. As we can see, the circular aperture changes the shape of the pattern at angles $> 60°$, which is approximately the angle between the feedhorn axis and the edge of the aperture.

Then, we simulated the effect of the introduction of the filter and the window without the AR coating using SRSR. We consider the central feedhorn, which lies on the telescope axis of symmetry, because SRSR provides a rigorous simulation of the electromagnetic performances of structures with symmetry of revolution; therefore, we cannot model feedhorns that are tilted with respect to the filter. All the simulations are performed at 43 GHz. Fig. 3.12 shows the pattern simulated by SRSR in two configurations: feedhorn with the filter and feedhorn with filter and window. These are compared with the nominal pattern.

The presence of the IR filter and the cryostat window changes significantly the beam shape. Since these simulations do not take into account the presence of the AR coating, we expect the presence of stationary waves between the optical elements. This effect is maximized by the fact that the central feedhorn leads to a normal incidence of the radiation onto the filter. The generation of stationary waves should be reduced by introducing a slight tilt between the feedhorn axis and the filter axis. This is the case for all the other

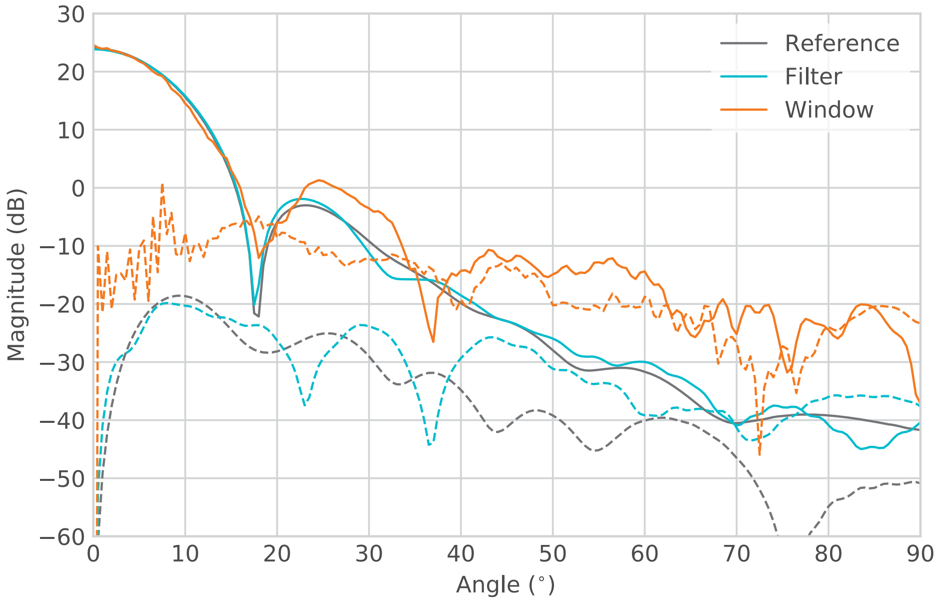

Figure 3.12: Feedhorn radiation pattern with filter (blue) and filter plus window (orange) as computed by SRSR. The co-polar (solid) and cross-polar (dashed) component for $\phi = 45°$ are shown.

feedhorns which are off-axis.

SRSR allows us to understand what happens without an AR coating as it takes into account the impedance mismatch between the different materials. It shows that the presence of the AR coating is crucial to avoid resonances. On the other hand, with GRASP we can simulate the case of a perfect impedance matching. This is done by modelling both the filter and window as lenses with flat surfaces. The lenses height corresponds to central homogeneous core without the pyramids. With this choice we are assuming that the pyramidal coating is acting as perfect AR coating with no reflections. The electromagnetic model of the lenses, as implemented in GRASP, is shown in Fig. 3.13. The scattering from each lens is calculated by means of a combination of Physical Optics and Geometrical Optics and a set of equivalent currents is calculated on each face of the lens. Simulations are performed considering the lens as mounted in an opaque screen. Only the equivalent currents on the lens face opposite to the source of the incident field are retained in the calculation of the radiated field and these currents radiate the total field in the forward half space, so that the incident field from the source should not be added.

We tried also to model both filter and window as dielectric layers for a cross-check; however, we found that the main difference between these two cases is that the surrounding metallic structure is not taken into account.

Finally, we simulated the radiation pattern considering both the filter and the cryostat window. The result is shown in Fig. 3.15 and it is compared with the pattern produced by the simple circular aperture. As we can see, the effect of the two lenses is to shrink the main beam, increasing the directivity, and to add ripples in the sidelobe region. This will affect the overall radiation pattern when the feedhorns are coupled with the telescope: we expect an increase in the full-width half-maximum (with respect to the model without the filters and window) and a lower level of the sidelobes.

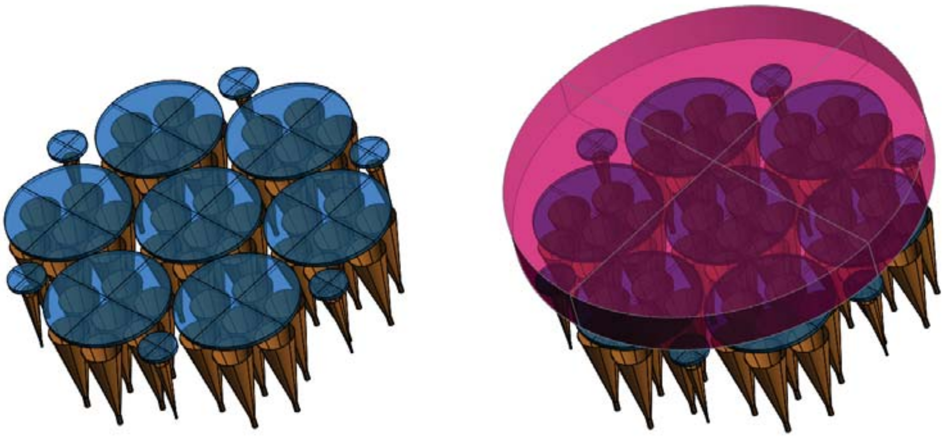

Figure 3.13: *Left*: GRASP model of the IR filters. *Right*: Model of the cryostat window. The IR filters can be seen underneath the window.

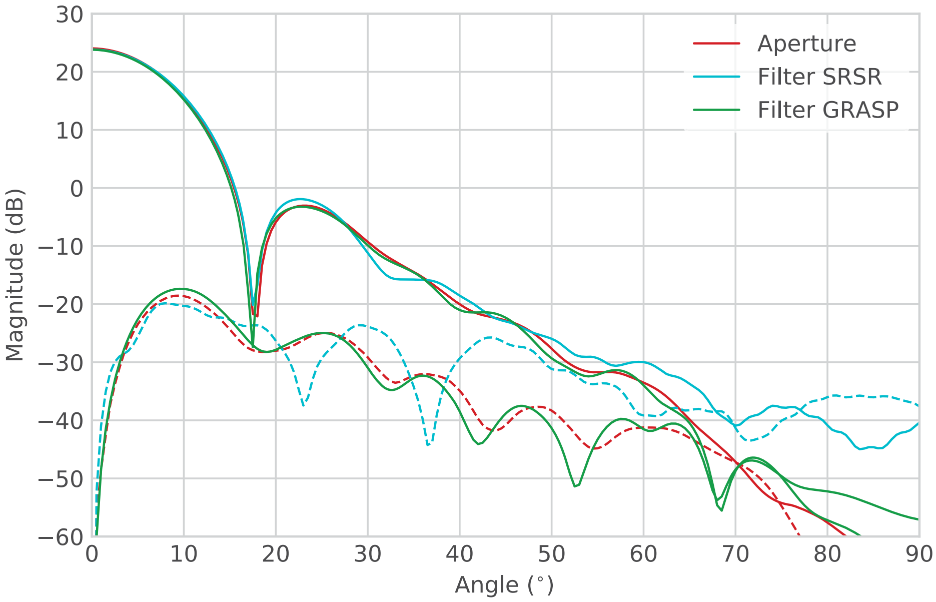

Figure 3.14: Feedhorn radiation pattern with filter modelled as a lens in GRASP (green). The pattern is compared with the pattern with only the circular aperture (red) and the pattern computed by SRSR (blue). The plot shows the co-polar (solid) and cross-polar (dashed) components for $\phi = 45°$.

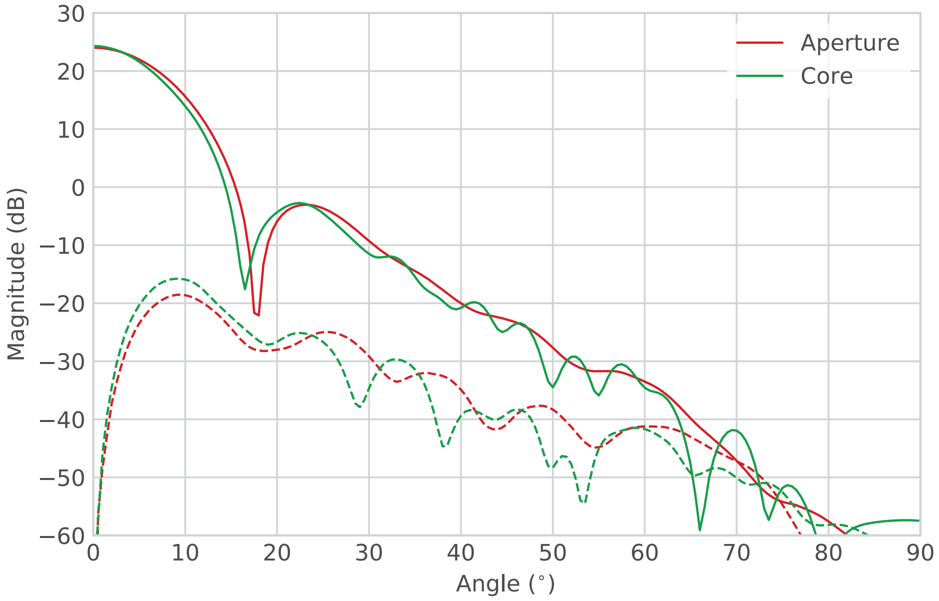

Figure 3.15: Feedhorn radiation pattern with filter and window modelled as lenses with thickness given by the central core thickness. The pattern is compared with the pattern with only the circular aperture (red line). The plot shows the co-polar (solid) and cross-polar (dashed) components for $\phi = 45°$.

3.4 Edge taper evaluation

The contour plots of the total amplitude field incident on the main reflector have been computed for each Strip Q-band feedhorn, in a surface grid with 301×301 points. The total amplitude field is defined as $\sqrt{E_x^2 + E_y^2 + E_z^2}$, where (x, y, z) is the coordinate system in which the field is calculated. The z-axis is pointing to the main beam direction. Physical Optics (PO) and Physical Theory of Diffraction (PTD) have been used to calculate the electric field incident on the surface of the primary and secondary mirror.

Fig. 3.16 and 3.17 show the field distribution on the primary and secondary mirror for all the 49 Q-band feedhorns divided in modules. As we can see, the feedhorns have been correctly placed so that the illumination is centered on the primary mirror. However, the illumination is roughly elliptical; hence, the field amplitude on the primary mirror rim is not constant. Fig. 3.18 and 3.19 show the edge taper curves for the feedhorns I_0, R_0, O_0 and Y_0. The angle ϕ moves along the rim of the mirror counterclockwise.

3.5 Main beams results

Far-field radiation patterns have been computed in the co- and cross-polarization basis according to Ludwig's third definition (Ludwig 1973) in uv-spherical grids to retrieve the main beam angular resolution of each feedhorn model analysed, as well as all major electromagnetic characteristics described in Appendix A.

A uv-grid defines field points in a 2D grid on a sphere where the field shall be calculated. The 2D grid is defined by the (u, v) coordinates, where u and v are dimensionless

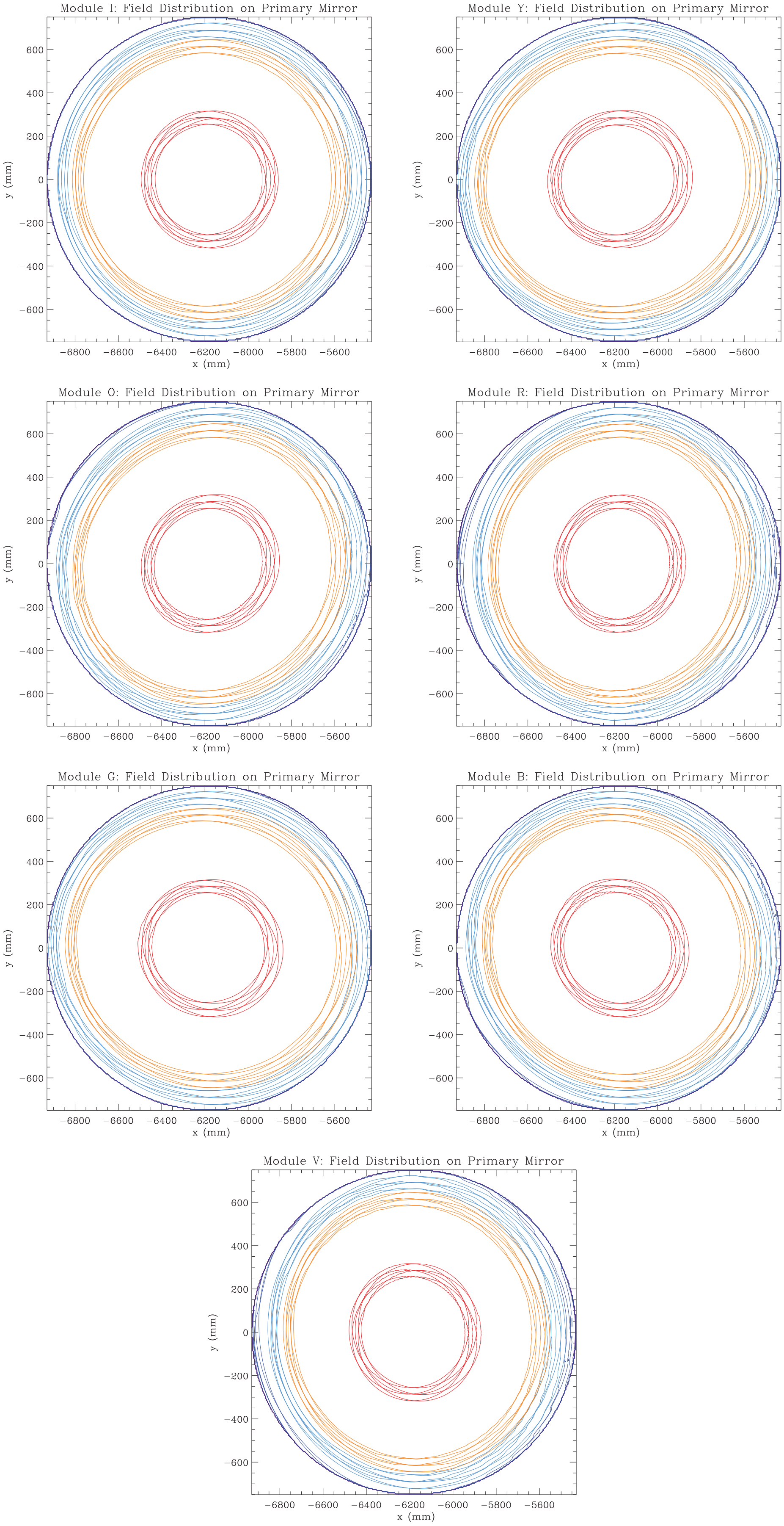
Module I: Field Distribution on Primary Mirror

Module Y: Field Distribution on Primary Mirror

Module O: Field Distribution on Primary Mirror

Module R: Field Distribution on Primary Mirror

Module G: Field Distribution on Primary Mirror

Module B: Field Distribution on Primary Mirror

Module V: Field Distribution on Primary Mirror

Figure 3.16: Field distribution on the primary mirror, for each module. Contour levels at -3, -15, and -20 dB are plotted.

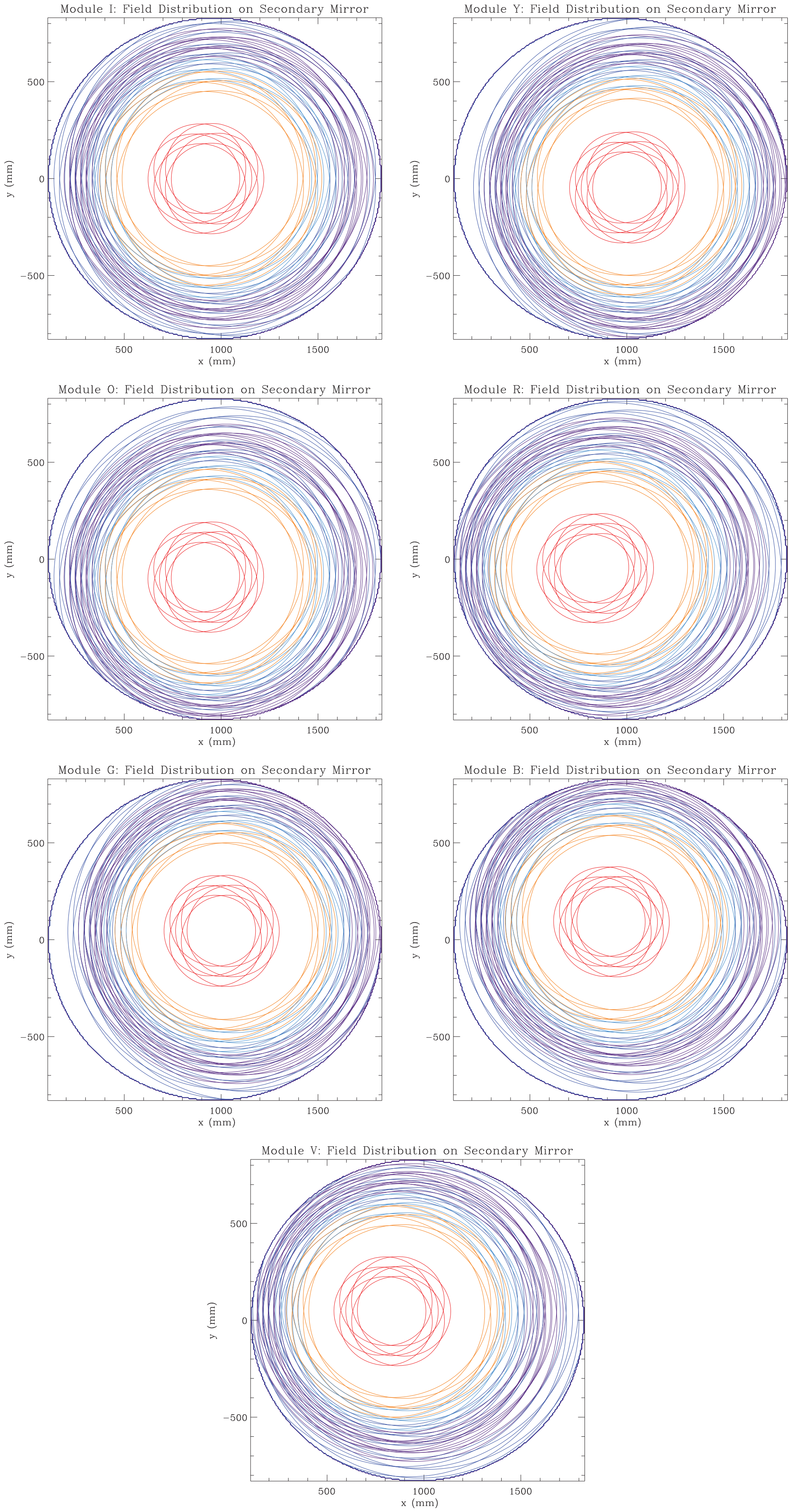

Figure 3.17: Field distribution on the secondary mirror, for each module. Contour levels at -3, -15, and -20 dB are plotted.

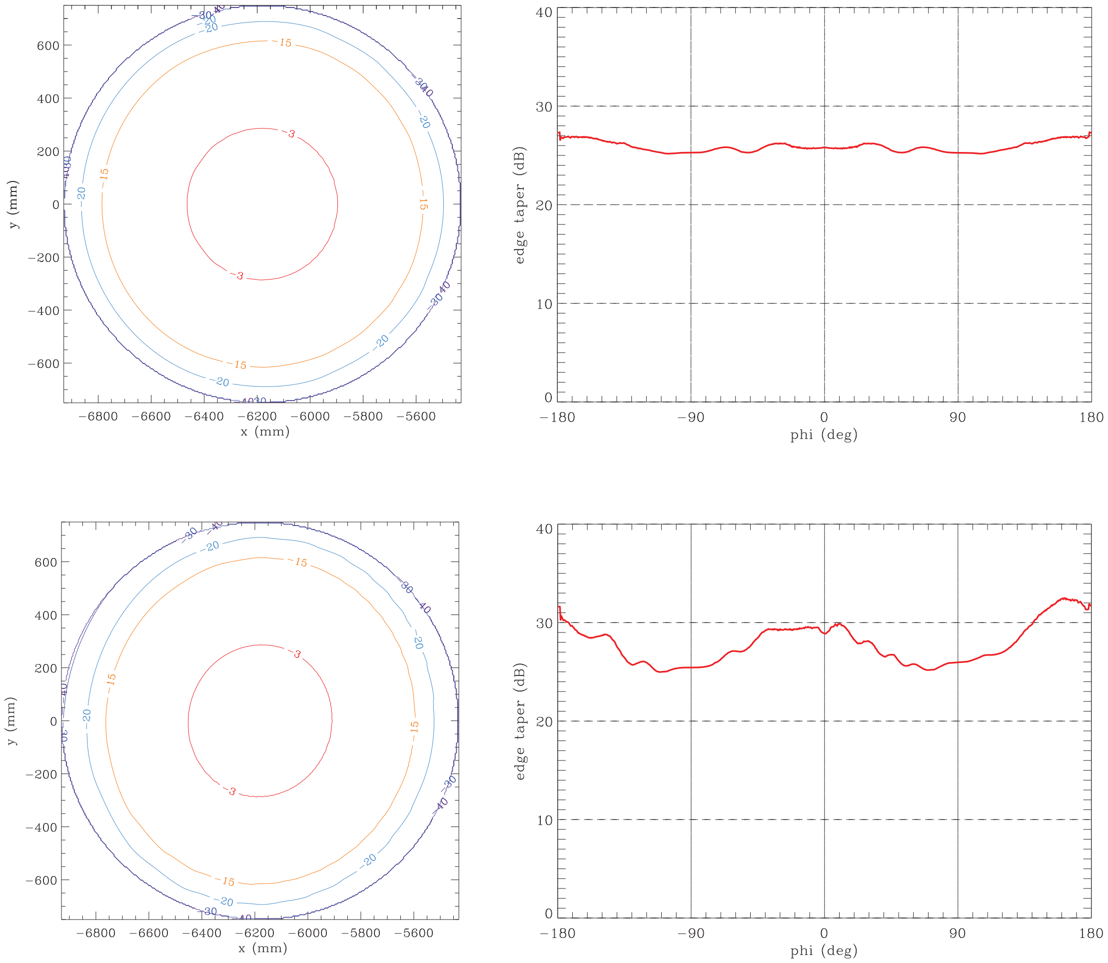

Figure 3.18: Field distribution on the main reflector and edge taper curves for the feedhorn I_0 (*top panel*) and the feedhorn R_0 (*bottom panel*) at 43 GHz.

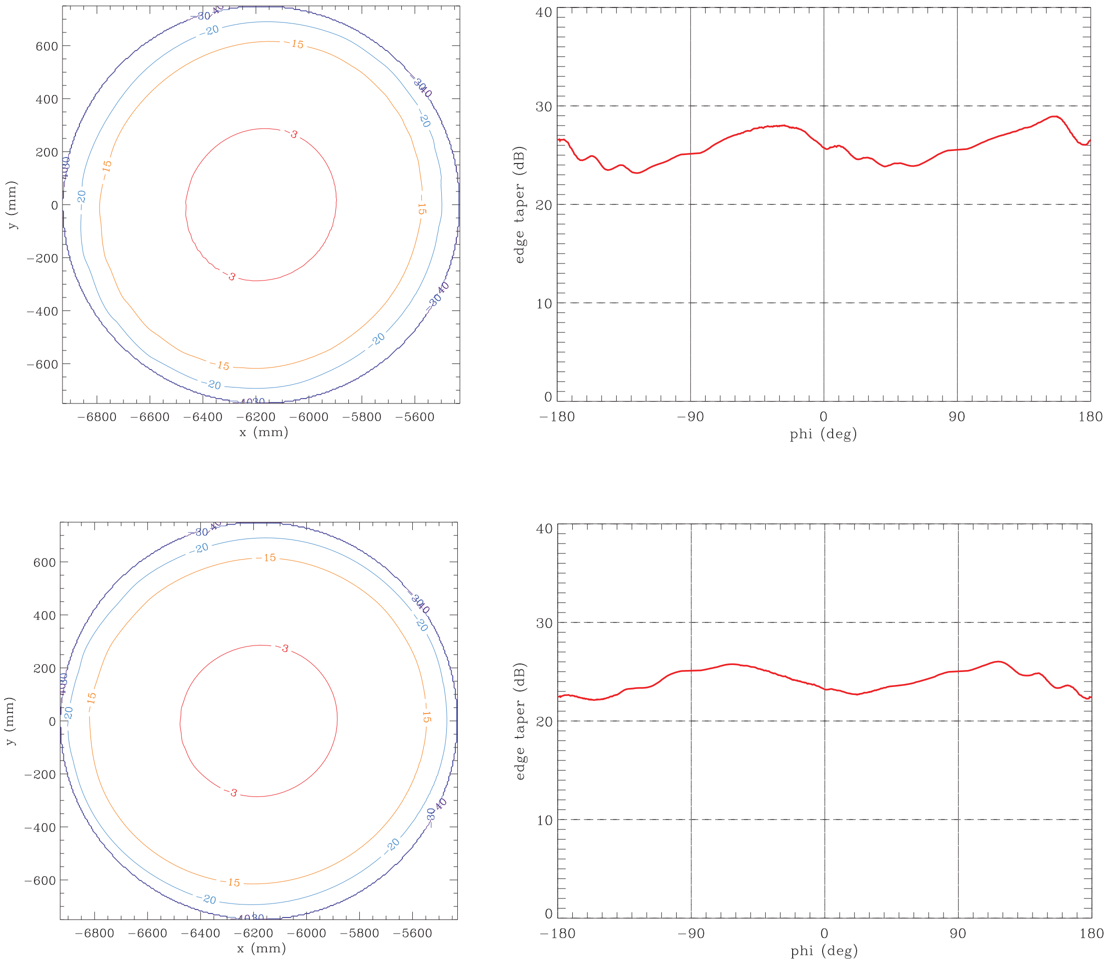

Figure 3.19: Field distribution on the main reflector and edge taper curves for the feedhorn O_0 (*top panel*) and the feedhorn Y_0 (*bottom panel*) at 43 GHz.

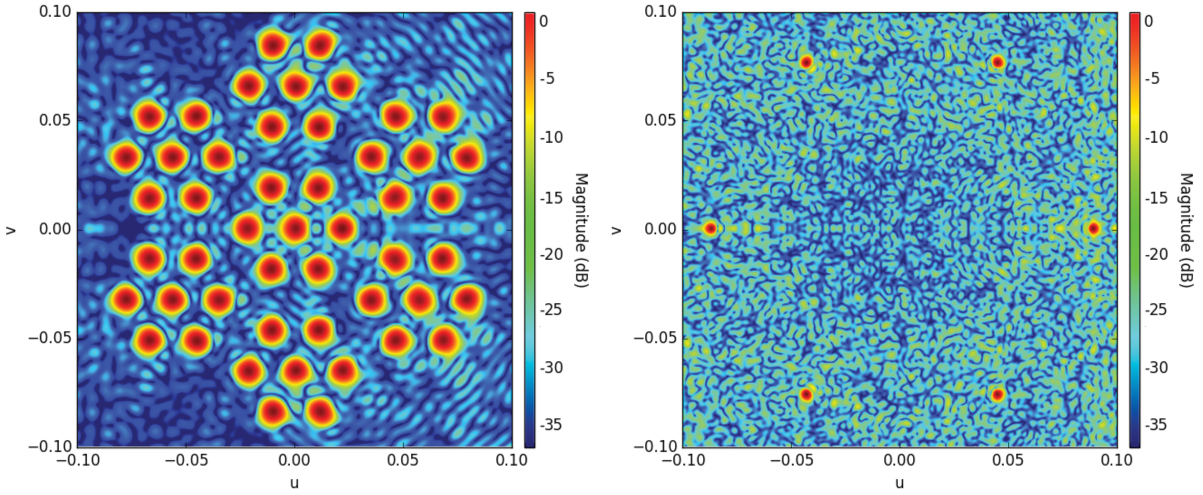

Figure 3.20: *Left*: Footprint of the forty-nine Q-band beams in the sky in (u, v) coordinates. *Right*: Footprint of the six W-band beams in the sky. The telescope symmetry plane is along the v-axis.

and can be related to the spherical coordinates by

$$\begin{aligned} u &= \sin\theta\cos\phi, \\ v &= \sin\theta\sin\phi. \end{aligned} \tag{3.1}$$

The feedhorns are excited individually with a linearly polarized signal along their x-axis at the simulation frequency, so that the forty-nine Q-band and six W-band radiation patterns can be calculated. The footprint of the 49 Q-band beams and 6 W-band beams in the sky is shown in Fig. 3.20. The overall width of the footprint is $\sim 10°$.

With the exception of the I_0 feedhorn, which is placed in the focus of the telescope, all the feedhorns are off-axis, so that the resulting main beams do not point along the telescope reference boresight. In Tables 3.4 and 3.5 we report the coordinate systems, with respect to the telescope reference boresight, in which each main beam has been computed. The angles θ_{MB} and ϕ_{MB} define the beam location in the sky, while ψ_{MB} is the polarization angle[3].

The main beams for all the forty-nine Q-band feedhorns have been simulated within the range $-0.02 < (u, v) < 0.02$, corresponding to a range between $\pm 1.15°$ in θ and ϕ polar coordinates. Each grid is sampled with 601×601 points, which means a spatial resolution of about 14 arcsec. From Fig. 3.21 to Fig. 3.24, we report the contour plot of the main beam relevant to co– and cross– polar components at the center frequency 43 GHz for the feedhorns I_0, O_0, R_0 and Y_0.

The main beams for all the six W-band feedhorns have been simulated within the range $-0.015 < (u, v) < 0.015$, corresponding to a range between $\pm 0.86°$ in θ and ϕ polar coordinates. Each grid is sampled with 301×301 points, i.e. a spatial resolution of about 20.5 arcsec. From Fig. 3.25 to Fig. 3.26, we report the contour plot of the main beam relevant to co– and cross– polar components at the center frequency 95 GHz for the feedhorns W_1 and W_2.

---

[3] Even if the simulated beams are computed as the far-field angular transmission function of a polarized radiating element, in general the far-field pattern is no longer linearly polarized. The beam frame definition adopted to compute each main beam involves that the power peak of the co-polar component lies in the center of the uv-grid and that a minimum in the cross-polar component appears in the same point (i.e. the major axis of the polarization ellipse is along the u-axis).

	Module I						
	I0	I1	I2	I3	I4	I5	I6
θ_{MB} (°)	0.0000	1.2395	1.2430	1.2449	1.2430	1.2396	1.2380
ϕ_{MB} (°)	0.0000	60.1344	120.1452	-180.0000	-120.1452	-60.1371	0.0000
ψ_{MB} (°)	0.0000	0.1216	0.1314	0.0000	-0.1314	-0.1216	0.0000
	Module B						
	BO	B1	B2	B3	B4	B5	B6
θ_{MB} (°)	3.7549	2.7455	2.7557	3.9676	4.8790	4.8631	3.9428
ϕ_{MB} (°)	-90.4574	-77.3238	-103.3999	-108.7389	-98.0166	-83.2403	-72.1571
ψ_{MB} (°)	-0.3414	-0.2179	-0.2103	-0.3383	-0.4673	-0.4616	-0.3424
	Module Y						
	Y0	Y1	Y2	Y3	Y4	Y5	Y6
θ_{MB} (°)	3.7288	4.8336	3.9309	2.7420	2.7297	3.9166	4.8233
ϕ_{MB} (°)	30.2222	37.5857	48.7282	43.3710	17.1640	11.7829	22.8262
ψ_{MB} (°)	-0.1141	-0.0143	-0.0080	-0.1124	-0.2114	-0.2068	-0.1111
	Module O						
	O0	O1	O2	O3	O4	O5	O6
θ_{MB} (°)	3.7549	4.8631	4.8790	3.9676	2.7557	2.7455	3.9428
ϕ_{MB} (°)	90.4574	83.2403	98.0166	108.7389	103.3999	77.3238	72.1571
ψ_{MB} (°)	0.3414	0.4616	0.4673	0.3382	0.2103	0.2179	0.3424
	Module V						
	V0	V1	V2	V3	V4	V5	V6
θ_{MB} (°)	3.7802	2.7611	3.9822	4.9158	4.9215	3.9808	2.7645
ϕ_{MB} (°)	-150.2355	-163.0545	-168.4055	-157.6140	-143.1977	-132.1095	-137.1113
ψ_{MB} (°)	-0.4915	-0.3352	-0.3294	-0.4910	-0.6447	-0.6388	-0.4901
	Module R						
	R0	R1	R2	R3	R4	R5	R6
θ_{MB} (°)	3.7802	3.9808	4.9215	4.9158	3.9822	2.7611	2.7645
ϕ_{MB} (°)	150.2355	132.1095	143.1977	157.6140	168.4055	163.0545	137.1113
ψ_{MB} (°)	0.4915	0.6388	0.6447	0.4910	0.3294	0.3352	0.4900
	Module G						
	G0	G1	G2	G3	G4	G5	G6
θ_{MB} (°)	3.7288	3.9166	2.7297	2.7420	3.9309	4.8336	4.8233
ϕ_{MB} (°)	-30.2222	-11.7829	-17.1640	-43.3710	-48.7282	-37.5857	-22.8262
ψ_{MB} (°)	0.1141	0.2068	0.2114	0.1124	0.0080	0.0143	0.1111

Table 3.4: Angles defining the coordinate systems, with respect to the telescope boresight, in which each Q-band main beam has been computed.

	W1	W2	W3	W4	W5	W6
θ_{MB} (°)	4.9900	5.0128	5.0629	5.0907	5.0613	5.0128
ϕ_{MB} (°)	0.0000	60.5208	120.5072	-180.0000	-120.2182	-60.5208
ψ_{MB} (°)	-179.5800	240.5190	120.5280	-179.7917	-120.5344	119.4773

Table 3.5: Angles defining the coordinate systems, with respect to the telescope boresight, in which each W-band main beam has been computed.

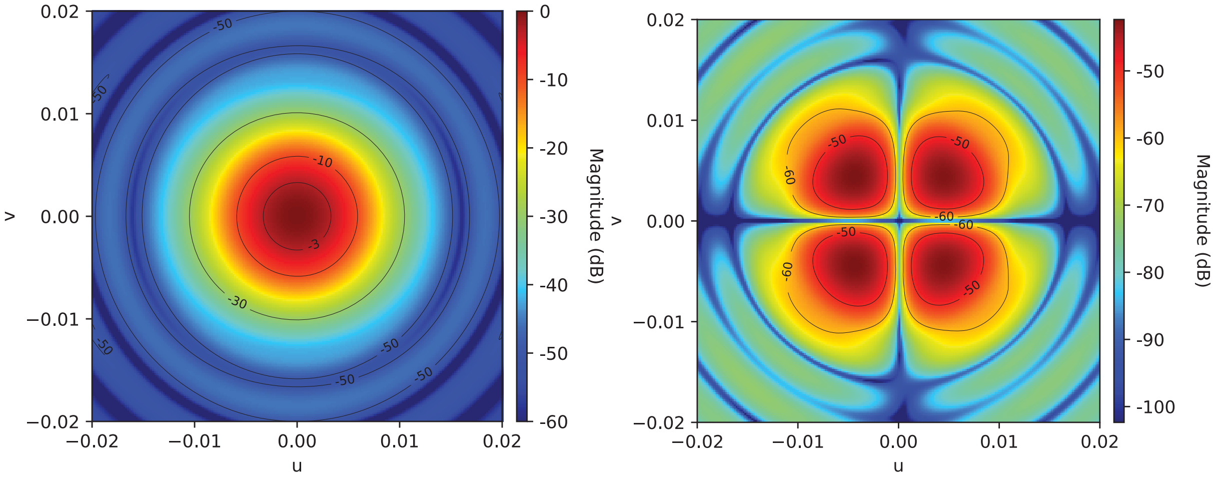

Figure 3.21: Co–polar (*left*) and cross–polar (*right*) peak-normalized components of the I_0 radiation pattern at 43 GHz in the uv plane.

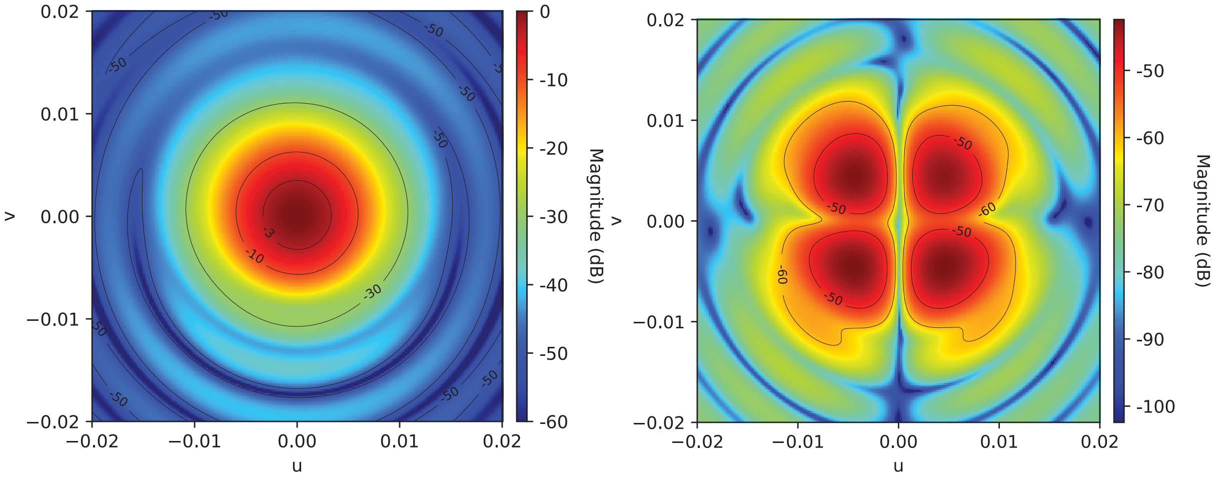

Figure 3.22: Co–polar (*left*) and cross–polar (*right*) peak-normalized components of the O_0 radiation pattern at 43 GHz in the uv plane.

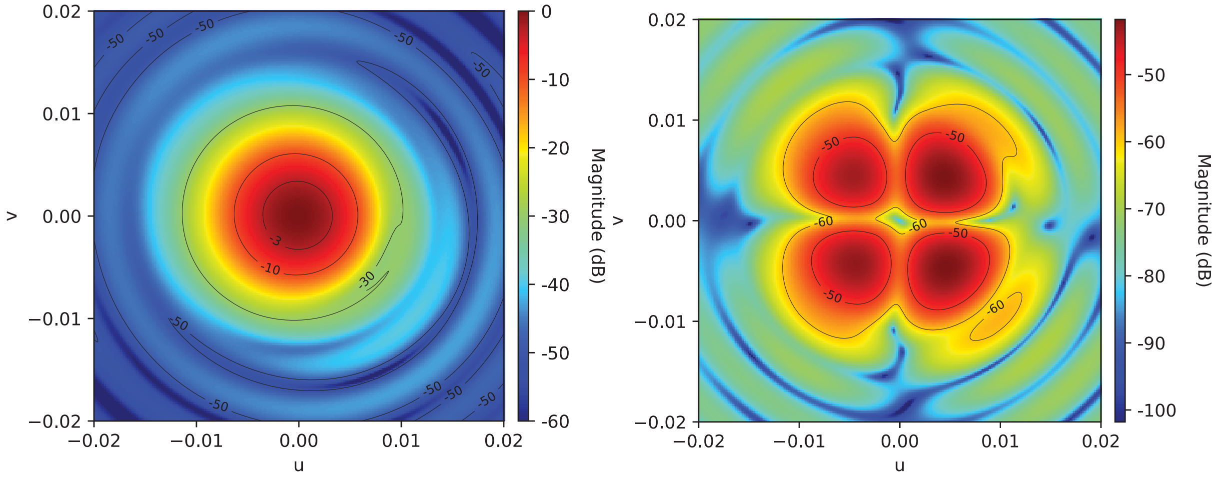

Figure 3.23: Co–polar (*left*) and cross–polar (*right*) peak-normalized components of the I_0 radiation pattern at 43 GHz in the uv plane.

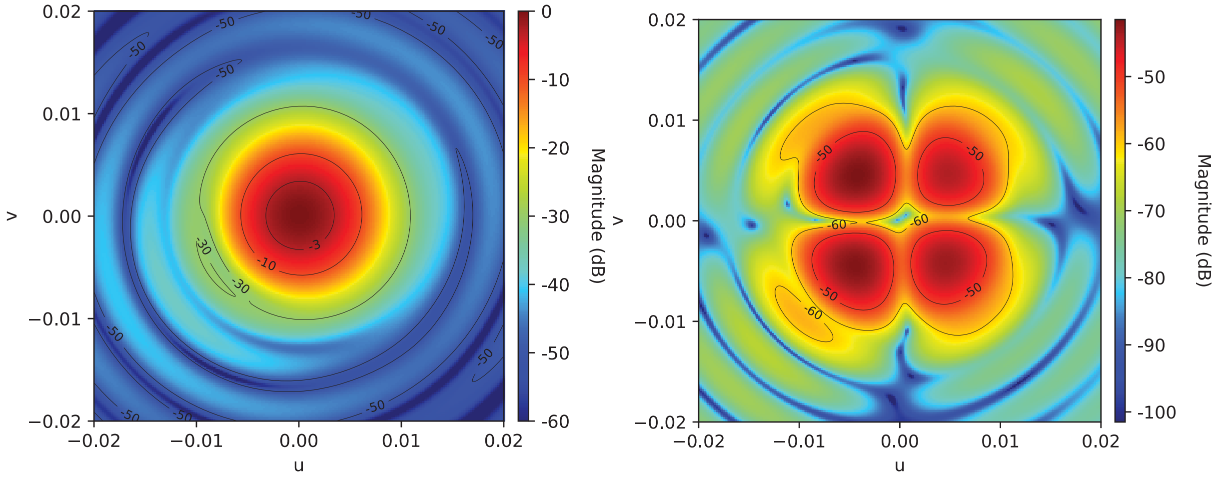

Figure 3.24: Co–polar (*left*) and cross–polar (*right*) peak-normalized components of the Y_0 radiation pattern at 43 GHz in the uv plane.

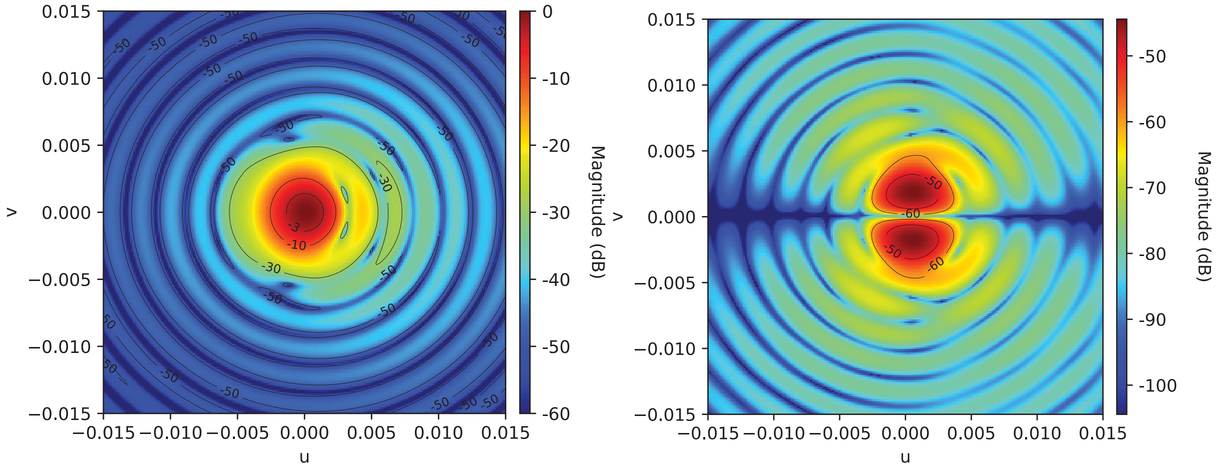

Figure 3.25: Co–polar (*left*) and cross–polar (*right*) peak-normalized components of the W_1 radiation pattern at 95 GHz in the uv plane.

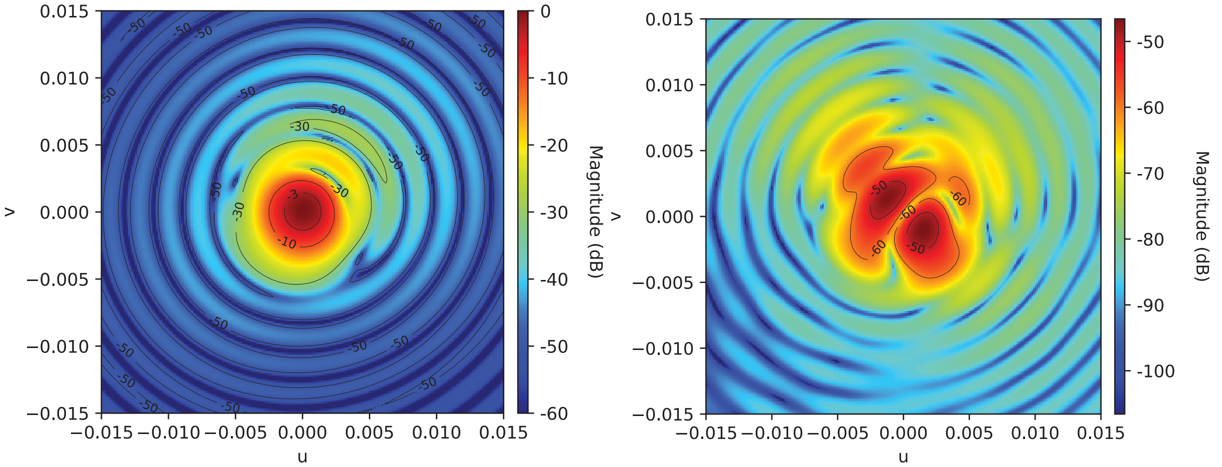

Figure 3.26: Co–polar (*left*) and cross–polar (*right*) peak-normalized components of the W_2 radiation pattern at 95 GHz in the uv plane.

Given the telescope configuration and the feedhorn off-axis location on the focal surface, the main beams are distorted and their shape differs from the Gaussian one. For this reason, the main beams cannot be mathematically represented by a single parameter (e.g. the Full-Width Half-Maximum of a Gaussian curve). For a complete characterization of the main beams, we evaluated several descriptive parameters: the angular resolution (FWHM), the ellipticity (e), the main beam directivity (D), the cross-polarization discrimination factor (XPD). These parameters are detailed in Appendix A.

For CMB anisotropy measurements, we can define an effective angular resolution as the FWHM of a perfect (symmetric gaussian) beam which produces the same signal of the distorted beam when the CMB field is observed. This quantity might be needed in the data analysis. Nevertheless, this definition requires astrophysical simulations done taking into account the scanning strategy and the CMB expected anisotropy map; hence, it is not viable in the analysis of the beam properties due to the excessive computational time required. Instead of the effective FWHM, we computed the average angular resolution of the beam (FWHM_A), which is related to ellipticity.

Tables 3.6 and 3.7 summarizes the major characteristics of the main beams of each feedhorn in half the focal plane due to the telescope symmetry. The beams relevant to the off-axis receivers are more subject to beam distortions; however, all beams are compliant with the requirements on the optics polarization purity, showing XPD $>$ 30 dB.

Main beam characterization in the frequency band

Because of the different response of feedhorns with the frequency and the different telescope diameter with respect to the wavelength, the main beam shape is expected to be frequency dependent within the bandwidth of each detector. Fig. 3.27 shows the copolar patterns ($\phi = 0°$) of the Q-band feedhorns as frequency varies in the bandwidth from 38 to 47 GHz. Radiation patterns have been simulated in the required frequency band, with a 0.5 GHz discretization.

Sub-reflector illumination is strongly dependent on the feeding frequency; in fact, in the azimuthal region between $15°$ and $30°$, power varies about 20 dB with frequency and the sidelobe peak and null gradually shift at lower angles with increasing frequency.

A direct consequence of the edge taper variation with the frequency is a different illumination of the telescope: increasing the frequency the primary mirror is less illumi-

Beam	FWHM$_x$ ($'$)	FWHM$_y$ ($'$)	FWHM$_A$ ($'$)	e	$\mathcal{D}$ (dBi)	XPD (dB)
I0	22.34	22.22	22.28	1.01	57.61	42.35
I1	22.34	22.30	22.32	1.00	57.59	42.08
I2	22.45	22.26	22.35	1.01	57.58	42.47
I3	22.51	22.23	22.37	1.01	57.57	42.30
I4	22.45	22.26	22.35	1.01	57.58	42.47
I5	22.34	22.30	22.32	1.00	57.59	42.08
I6	22.35	22.25	22.30	1.00	57.60	42.05
Y0	22.44	22.52	22.48	1.00	57.48	41.50
Y1	22.60	22.75	22.67	1.01	57.38	41.25
Y2	22.49	22.59	22.54	1.00	57.46	41.75
Y3	22.45	22.35	22.40	1.00	57.53	41.85
Y4	22.45	22.32	22.39	1.01	57.53	41.94
Y5	22.52	22.52	22.52	1.00	57.46	41.46
Y6	22.63	22.72	22.67	1.00	57.38	41.32
O0	22.46	22.78	22.62	1.01	57.41	42.42
O1	22.61	22.99	22.80	1.02	57.32	42.32
O2	22.60	23.04	22.82	1.02	57.31	42.49
O3	22.87	22.51	22.69	1.02	57.38	42.22
O4	22.62	22.41	22.51	1.01	57.47	42.26
O5	22.36	22.59	22.48	1.01	57.48	42.15
O6	22.50	22.75	22.62	1.01	57.41	42.27
R0	22.97	22.41	22.69	1.03	57.40	41.78
R1	22.96	22.46	22.71	1.02	57.39	42.11
R2	23.21	22.60	22.91	1.03	57.29	41.60
R3	23.24	22.61	22.93	1.03	57.29	41.48
R4	23.02	22.48	22.75	1.02	57.37	41.50
R5	22.80	22.31	22.56	1.02	57.47	42.09
R6	22.78	22.29	22.53	1.02	57.48	42.17

Table 3.6: Main beam characteristics at the central frequency 43 GHz.

Beam	FWHM$_x$ ($'$)	FWHM$_y$ ($'$)	FWHM$_A$ ($'$)	e	$\mathcal{D}$ (dBi)	XPD (dB)
W1	9.30	9.52	9.41	1.0231	61.45	44.43
W2	9.25	9.42	9.34	1.0185	61.52	46.57
W3	9.29	9.34	9.32	1.0054	61.56	46.53
W4	9.49	9.48	9.49	1.0004	61.40	44.14

Table 3.7: Main beam characteristics at the central frequency 95 GHz.

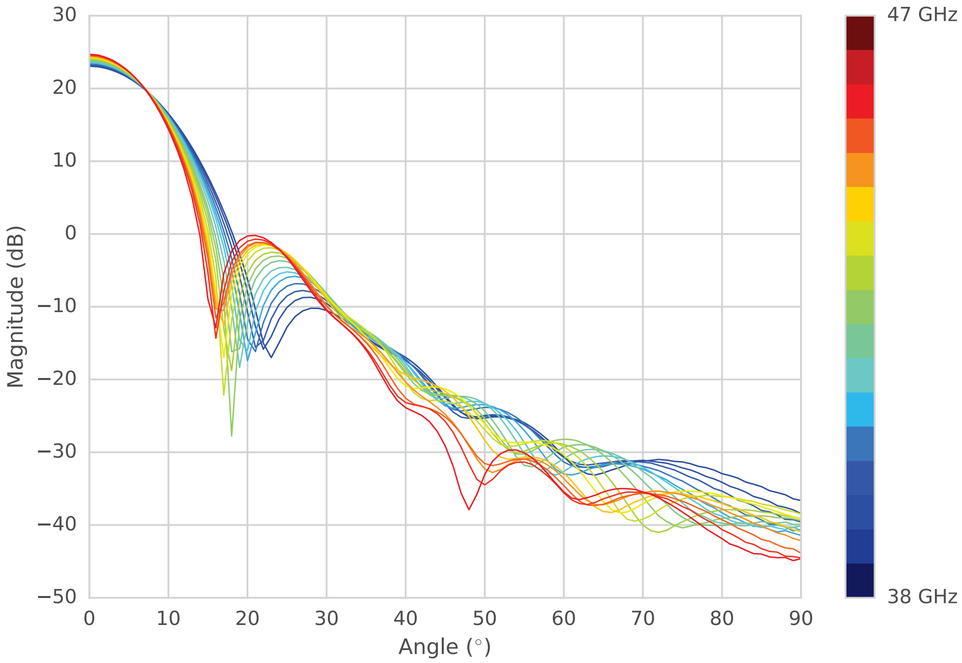

Figure 3.27: Co-polar radiation patterns frequency dependence in the Q-band. Patterns are simulated in the feedhorn coordinate system.

nated and the angular resolution would in principle get worst. However, this effect is compensated by the fact that the mirror at higher frequency is larger (in terms of wavelength) compared to the lower frequency. As a result, the bandwidth effect on the main beams is not predictable analytically, but only through simulations that are still underway. Hereafter we report only the result for the analysis of the FWHM variation in the bandwidth for the feedhorn I_0. As we can see from Fig. 3.28, the maximum variation of the full-width half-maximum at –3 dB from 39 to 47 GHz is about 1.8%. The significance of this variation may be verified by assessing the impact on CMB observations. However, it will be crucial to account for this information during the data analysis process, since the variation of the beam shape in the bandwidth should be weighted by the radiometers response in the bandwidth.

Rotation angle of the polarization ellipse

As we said, each main beam has been computed in its own coordinate system in uv spherical grids. Although the simulated beams are computed as the far-field angular transmission function of a largely polarized radiating element (i.e. the feedhorn) in the focal plane of the telescope, in general the far-field pattern is no longer linearly polarized: a small circular component is present as induced by the optics (Sandri 2005).

The beam frame definition adopted, in which each main beam has been computed, involves that i) the power peak of the co– polar component lies in the center of the uv-grid and ii) a minimum in the cross– polar component appears in the same point (i.e. the major axis of the polarization ellipse is along the u-axis). This means that, very close to the beam pointing direction, the main beam can be assumed linearly polarized.

Fig. 3.29 shows the rotation angles of the polarization ellipse the I_0, O_0, Y_0 and R_0 beams. As we can see, they are largely linearly polarized close to the pointing direction.

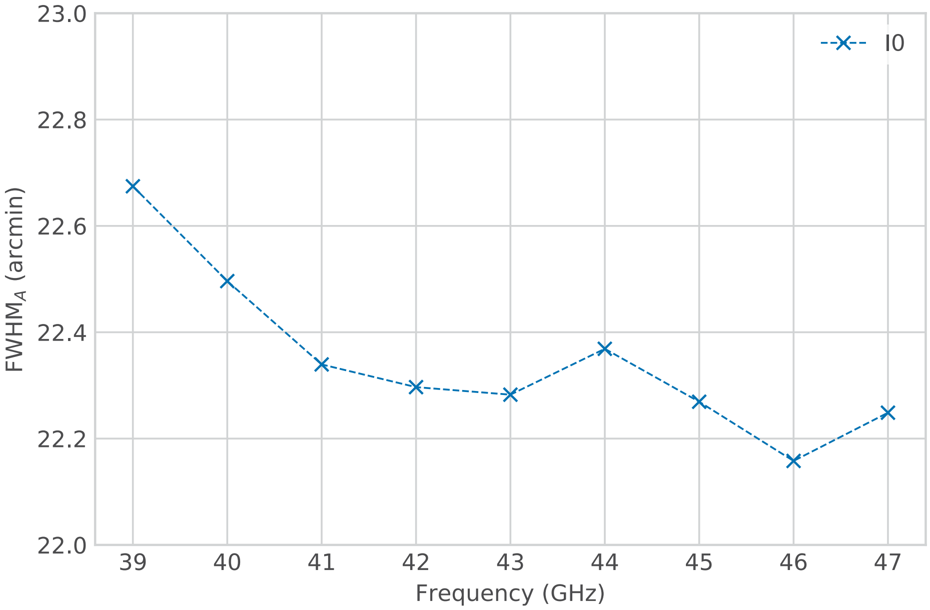

Figure 3.28: FWHM at –3 dB from the main beam power peak for the I_0 beam in the frequency range 37-49 GHz.

3.6 Mirrors imperfection modelling

Telescope structural analysis is currently being developed to verify Strip telescope design compliance with safety, legal and scientific requirements.

The theoretical shape of the reflectors can be approached only up to some finite limit tolerance set by fabrication constrains. Moreover, deformations can occur during telescope operation due to the effect of gravity, temperature variations and wind pressure.

Irregularities on the reflector surfaces induce phase variations across the antenna aperture and the resulting performance of the optical system could be considerably degraded. In this section an evaluation of the impact of such distortions on the main beam is reported.

In particular, we evaluated the effect of mechanical tolerance as a random error on the surface, whereas we analysed the effect of a structured variation due to external effects describing the surface by means of Zernike polynomials. The analysis of the structural behavior has been performed by the company BCV progetti s.r.l., who provided the Zernike polynomials expansion used for the subsequent optical analysis.

Random surface

The surface of the mirrors can be defined in a regular grid with random z-values, specified by a correlation distance and an amplitude. With this approach, we can model slowly varying errors, which are typical for thermal distortions, as well as rapidly varying errors, which are more typical for manufacturing tolerances. The surface values at the nodes of the regular grid are selected as random numbers uniformly distributed in a given interval (the peak-to-peak value) and with a mean value equal to zero. A cubic interpolation function yields a smooth surface between the random values at the nodes. The spacing between the nodes, c_x and c_y, relative to the reflector diameter determines the roughness of the surface and the rms-value of the distortions can be computed as

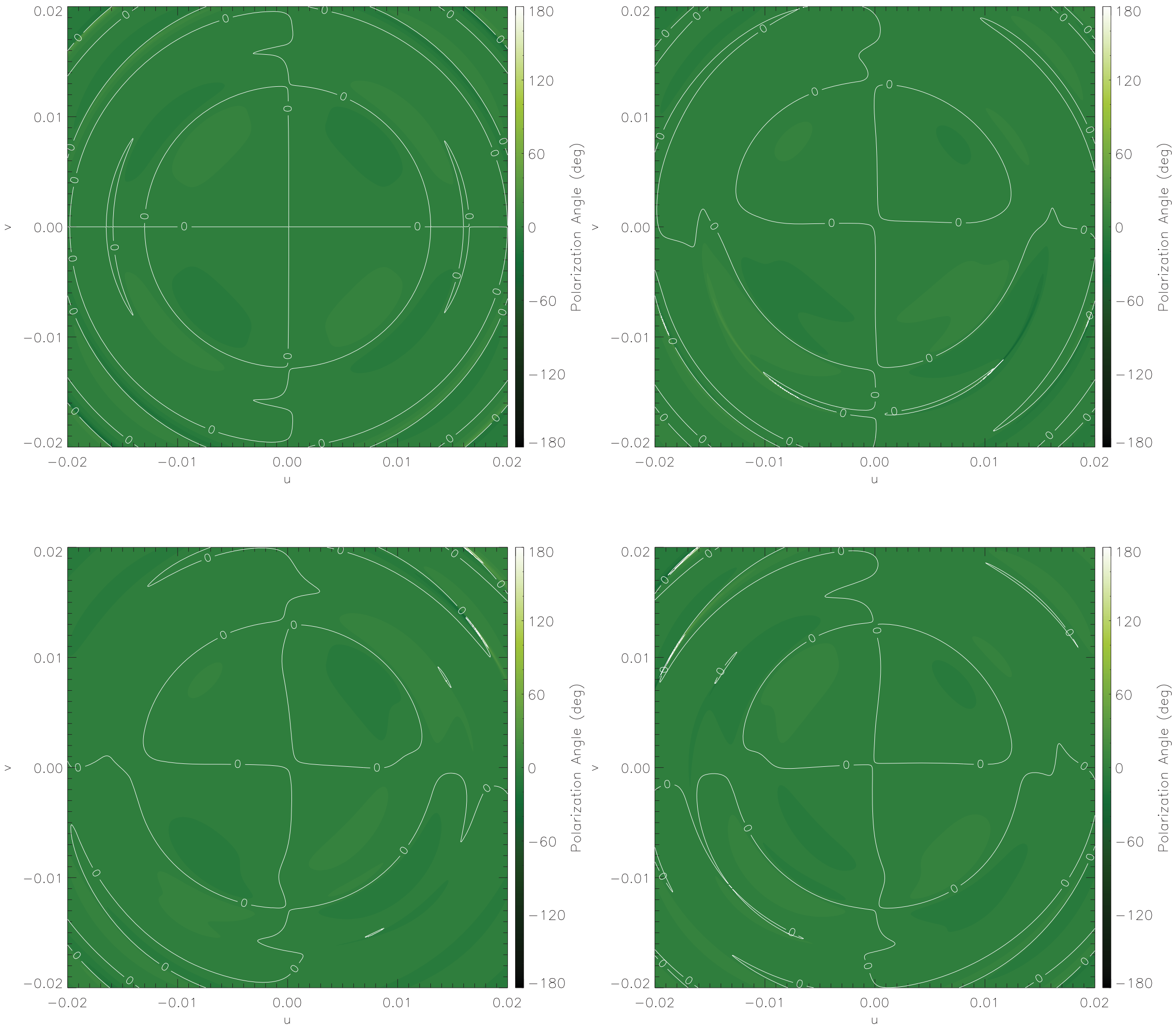

Figure 3.29: Polarization angle of the I_0 (top-left), O_0 (top-right), R_0 (bottom-left) and Y_0 (bottom-right) main beams at 43 GHz. Main beams are largely linearly polarized close to the pointing direction.

Feed	c_x (mm)	ΔFWHM$_\mathrm{A}$ (%)	Δe (%)	$\Delta\mathcal{D}$ (%)	ΔXPD (%)
I$_0$	7.46	0.02	-0.02	0.09	0.02
	100	-0.16	-0.21	0.10	0.64
	500	0.31	0.04	-0.07	0.17
R$_0$	7.46	0.02	-0.03	0.09	0.10
	100	0.03	0.30	0.05	-0.43
	500	0.34	-0.38	-0.07	0.45

Table 3.8: Differences between main beam descriptive parameters computed with ideal reflectors and those computed with random distortions on three different scales. $\Delta\mathcal{D}$ and ΔXPD are computed in dB scale.

$0.24\cdot$ PP, where PP is the peak-to-peak value.

The STRIP mirrors are designed to have a peak-to-peak error within $\pm 50\,\mu$m; therefore, we consider an rms value of 23.5 μm. Since the error has been measured with a photogrammetry along the z-axis used to define the mirror surface shape, the results will be slightly underestimated due to the incidence angle on the mirror. We considered three different scales for the random distortions analysis: the scale of the central wavelength (7.46 mm), a variation on the scale of the whole telescope and an intermediate scale of ~ 20 cm, which should take into account variations due to the mirrors supporting structure. The percentage variation of main beam descriptive parameters computed with ideal reflectors and with random distortions for the representative horns I$_0$ and R$_0$ is reported in Table 3.8 and it shows that the variations are lower than 0.5%.

Zernike surface

The GRASP simulation software allows to define a surface through a weighted sum of Zernike polynomials, where the evaluation of the Zernike expansion determines the z-values of the surface.

Zernike polynomial expansion is an efficient way to describe a moderately shaped reflector surface and it is frequently used in optics for the investigation of aberrations (see e.g. Born & Wolf (1999)). Even if Zernike polynomials are in general complex-valued functions, since we are interested only in the real part, each mode may be written as

$$Z_n^m(x,y) = a_n^m R_n^m(\rho)\cos(m(\phi-\phi_n^m)), \tag{3.2}$$

where a_n^m is the amplitude, ϕ_n^m is a reference direction, ρ and ϕ are the polar coordinates. The polynomials R_n^m are listed in Appendix C and the functions are normalized such that $R_n^m(1) = 1$. The formulation in Eq. (3.2) is only useful for surface approximations within the unit circle $0 \leq \rho \leq 1$ in the xy-plane. Therefore, a transformation from the unit circle to the elliptical reflector area in the xy-plane is necessary. The surface may then be expressed by

$$Z(x,y) = w\sum_{m,n} a_n^m R_n^m(\rho)\cos(m(\phi-\phi_n^m)), \tag{3.3}$$

where w is a weight factor, a_n^m is the amplitude of the Zernike mode (m,n), $R_n^m(\rho)$ is the radial Zernike polynomial, and ϕ_n^m is the reference direction.

With this description of deformations, we can analyse with GRASP the effect of the structural behavior of the main and sub-reflector of the Strip telescope for different design loads and configurations. The structural analysis of the reflectors has been made considering the mirrors as supported on a rigid structure; hence, it takes into account only the reflector stiffness. The analysis does not consider the optical enclosure, telescope mount and baseplate influence, which will be studied in the next future. The elevation range of the telescope, and accordingly mirrors orientation, is between 35° and 90° given as elevation angles (i.e. between 55° and 0° zenith angles)[4].

Different loads act or may act on mirrors during telescope operative conditions: gravity, rotation and movements effects, thermal loads (temperature variation and gradient) and wind pressure. Hereafter we give more details about each load that will be considered in the optical analysis.

- **Gravity.** Gravity load cases have been studied changing the reflectors orientation and taking into account the rotation angle about elevation axes. Six elevation angles have been studied: 90°, 80°, 70°, 60°, 50° and 35° (zenith angles).
- **Thermal load.** Uniform, non-uniform temperature variations and thermal gradient produce deformations in the telescope reflectors. At the moment, there is not enough information about realistic temperature distributions on telescope components during observation time. For this reason, the following cases have been studied: uniform temperature variation of $+20^\circ$C, unitary axial gradient and unitary lateral gradient along axes. These load cases are useful to understand the impact of different thermal conditions.
- **Wind.** Strip telescope will be mounted within a building with a removable protecting roof and it will have two wind speed thresholds for operation. Observations can be performed if wind speed is lower than 12.5 m/s. For higher speed the telescope will move to a “survival” configuration up to wind speed of 24.0 m/s. Over this second limit, the dome will be closed. For safety reasons, wind effects have been analyzed supposing front wind directed orthogonal to optical surface with two speeds, 12.5 m/s and 24.0 m/s.

Table 3.9 summarizes the different load conditions considered for the effect on the optical performance with their identification code. For all the configurations, the deformations of the optical surface were computed and represented using the Zernike polynomial approach. An example of deformation due to gravity effect is shown in Fig. 3.30, while the effect of a thermal load is shown in Fig. 3.31.

The percentage variation of main beams computed with ideal reflectors and with distortions retrieved by the structural analysis is reported in Tables 3.10 and 3.11 for feedhorn I_0 and R_0, respectively. The results show that FWHM variations are lower than 0.05% . The same holds true for ellipticity, with the exception of load W2, which shows a greater distortion with respect to all other loads. For both the feedhorn we analysed, the W2 configuration gives a higher value, so we will have to analyze in detail the effect of strong winds. We can see also that off-axis feedhorns are more affected by mirror distortions. This behaviour is highlighted by the XPD parameter variation, since the cross-polarization is more sensitive to surface deformations. For the XPD calculation, we considered the same coordinate system that we used to compute main beam parameters in Sec. 3.5. We should note also that the effect of gravity is stronger for higher elevation

---

[4] Elevation angles are measured from the horizontal position of the telescope, while zenith angles are measured from the zenith.

G1	Gravity with 90° elevation angle
G2	Gravity with 80° elevation angle
G3	Gravity with 70° elevation angle
G4	Gravity with 60° elevation angle
G5	Gravity with 50° elevation angle
G6	Gravity with 35° elevation angle
T1	Uniform temperature variation (+20° C)
T3	Unitary axial gradient
T5	Unitary lateral gradient along minor axes
W1	Wind load with speed of 12.5 m/sec
W2	Wind load with speed of 24.0 m/sec

Table 3.9: List of different load conditions of the telescope whose optical effect has been analysed, with their identification code.

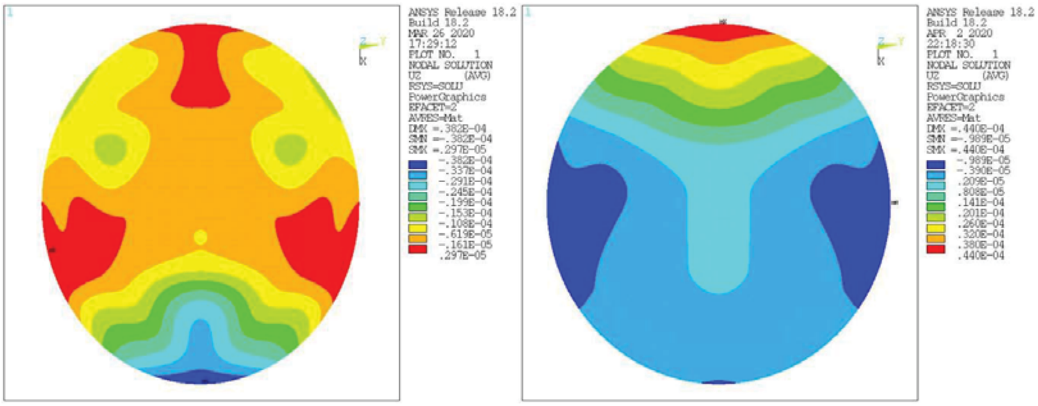

Figure 3.30: Optics deformation in the G1 configuration. The pictures show the displacement along the z-axis for the main (left) and sub-reflector (right).

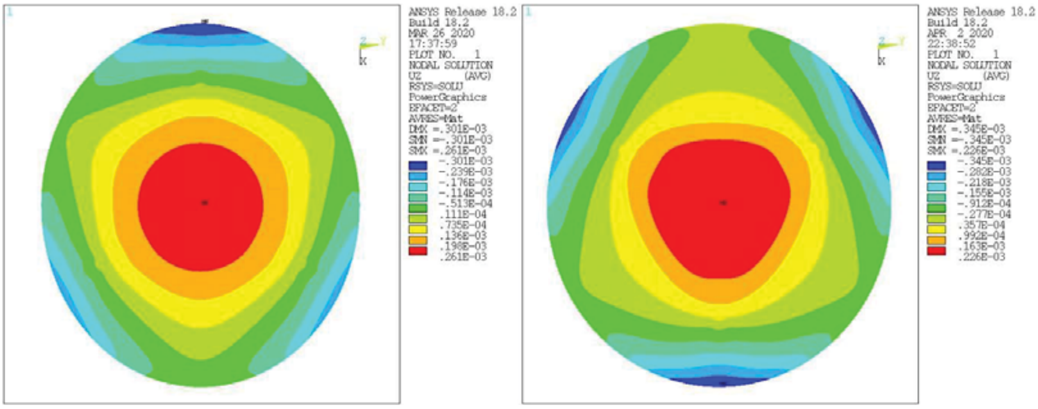

Figure 3.31: Optics deformation in the T1 configuration. The pictures show the displacement along the z-axis for the main (left) and sub-reflector (right).

Load	ΔFWHM$_A$ (%)	Δe (%)	$\Delta\mathcal{D}$ (%)	ΔXPD (%)
T1	0.0236	-0.0209	0.00	0.02
T3	-0.0031	0.0031	0.00	0.00
T5	-0.0009	0.0000	0.00	0.00
G1	0.0500	-0.0520	0.00	0.02
G2	0.0485	-0.0505	0.00	0.02
G3	0.0457	-0.0475	0.00	0.02
G4	0.0412	-0.0433	0.00	0.02
G5	0.0354	-0.0378	0.00	0.00
G6	0.0246	-0.0273	0.00	0.00
W1	-0.0108	0.0237	0.00	0.00
W2	-0.0435	0.0893	0.02	0.05

Table 3.10: Differences between main beam descriptive parameters computed with ideal reflectors and those simulated with a load for the feedhorn I_0.

Load	ΔFWHM$_A$ (%)	Δe (%)	$\Delta\mathcal{D}$ (%)	ΔXPD (%)
T1	0.0149	-0.0609	0.00	0.14
T3	-0.0029	0.0082	0.00	0.17
T5	-0.0015	0.0023	0.00	0.17
G1	0.0808	-0.0381	-0.02	0.17
G2	0.0764	-0.0399	-0.02	0.17
G3	0.0698	-0.0403	-0.02	0.17
G4	0.0610	-0.0396	0.00	0.17
G5	0.0502	-0.0376	0.00	0.17
G6	0.0312	-0.0325	0.00	0.17
W1	-0.0003	0.0525	0.00	0.14
W2	-0.0011	0.1878	0.00	0.14

Table 3.11: Differences between main beam descriptive parameters computed with ideal reflectors and those simulated with a load for the feedhorn R_0.

angles. Eventually, a point shift due to mirror distortions may occur and it should be carefully analysed.

CHAPTER 4

Strip sidelobes

In this chapter, I analyse the 4π beams of the Strip feedhorns coupled with the dual-reflector telescope, taking into account its shielding structure. This analysis is essential to understand the level of the sidelobes and their origin, so that we can try to mitigate them, since straylight contamination may be one of the most critical sources of systematic effects in observations of the Cosmic Microwave Background. Optical simulations are of primary importance for an optimal knowledge of instrumental characteristics, especially in the far sidelobe region where the power levels are extremely low, making direct measurements difficult and uncertain. We consider also the effect of the introduction of a forebaffle on top of the telescope aperture and how the beam is modified if we place an absorbent coating on the shielding panels.

4.1 Definition and analysis method

In principle, the Physical Optics method is the most accurate method to predict beams and may be used in all regions of the space surrounding the reflector antenna system. Nevertheless, as the frequency increases the reflectors have to be more precisely sampled. Besides, a finer integration grid is also required because in the sidelobe region the PO integrand becomes increasingly oscillatory.

For this reason, the sidelobes have been computed using the Multi-Reflector Geometrical Theory of Diffraction (MrGTD), which represents a suitable method for predicting the full-sky radiation pattern of complex mm-wavelength optical systems, because it computes the scattered field from the reflectors performing a backward ray-tracing (Nielsen 2000). The purpose of the MrGTD is to calculate the GTD fields from any number of reflectors illuminated sequentially starting at a given source. Reflector geometry, source characteristics, and output field points have to be defined, together with each contribution (i.e., a bundle of rays defined by a sequence of scatterers and by the type of interaction – reflection or diffraction – on each of them) to be taken into account to reach an accurate radiation pattern prediction.

The MrGTD is a GRASP tool based on backward ray tracing that uses a set of points generated on each reflector. All points are connected into a set of paths starting at the source and ending in the far-field direction. For each path, the fulfilment of the diffraction or reflection laws is tested. When the ray traces are found, possible shadows from all defined structures are detected. If no such intersections exist, the field is calculated by standard GTD method for each reflection or diffraction points. When many scatterers are involved, the amount of ray tracing contributions may lead to unacceptable computational time even with MrGTD. Since each contribution to the sidelobes is computed separately, it is crucial to identify the contributions which produce significant power levels in the resulting radiation pattern.

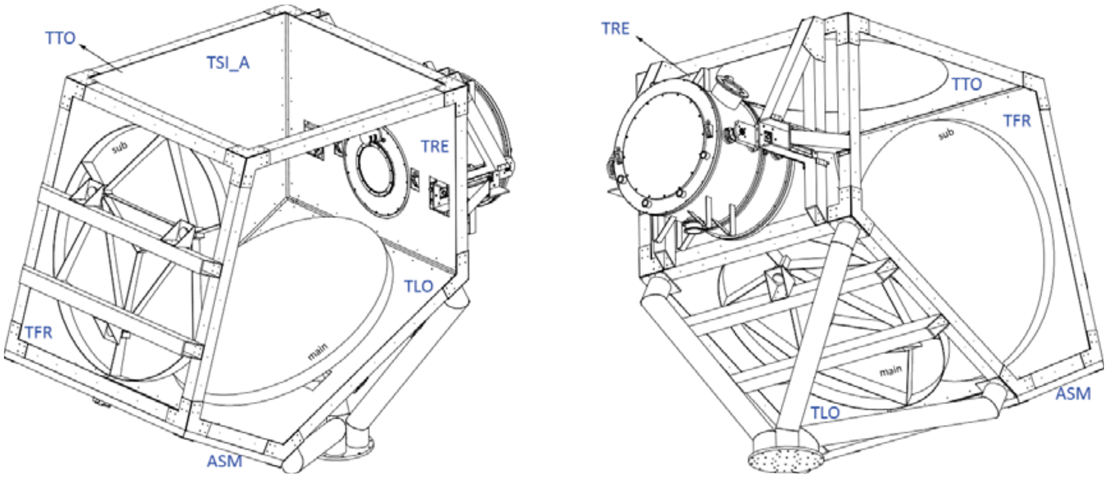

Figure 4.1: Mechanical design of the shielding structure, together with the nomenclature adopted to describe each panel.

4.2 Shielding structure

The Strip telescope is surrounded by a co-moving baffle made of seven aluminum plates of different shapes in order to reduce the contamination due to the sidelobes. Proper evaluation of the effect of shields is crucial, since these structures redistribute the power that is radiated by the horns and is not reflected by the telescope. Fig. 4.1 shows the mechanical design of the shielding structure, together with the nomenclature adopted to describe each panel.

4.2.1 Sidelobes simulations

In the simulations, the two reflector and the shielding structure have been considered as blocking structures. The shielding panels have been modelled as perfectly conducting surfaces. Using the MrGTD approach, each contribution to the sidelobes is computed separately, taking into account for interactions at different orders. Each interaction can be a reflection or a diffraction. We computed the sidelobes of the Strip telescope up to the 2^{nd} order of interaction at 43 GHz for some representative channels: feedhorn I_0, O_0, R_0 and Y_0.

As an example, Fig. 4.2 shows the co-polar contribution to the sidelobes due to radiation coming directly from the horn and not intercepted by the reflecting structures for the feedhorn I_0 at 43 GHz. The field is sampled with a $0.5°$ step both in the θ and ϕ coordinates. Sidelobes are represented as full-sky Mollweide projections using the HEALPix[1] visualization facilities, where the main beam axis points towards the North pole of the maps. Fig. 4.3 shows a 2^{nd} order contribution consisting of a series of two reflections, the first on a shielding panel and the second on the sub-reflector.

We computed a total of 240 contributions and Table 4.1 reports the brightest for each horn considered in the analysis. These feedhorns have been chosen as they should be the worst and best cases. As we can see, the worst contributions for the central feedhorn

---

[1] HEALPix is an acronym for Hierarchical Equal Area isoLatitude Pixelation of a sphere. This pixelation produces a subdivision of a spherical surface in which each pixel covers the same surface area as every other pixel. HEALPix provides a mathematical structure which supports a suitable discretization of functions on a sphere at sufficiently high resolution, and it facilitates fast and accurate statistical and astrophysical analysis of massive full-sky data sets (Gorski et al. 1999).

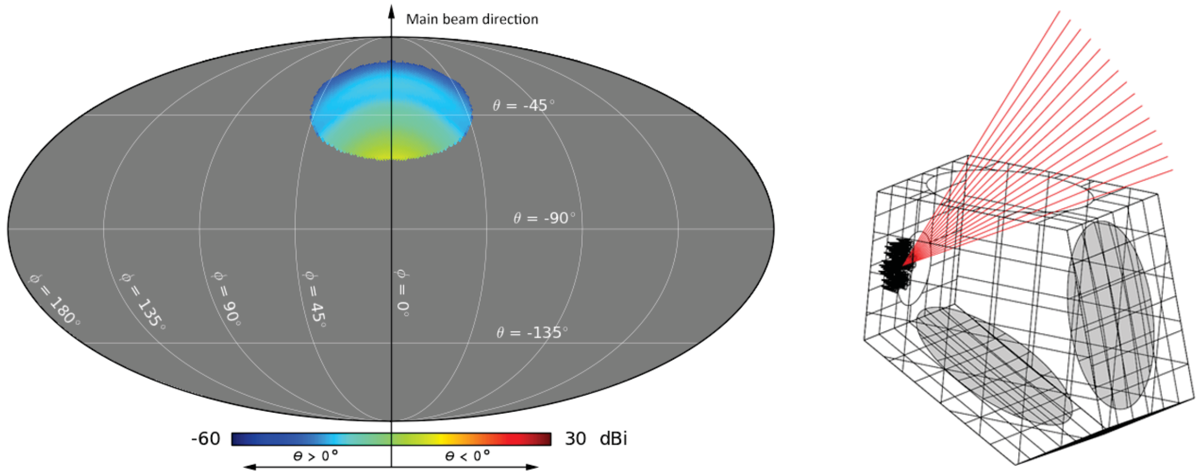

Figure 4.2: *Left*: 4π map of the field due to the rays coming from the feedhorn (direct contribution) is shown. Most of the map is empty (gray colour) because most of the rays are blocked by the baffle. The power peak of the direct contribution is -62.65 dB below the main beam directivity. *Right*: Sketch of the optics with the ray-tracing of the direct contribution.

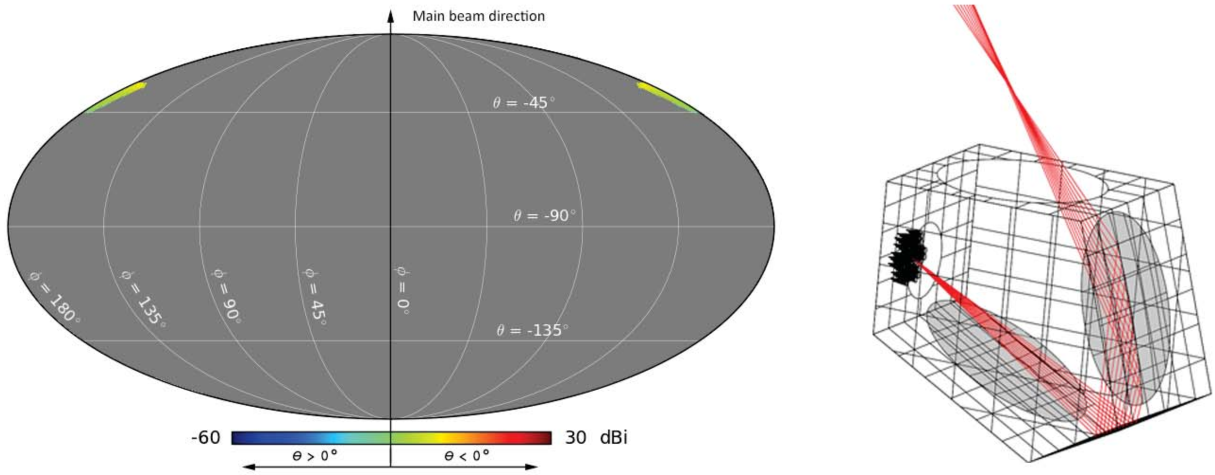

Figure 4.3: *Left*: 4π map of the field due to the rays that are reflect on the ASM panel and then reflected by the sub-reflector (namely ASMrSr contribution). The power peak of the direct contribution is about -58.46 dB below the main beam directivity. *Right*: Sketch of the optics with the ray-tracing of 2^{nd} order contribution.

Feedhorn I_0		Feedhorn R_3	
Contribution	Level (dB)	Contribution	Level (dB)
ASMrSr	-58.46	direct	-59.88
direct	-62.65	ASMrSr	-61.33
ASMrSd	-64.02	TTOd	-65.98
TTOd	-68.83	ASMrSd	-67.03
TSI_Ad	-78.88	SdTLOr	-75.95
TSI_Bd	-78.89	TSI_Bd	-75.97
Feedhorn O_2		**Feedhorn Y_1**	
Contribution	Level (dB)	Contribution	Level (dB)
MdSr	-53.16	ASMrSr	-55.68
ASMrSr	-58.17	ASMrSd	-60.79
direct	-61.70	direct	-65.99
ASMrSd	-63.20	TTOd	-71.86
TTOd	-67.66	ASMr	-76.99
TSI_Bd	-75.52	TLOrASMd	-77.11

Table 4.1: Brightest contributions to the sidelobes for the I_0, R_3, O_2 and Y_1 feedhorns on the 4π sphere with their power level computed with respect to the directivity of the main beam.

Feedhorn	Level (dB)
I_0	-58.69
R_3	-59.54
O_2	-53.17
Y_1	-56.76

Table 4.2: Maximum power level for the main contributions to the sidelobes with respect to the main beam directivity for the I_0, R_3, O_2 and Y_1 on the 4π sphere as calculated with the GRASP MrGTD.

I_0 are the direct, ASMrSr, ASMrSd and TTOd[2], which are characterized by a co-polar component lower than -58 dB with respect to the main beam directivity. This values should be compared with the requirement on sidelobe level, which should be lower than -65 dB: this means that the requirements are only marginally satisfied.

After calculating every single contribution at different orders, we summed them up to get the overall effect of the sidelobes. The final co-polar and cross-polar maps for the previous four feedhorns are shown from Fig. 4.4 to Fig. 4.7 and the maximum power levels in the sidelobes is reported in Table 4.2. The lower half of the full-sky map is empty due to the fact that we are using a ray-tracing technique combined with the fact that on top of the shielding structure there is a panel with a circular aperture; hence, rays can reach at most $\theta = \pm 90^\circ$.

The Mollweide projections show that the sidelobes are unevenly distributed and concentrated mainly in two areas, namely the direct contribution and the double reflection on the ASM panel. These contributions have already been show in Fig. 4.2 and 4.3. The

---

[2] The nomenclature is composed by the name in capitals of the panel on which the interaction occurs followed by the type of interaction (r for reflection, d for diffraction). For the panel names refer to Fig. 4.1.

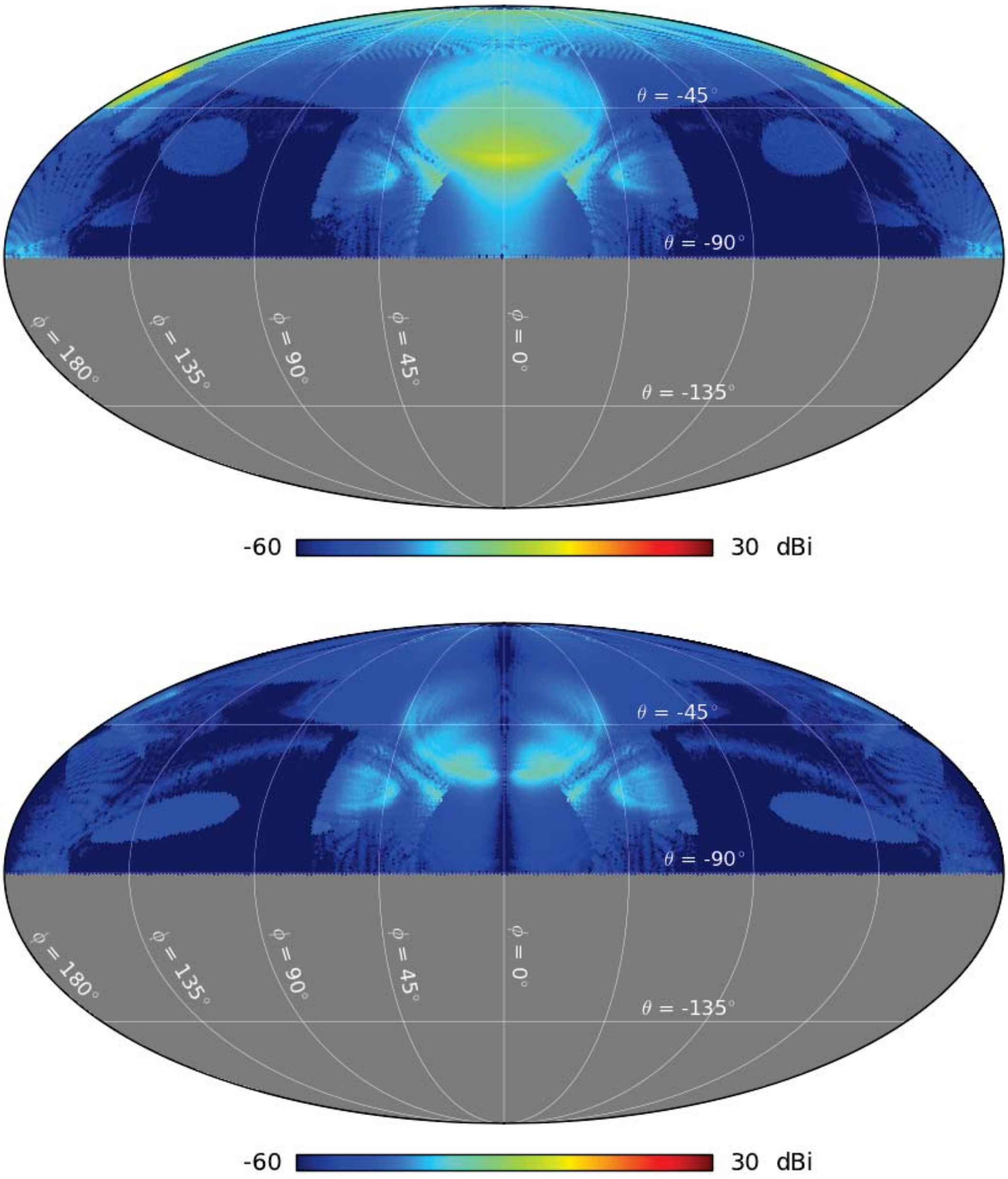

Figure 4.4: Co–polar (*top*) and cross-polar (*bottom*) component of the I_0 radiation pattern over the full sky computed with MrGTD.

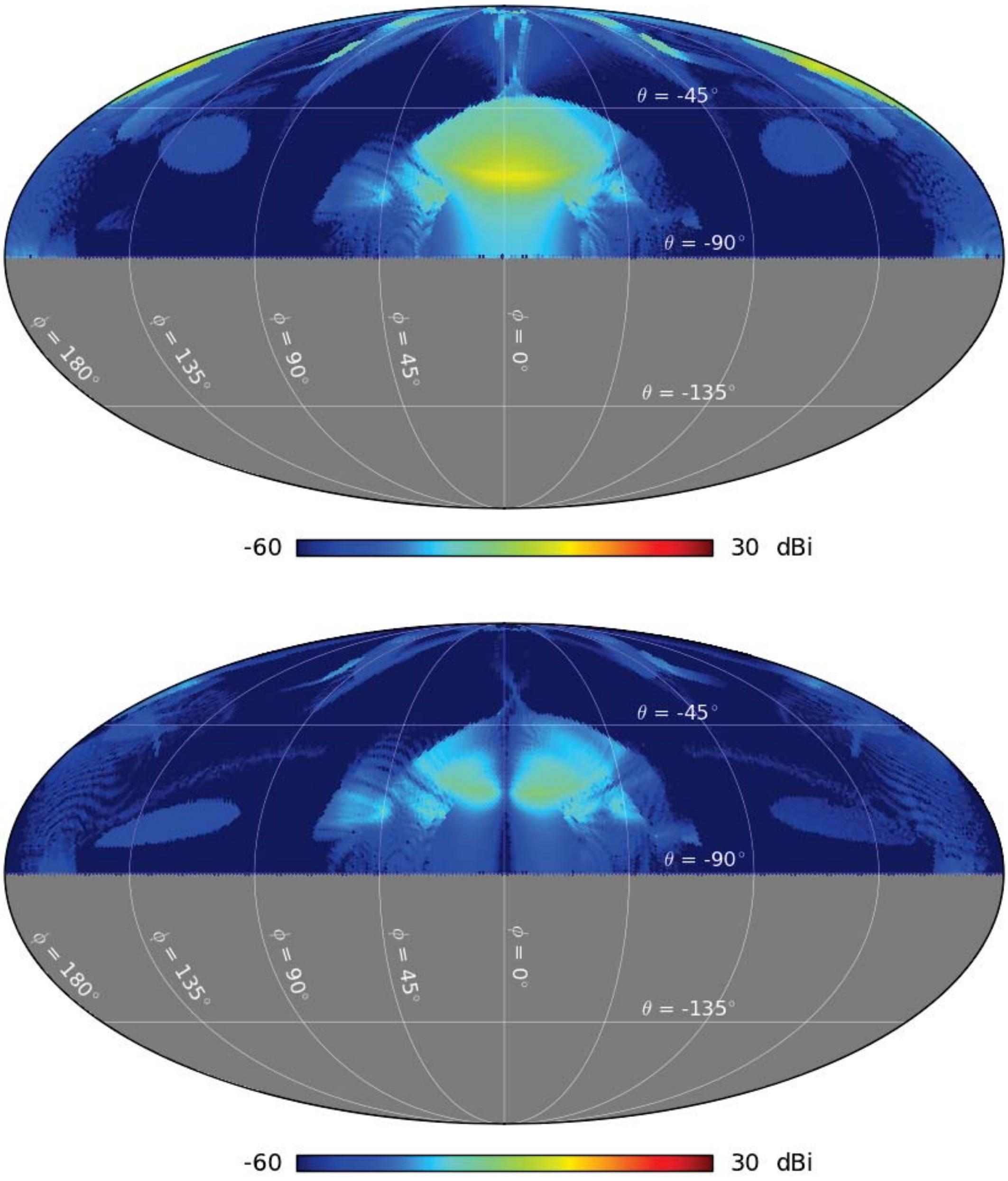

Figure 4.5: Co–polar (*top*) and cross-polar (*bottom*) component of the R_3 radiation pattern over the full sky computed with MrGTD.

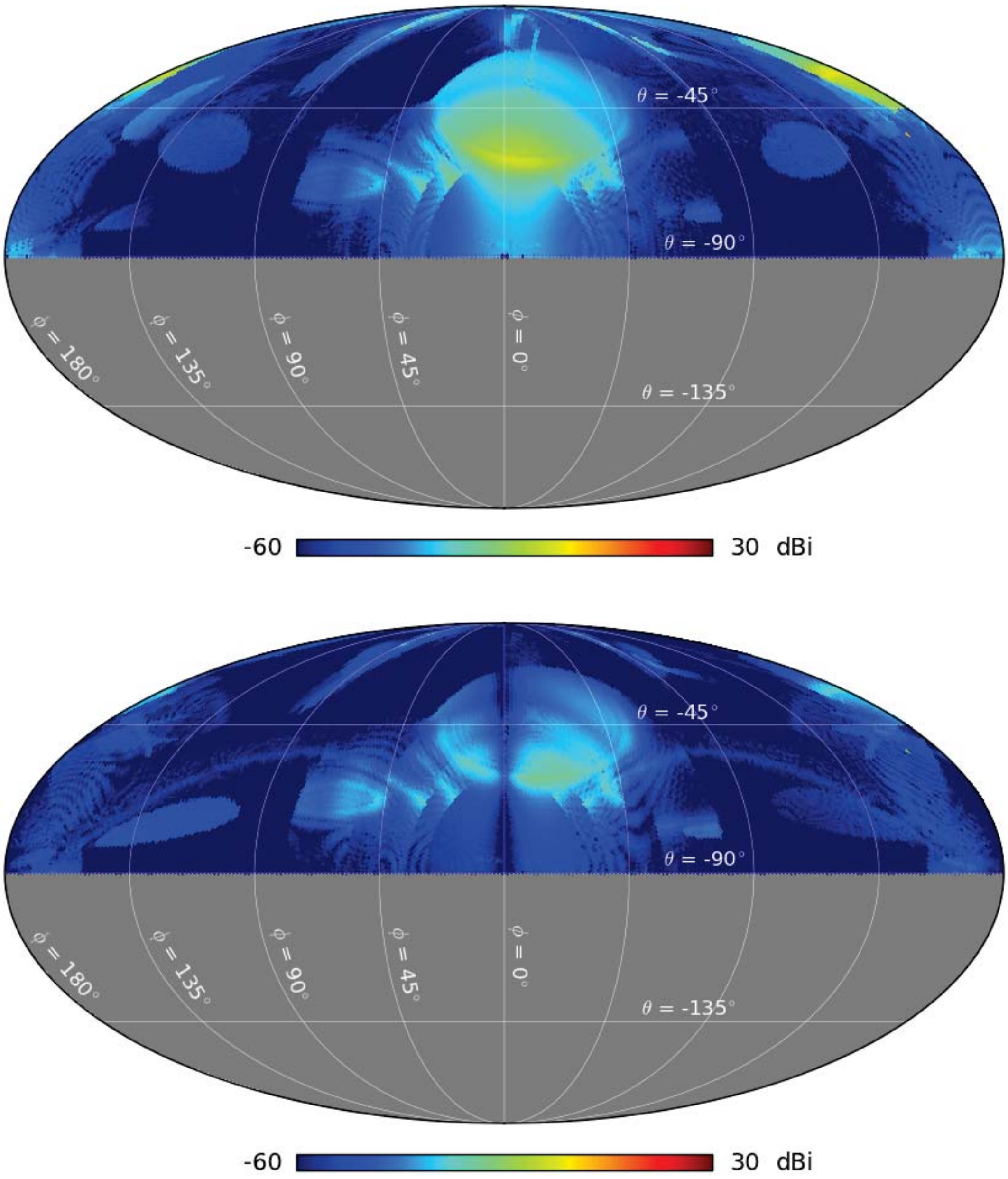

Figure 4.6: Co–polar (*top*) and cross-polar (*bottom*) component of the O_2 radiation pattern over the full sky computed with MrGTD.

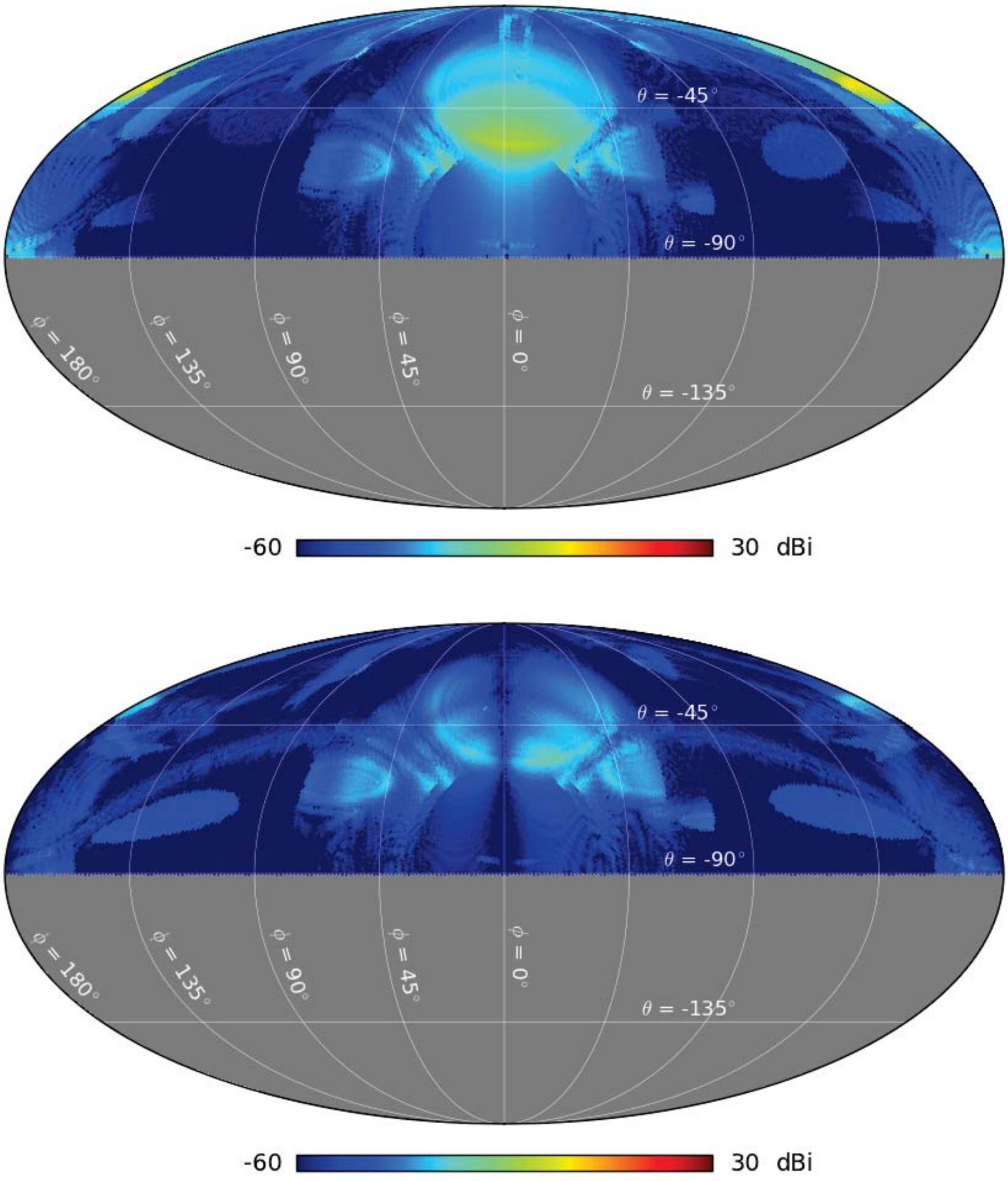

Figure 4.7: Co–polar (*top*) and cross-polar (*bottom*) component of the Y_1 radiation pattern over the full sky computed with MrGTD.

direct contribution is generated by the rays entering the feedhorns without any interaction with the reflectors; its shape and power level are given by the feedhorn radiation pattern pointing at about 60° from the telescope reference boresight. On the other hand, the double reflection is primarily due to rays reflected by one of the shields (ASM panel) and then reflected by the sub-reflector. These are the brightest contribution in the sidelobe region which lead to a maximum power level which does not marginally satisfy the requirements. The power level of the two contributions is comparable in the four feedhorn analysed (see Table 4.1). We notice that the double reflection affects an angular region narrower than the direct contribution, but it is closer to the main beam.

In principle, these contributions could be reduced with the introduction of a forebaffle placed on top of the telescope aperture and absorbers inside the shielding structure. In fact, this study with GRASP MrGTD is neglecting any absorbers used to minimize sidelobe pickup. Moreover, it does not take into account the envelope of the cryostat in which the feedhorn array is placed with its dielectric window.

Even if the requirement is marginally satisfied, the knowledge and possibly the reduction of the sidelobe level is still of major importance. In fact, the telescope sidelobes will pickup the 300 K emission of the ground, which could be polarized. This will depend also on the arrangement of the telescope at the observing site.

4.2.2 Forebaffle analysis

According to the results shown in the previous section, we investigated the possibility to introduce a forebaffle placed on top of the telescope aperture to reduce the sidelobe level. We started from the analysis of the direct contribution, which from previous simulations appeared to be one of the most harmful cause of the maximum power level in the sidelobes. Being a zero order contribution, it does not require a long computational time to investigate its behaviour. The work has been divided in different steps, starting from the simulation of the direct contribution without a forebaffle and then changing the height of the reflective baffle at the operational frequency of 43 GHz.

Using the information about ray traces stored in the GRASP $.trc$ file, we analysed the angular extension[3] and power of each direct contribution to the sidelobes for the 49 feedhorn of the Strip focal plane (Q-band). Fig. 4.8 shows the angular extension of each direct contribution along the θ coordinate (angles are given from the line of sight of the telescope). As we have already done previously, only half focal plane is reported for symmetry reasons.

We find that the closest angle to the line of sight is 12.04°, and is related to the feedhorn G_6; on the other hand, the farthest is 68.5°, which is connected to feedhorn R_3. As a reference value, the central feedhorn I_0 gives a direct contribution with a 43.56° angular extension on the $\phi = 0^\circ$ cut (from 19.44° to 63°). For these reasons, we focused the simulations on the following feedhorns: R_3, G_6 and I_0. Table 4.3 reports the main characteristics of the direct contribution of these feedhorns. Fig. 4.9 shows the co-polar component power as a function of θ with $\phi = 0^\circ$, which is the plane of the maximum angular extension.

After this analysis, we defined the baffle with a cylindrical structure (see Fig. 4.10). The electromagnetic model is based on four reflectors with a cylindrical surface with a 770 mm radius. The effect of the baffle on the direct contribution has been analysed for seven different heights of the baffling cylinder. Table 4.4 shows the angle at which the baffle geometrically stops the rays from each feedhorn analysed as a function of the

---

[3] With reference to Fig. 4.2, for a fixed ϕ, we can define the angular extension as the angular range along the θ coordinate affected by the contribution.

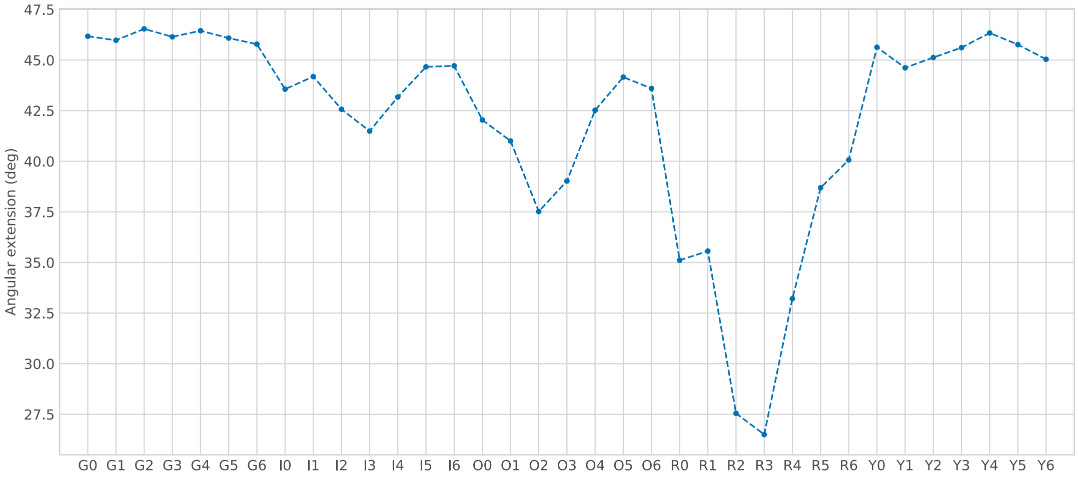

Figure 4.8: Angular extension along the θ coordinate of the direct contribution from each of the Q-band feedhorns of the Strip focal plane.

Horn	θ_{low} (°)	θ_{high} (°)	Extension (°)	Co-polar (dB)	Level (dB)
G_6	57.8	12.0	45.8	-9.25	-64.21
R_3	68.5	42.0	26.5	-2.59	-57.25
I_0	63.0	19.5	43.5	-5.04	-59.80

Table 4.3: Main characteristic of the direct contribution of the R_3, G_6 and I_0 feedhorns. The absolute power level is reported in dBi, together with the level with respect to the main beam directivity.

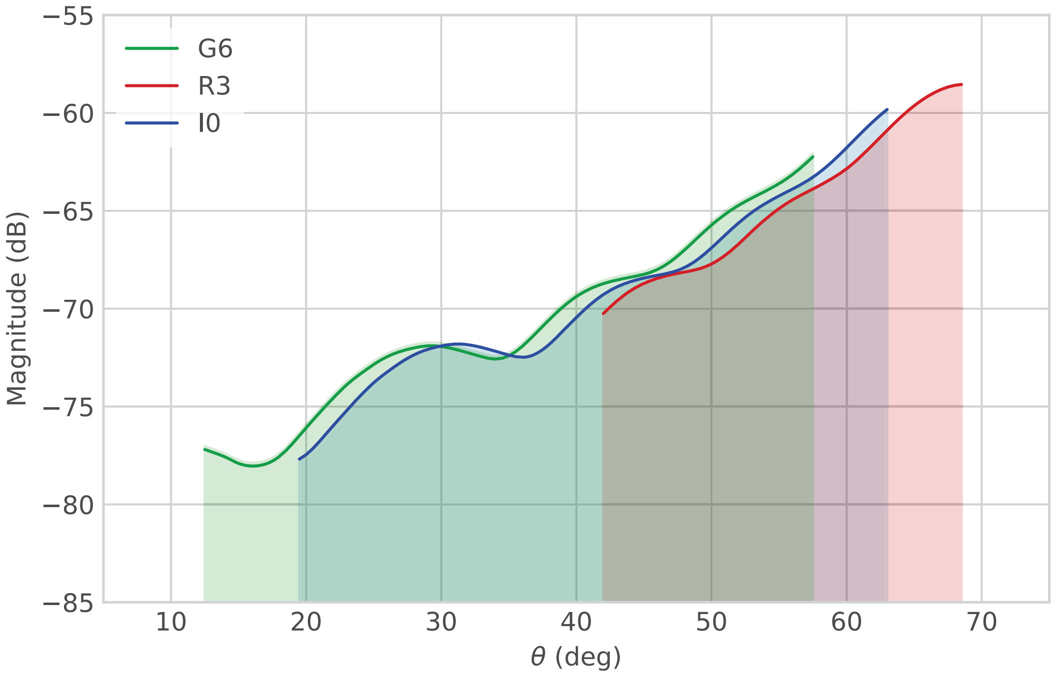

Figure 4.9: Co-polar component power as a function of θ with $\phi = 0°$.

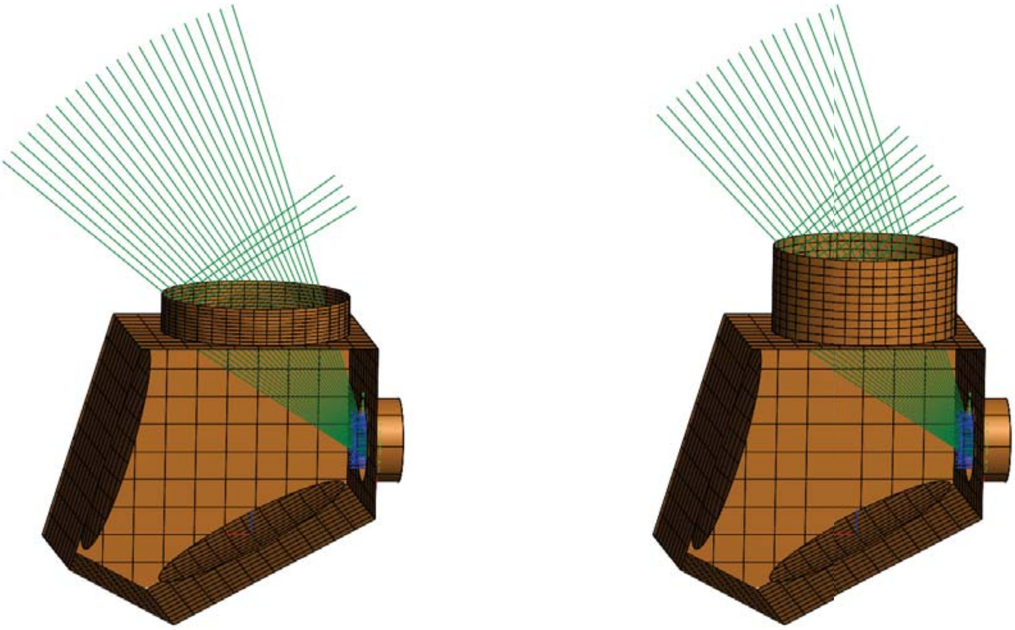

Figure 4.10: Electromagnetic model of the forebaffle with different heights: 300 mm (*left*) and 700 mm (*right*). We can see the effect on the direct rays coming from feedhorn G_6. The number of rays intercepted by the baffle increases with its heigth.

baffle height. Fig. 4.11 shows the variation of the maximum co-polar value for different baffle heights and for the three feedhorns considered.

We can see that the maximum power in the direct contribution is reduced with the introduction of the forebaffle and we find that a baffle height of 300 mm is enough to move the power level due to the direct contribution within the requirement. We computed again the sidelobes analysing reflections and diffractions on the reflecting cylindrical surface with a 300 mm height baffle and the resulting co- and cross-polar 4π maps are shown in Fig. 4.12. Looking at Fig. 4.10, we find that the baffle redirects the contribution at the lowest angles in other directions introducing a new reflection and diffraction on the baffling structure. This means introducing a further degree of uncertainty into the overall knowledge of the sidelobes. We should remind that the direct contribution

Height (mm)	Stopping angle (°)		
	I_0	R_3	G_6
0	27.0	21.5	32.2
200	32.0	27.0	36.5
300	34.0	29.5	38.5
400	36.0	32.0	40.5
450	37.5	33.0	41.5
500	38.5	34.0	42.5
630	41.0	37.0	44.5
700	42.0	38.5	45.6

Table 4.4: Stopping angle computed geometrically as a function of the baffle height for the three feedhorn analysed.

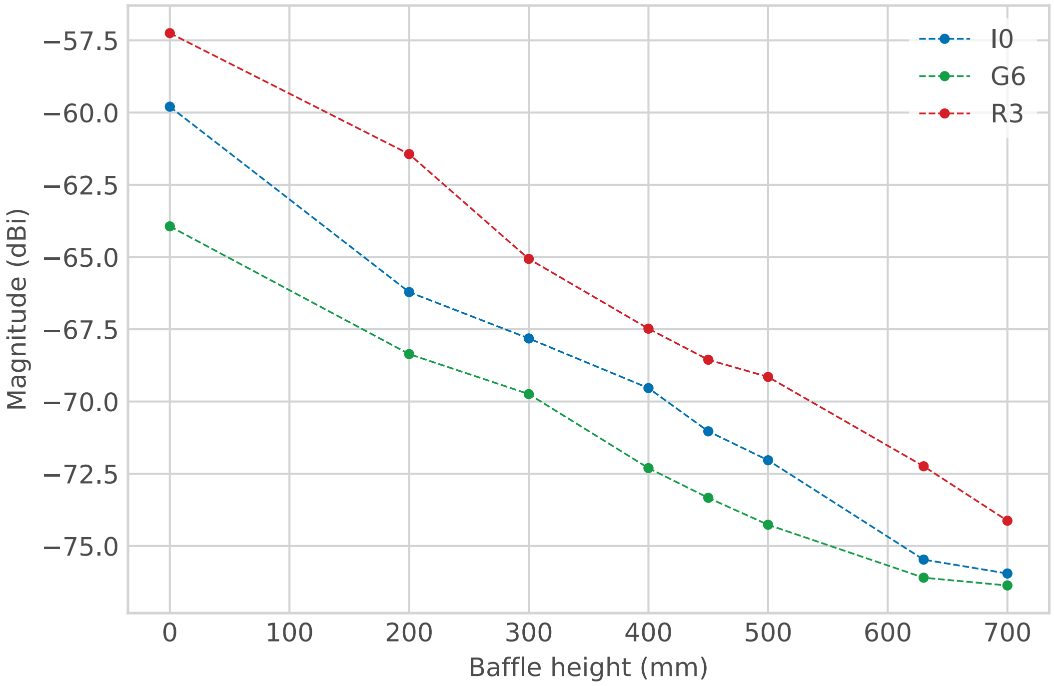

Figure 4.11: Variation of the maximum power level in direct contribution as a function of the baffle height.

corresponds to the feedhorn radiation pattern, which has been perfectly characterized with simulation and measurement, whose difference is within a fraction of dB. Therefore, the direct contribution can be described with a high accuracy in the data reduction phase. Moreover, a 300 mm baffle is not enough to intercept the ASMrSr contribution. This contribution would require a baffle higher than 1 m, which is not feasible due to mechanical constraints at the observation site (interference with the rooftop).

For this reason and due to the fact that the introduction of a forebaffle would have required a mechanical analysis not compatible with the tight schedule of the instrument, the Strip collaboration decided not to use a forebaffle for the telescope.

We did not consider the option of an absorbing baffle, which could absorb radiation instead of redirecting it, for the following reasons: modelling an absorber is not straightforward and we would introduce a further degree of uncertainty on the knowledge of the radiation pattern, thus degrading the knowledge of the optical response of the telescope.

4.3 Field on the shielding panels

Besides the computation of the edge taper reported in Sect. 3.4, we also simulated the power hitting the reflectors of the shielding structure for the feedhorn in the focus of the telescope. In particular, we considered the lateral panels (TSI) and the panel placed between the two mirrors (ASM). Due to the symmetrical configuration of the lateral panels, we report the results only for one of them. The analysis of the ASM panels is extremely important because it produces the double reflection inside the shielding structure, which is one of the main contributions to the sidelobe (see Sect. 4.2). In addition, this panel will be used to install an internal near-field calibrator; therefore, it will require a further in-

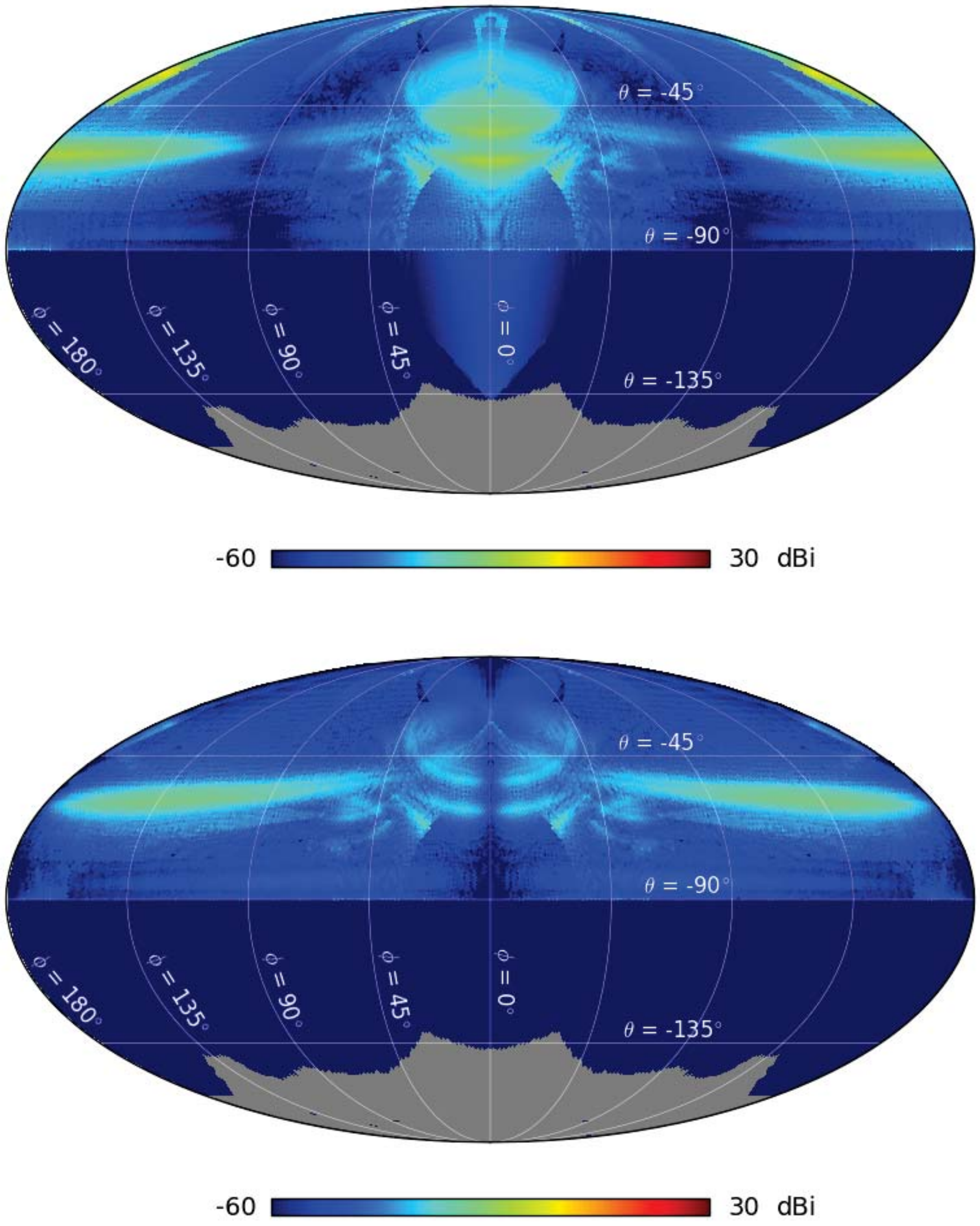

Figure 4.12: Co–polar (*top*) and cross-polar (*bottom*) component of the I_0 radiation pattern with the reflecting forebaffle.

Panel	Reflection	Max (dB)
ASM	direct	-70.13
	sub	-43.49
	main	-34.92
TSI	direct	-70.28
	sub	-35.61
	main	-28.74

Table 4.5: Maximum value of the total amplitude field on the shielding panels ASM and TSI.

vestigation.

The analysis of the field distribution is useful to understand how much power ends up on each panel and decide whether an absorbing coating is required. The contour plots of the total amplitude field incident on the panels have been computed in a surface grid with 701 × 701 points. The surface points are specified as a two-dimensional grid in x and y of the coordinate system of the scatterer. Top panels of Fig. 4.13 show the field distribution on the reflectors when the feedhorn is used as radiation source. Moreover, we computed the field distribution when the feedhorn radiation is scattered by the sub-reflector (central panels) and by the main-reflector (bottom panels). Table 4.5 reports the maximum values of the total amplitude field, which should be compared with the feedhorn directivity (23.93 dB).

Due to the absence of a forebaffle and to the fact that some reflections inside the shielding structure lead to a significant contribution to the sidelobe level, it has been decided to cover the inner structure with absorbent material.

4.4 Absorber effect

Absorbers in the RF/microwave frequency range are materials that attenuate the energy in an electromagnetic wave. They are used in a wide range of applications to eliminate stray or unwanted radiation that could interfere with the system operation. Absorbers are characterized by their electric permittivity and magnetic permeability, which are complex quantities generally written as

$$\begin{aligned} \varepsilon &= \varepsilon' - i\,\varepsilon'', \\ \mu &= \mu' - i\,\mu'', \end{aligned} \tag{4.1}$$

where ε' is called *dielectric constant* and describes the ability of a material to store energy. The imaginary component causes the losses in the materials and it is a measure of the attenuation of the electric field caused by the material. We can define also the electric *loss tangent* as $\tan\delta = \frac{\varepsilon''}{\varepsilon'}$. The greater the loss tangent of the material, the greater the attenuation as the wave travels through the material. A good knowledge of the permittivity and permeability of materials is essential to model the absorber performance. In most absorbers, both permittivity and permeability are functions of frequency and can vary significantly over even a small frequency range. However, it is difficult to get a detailed characterization of these parameters.

Absorbers can take many different physical forms, but we are interested especially in reflectivity absorbers, which reduce the reflection level compared to a perfect reflector. These can be realized with a multi-layer or with an impedance gradient. In the latter

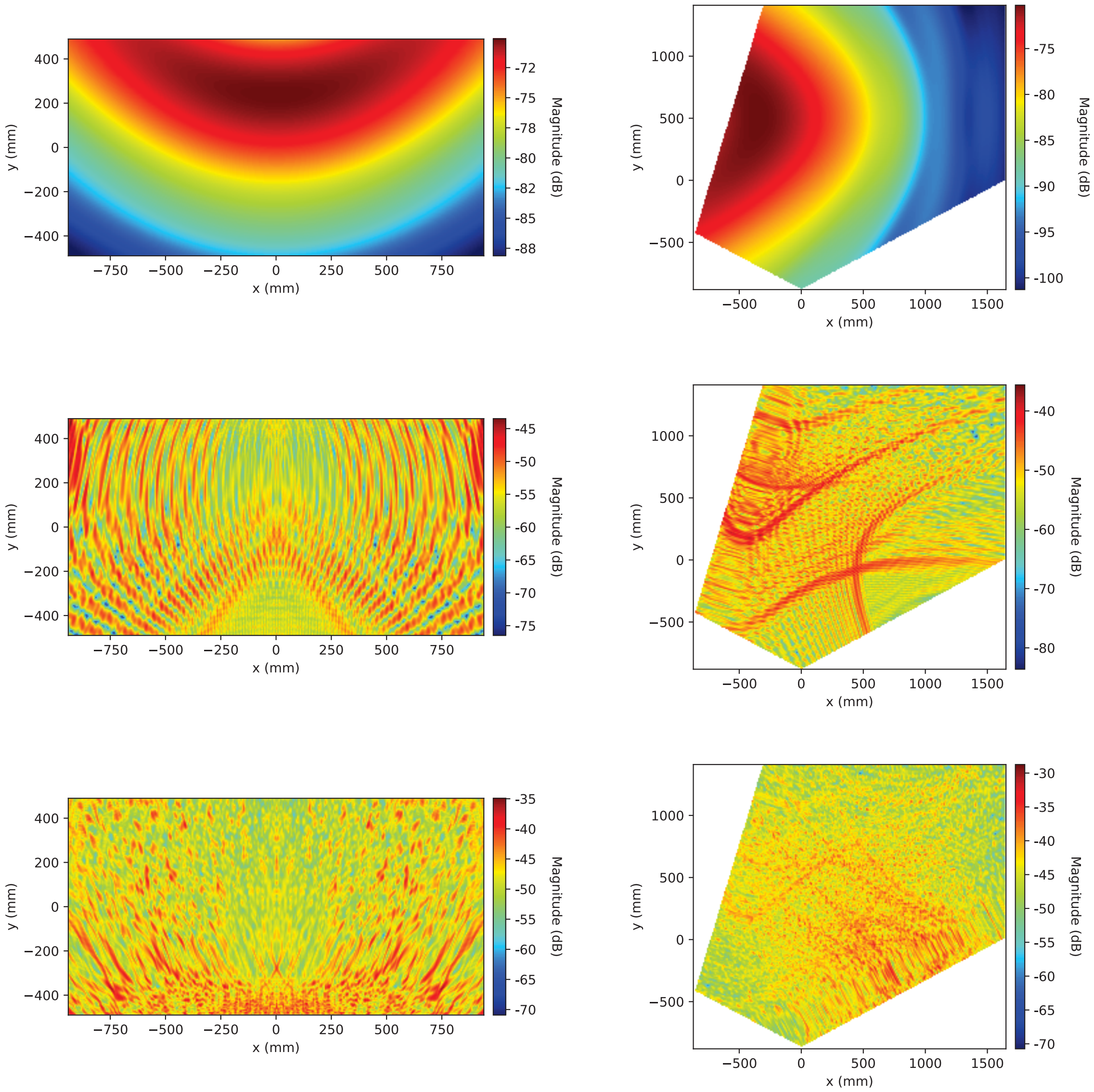

Figure 4.13: Field distribution for the feedhorn on the ASM reflector (*left panels*) and TSI reflector (*right panels*) at 43 GHz. The top row shows the field distribution when the feedhorn is considered as a direct source of radiation. The central and bottom row show the field distribution when the feedhorn radiation is scattered by the sub-reflector and main-reflector, respectively.

Figure 4.14: Picture of the broad band, carbon loaded polystyrene absorber with an operating frequency of 70MHz up to 40GHz provided by Comtest Engineering.

class, the impedance at the front face is very close to 377 Ω but gradually reduces to 0 Ω at the back face. Since there is no abrupt transition layer, there is no point which will cause a large reflection. The impedance gradient is obtained shaping the material so that the wave 'sees' a small portion of the material at the front face and a gradually increasing portion as it travels into the material. The most common shape is a pyramid.

The absorbent material chosen for the Strip telescope will be provided by the company Comtest Engineering and it is a closed cell polystyrene absorber. The benefits of this kind of absorbers are light weight, uniform carbon cell loading, removable tapers (see Fig. 4.14) and broad band, with an operating frequency from 70 MHz to 40 GHz. The absorbers base plate thickness is 50 mm and it will be used without the taper to reduce the interference inside the telescope shielding structure. The material dielectric constant is 1.1, but the loss tangent is not given. Knowing that the absorber provides a 12 dB attenuation, we tried to retrieve the dielectric constant by means of electromagnetic simulations with GRASP.

We want to model a flat slab of uniform, isotropic, lossy material backed by the perfect conductor and this can be done in GRASP modelling the absorbing panel as a dielectric layer, i.e. a plate of dielectric material of given thickness and relative dielectric constant, which may be complex to account for losses in the material. It requires to define a displacement relative to the surface scatterer and the conducting surface must be specified as a separate layer.

Fig. 4.15 shows the beam pattern reflected by a panel covered with a dielectric layer with different values of $\tan\delta$ on the radiation pattern of a simple feedhorn. The simulation is repeated for normal and oblique incidence. The panel, the distance of the feedhorn and oblique incidence angle are the one of the Strip telescope. We can see that the attenuation changes as a function of $\tan\delta$. With these simulations, we found that an attenuation of 12 dB can be achieved setting $\tan\delta = 0.03$.

To check the effect of placing an absorber on the ASM panel, we computed the radiation pattern using Physical Optics, which is the most accurate method, even if time consuming. We simulated the main contributions: the nominal optical path, the direct contribution, the double reflection which occurs on the ASM panel and other possible

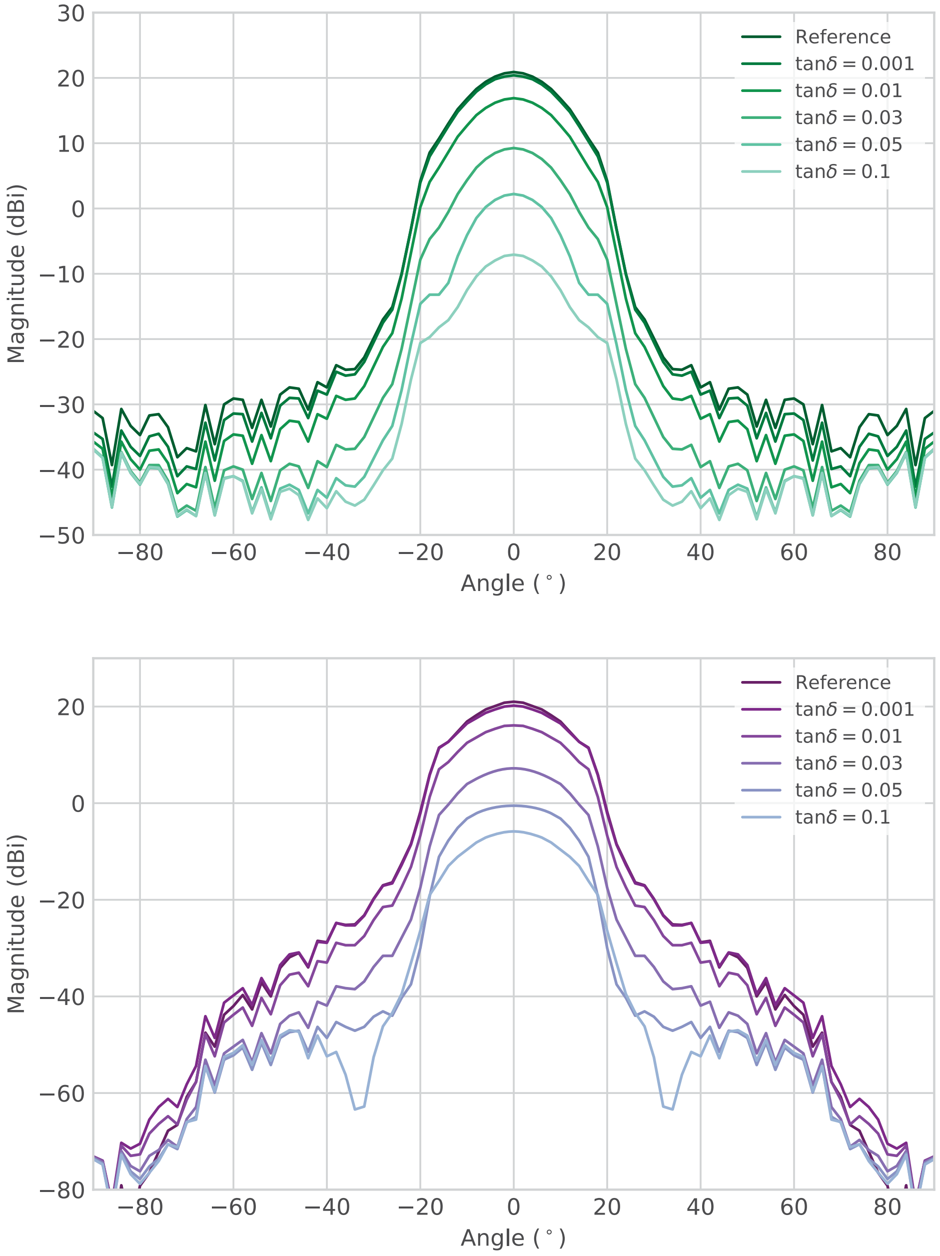

Figure 4.15: Effect of a reflecting panel covered with a dielectric layer with different values of $\tan\delta$ when illuminated by a feedhorn with normal (*top*) and oblique (*bottom*) incidence.

contributions due to the sub-reflector, like self-obscuration. Fig. 4.16 shows a scheme of the telescope with the ray-tracing of the main contributions which are reported also in the radiation pattern on the bottom panel. It shows the main optical path, the direct contribution, which affects the angular range $[-40°, -60°]$, and the contributions coming from the sub-reflector, which include the double reflection on the ASM panel around $33°$ and the possible self-obscuration of the mirrors. Adding up these contributions, we get the total co-polar radiation pattern for the feedhorn I_0 at 43 GHz shown in Fig. 4.17. Note that the radiation pattern is represented in the angular range $\pm 90°$ because it takes into account also the effect of the circular aperture on top of the telescope structure.

From this analysis, we found an additional contribution to the sidelobes, which appears as a 3^{rd} order interaction and affects angles around $51°$, introducing a peak with a power level over the requirement. The ray tracing of this contribution, which is made of a sequence of three reflections, is shown in Fig. 4.18. Third order sidelobes were not computed due to lack of time; however, this contribution will be included in future analysis.

Then, we repeated the same simulation adding a dielectric layer placed over the ASM panel. According to the simulations reported previously, we expected to see a reduction in the power level of the peaks related to the reflections occurring on this panel, thus moving the sidelobe level within the requirement; however, we did not see a significant variation in the sidelobe level. To check this unexpected behaviour, we verified the angular response of the single ASM panel when illuminated by the sidelobe of the Strip feedhorn. Fig. 4.19 shows the comparison between the cut obtained treating the panel as perfect reflector and with the addition of the absorber. As we can see, the problem shows up already at this level: we see a variation only at high angles, but not in the reflection peak at $-15°$, which is the one that will hit the sub-reflector. Thus, we will have to understand and verify how the dielectric layer is behaving when not directly illuminated by the feedhorn main beam. This last result calls for a further investigation of the way in which the absorber should be modelled, since our choice might not be the right one. A possible improvement would be to perform the same analysis with other tools that are more suitable for treating materials which are not perfect conductors.

4.5 Considerations on sidelobe analysis

The analysis of the Strip telescope sidelobes showed that there are two regions in which the requirements are only marginally satisfied. These regions are related to the direct contribution, which influences an angular region around $60°$ from the main beam, and to a double reflection inside the shielding structure, which shows up at $\sim 33°$. Their power level is comparable and close to the requirement of -65 dB.

We analysed two possible ways to reduce the sidelobe level: a reflecting forebaffle on top of the telescope aperture and an absorber inside the shielding structure. The collaboration decided to not add the baffle as it would increase the degree of uncertainty on the overall knowledge of the sidelobes and due to mechanical and schedule constraints. Eventually, the decision fell on the placement of an absorbing coating on the panels of the shielding structure. We tried to analyse the effect of this absorber, modelled as a dielectric layer; however, the results are not well understood or convincing. The absorber model is still an open issue and we will keep on working on it because the use of a coating is the current baseline for the telescope.

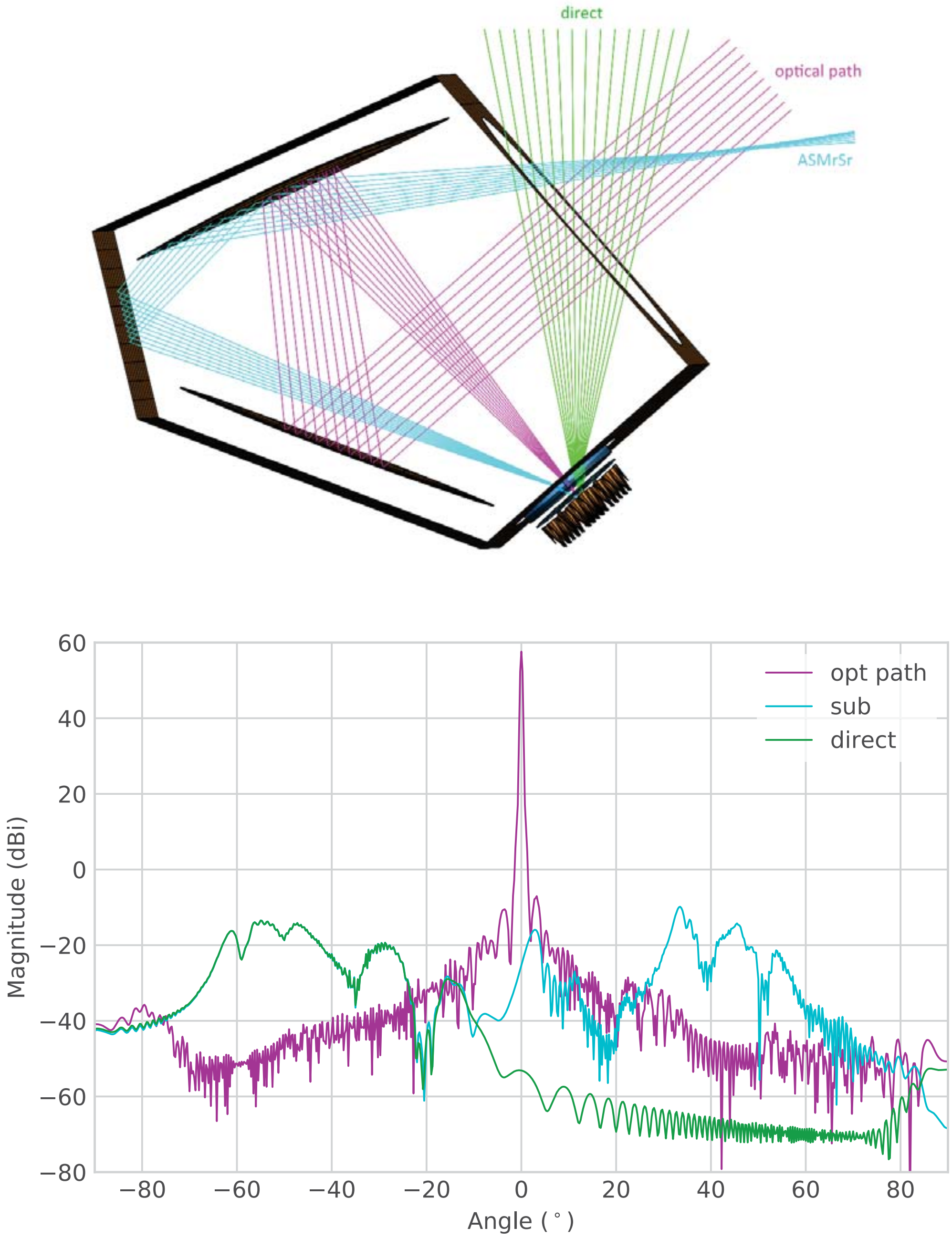

Figure 4.16: *Top*: Scheme of the telescope with the ray-tracing of the main contributions. *Bottom*: Total radiation pattern which takes into account the main contribution shown in the telescope scheme. We can see the main optical path, the direct, and the contributions coming from the sub-reflector, which include the double reflection on the ASM panel around 33° and the possible self-obscuration of the mirrors. The simulation has been done for the feedhorn I_0 at 43 GHz without any absorber.

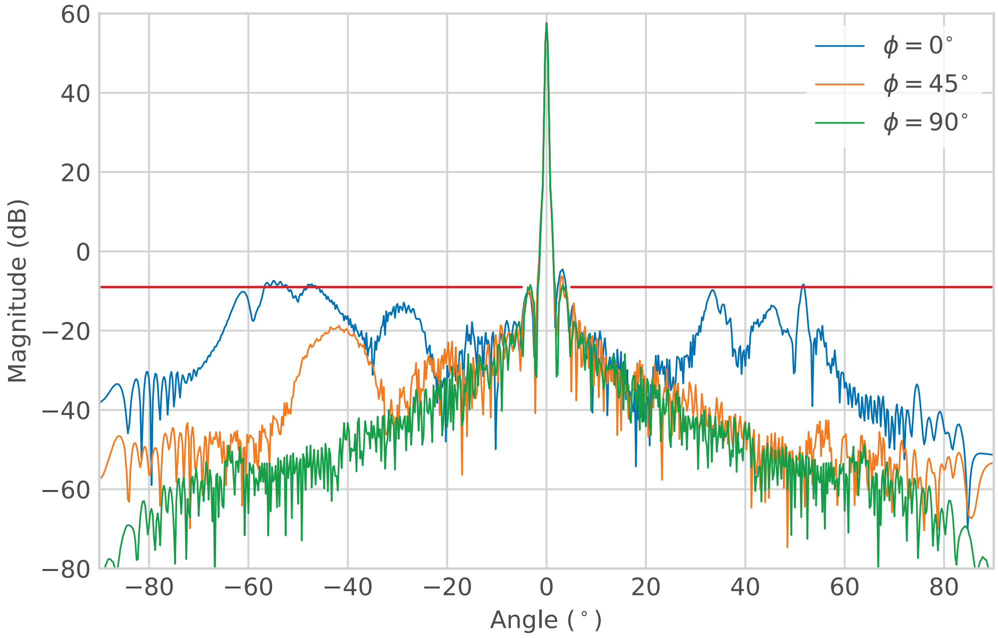

Figure 4.17: Radiation pattern of the feedhorn I_0 at 43 GHz computed with GRASP Physical Optics method without any absorber at different ϕ cuts compared with the requirement of -65 dB below the main beam peak.

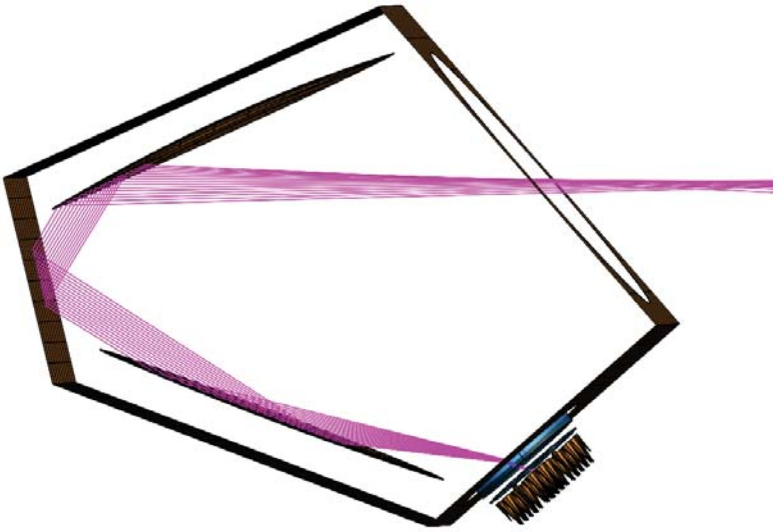

Figure 4.18: Ray-tracing of the third order contribution which introduces a peak with a power level higher than the requirement. It is made of a sequence of three reflections.

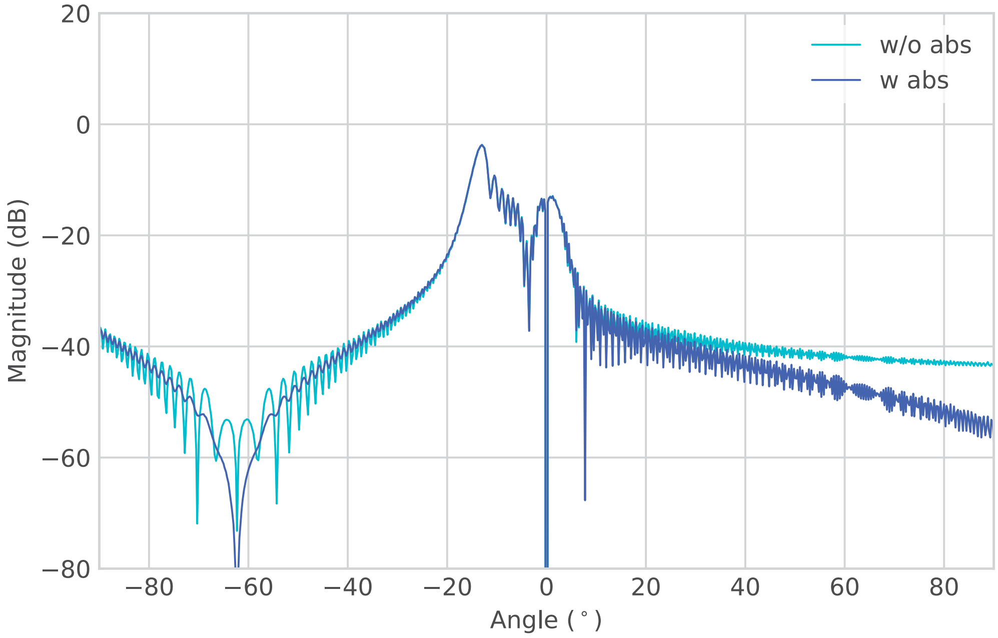

Figure 4.19: Comparison between the cut obtained treating the ASM panel as a perfect reflector and with the addition of the absorber, modelled as a dielectric layer.

CHAPTER 5

Impact on observations

Beams characteristics have a strong impact on the observation of the polarized CMB sky. Angular scales smaller than the telescope resolution are inevitably smoothed, with the consequent loss of details at scales below the angular resolution of the Strip optics. This is not an issue, since the instrument aims at large angular scales. Nevertheless, there are still some unwanted optical aberrations, which play a key role on observations: the main beam asymmetries due to the off-axis configuration of the telescope, the spurious effect of the cross–polarized component, as well as the not–negligible level of sidelobes, inevitably impact on the measurements of the CMB polarization signal.

A comprehensive knowledge of the beam radiation pattern would in principle allow the reconstruction of the true signal from the sky, within the accuracy limits imposed by systematic effects. Besides the difficult measurement of the real beam response at power levels of several tens of dB below the peak, also the effect of the instrument scanning strategy has to be taken into account. The signal measured in a given direction in the sky is indeed the result of a superposition of observations, where the actual orientation and rotation of the scanning beam changes with time and ultimately depends on the scanning strategy of the instrument.

In the following, we use the LevelS simulator to study the impact of the optical response on the CMB polarization measurements, when observing the sky with the nominal scanning strategy.

5.1 The LevelS simulator

The Strip LevelS is a numerical tool that simulates the instrument detectors response when observing the sky with a scanning strategy. It takes into account for the mission details such as the latitude of observation, instrument pointing, the beam response and a possible noise contribution from the instrument itself. It derives from Planck–LFI LevelS (Reinecke et al. 2006) and it employs the same workflow with a specific customization.

LevelS is organized into modules, each accomplishing one or more tasks in the processing. With reference to Fig. 5.1 that shows a block diagram of the typical LevelS operations, we give an overview of the simulation modules, focusing on those we use in our analysis of the Strip optical response.

The pipeline modules

Main inputs to the LevelS for the analysis of main beam effects are (*i*) the CMB sky maps to be observed, (*ii*) the scanning beam, (*iii*) the scanning strategy and (*iv*) a focal plane database including information about each detector. Some of these inputs are provided

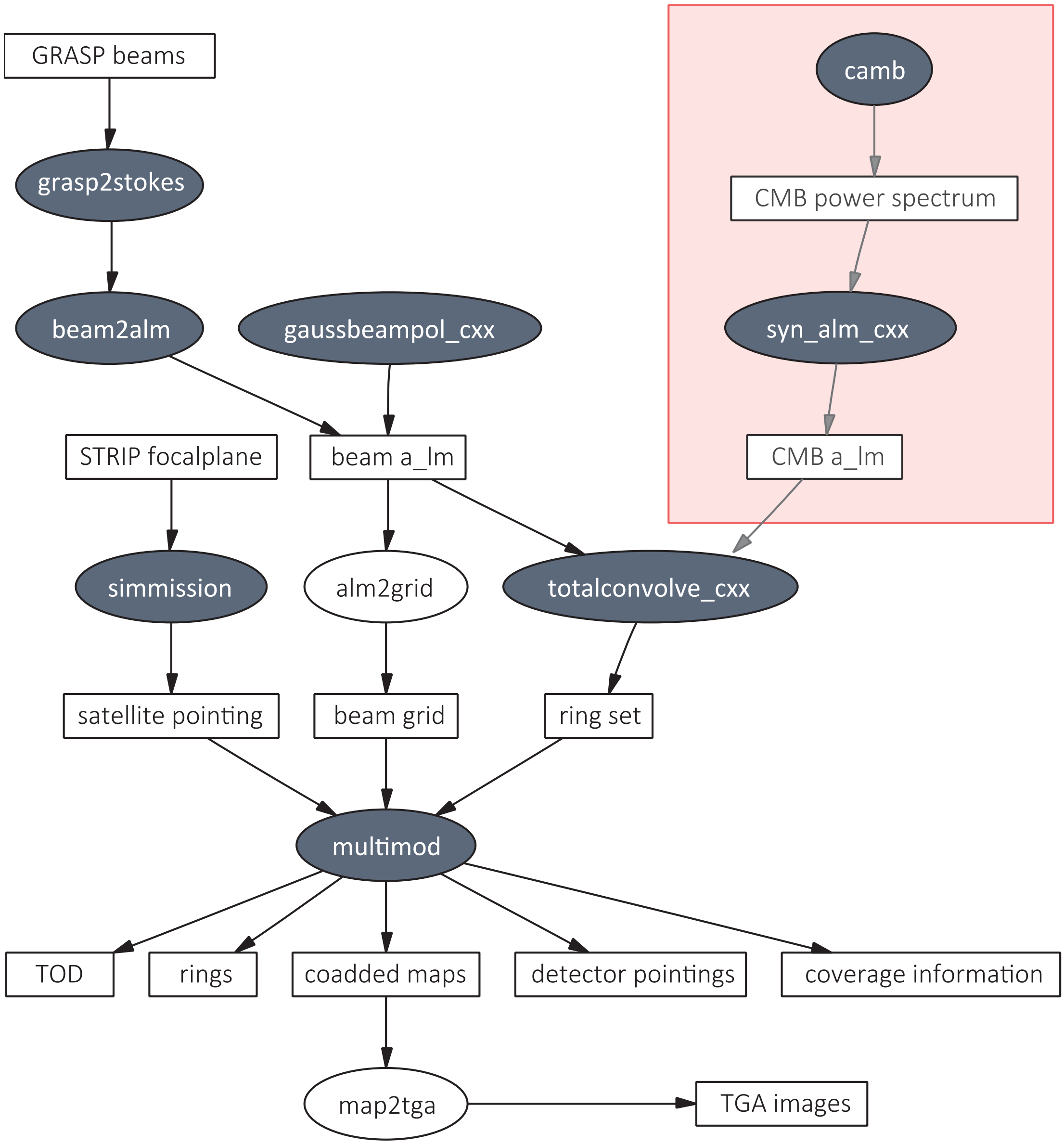

Figure 5.1: Schematic data flow of the LevelS in a typical Planck simulation pipeline. Rectangular components denote parameters or data products, whereas elliptic shapes represent modules (Reinecke et al. 2006). Grey shaded modules are those used in our analysis, suitably customized. The pink shaded area includes modules used to generate the CMB map to be observed.

by third-party software tools and have to be opportunely processed to be used by LevelS modules.

- **CAMB**: the *Code for Anisotropies in the Microwave Background*, `CAMB` (Lewis & Challinor 2011), produces a CMB power spectrum from a set of cosmological parameters. It also provides a realization of this power spectrum using the `syn_alm_cxx` module, which is part of the Healpix facilities (Gorski et al. 1999), resulting in a set of $a_{\ell \mathrm{m}}$.

The task of the following modules is to provide the second input to the convolution process, that is a spherical-harmonic transform of the beam. The main beam simulated with GRASP is expanded into spherical harmonics using the `grasp2stokes` and `beam2alm` modules.

- **grasp2stokes**: this module converts a GRASP cut or grid beam file into the corresponding Stokes parameters, as an input for the `beam2alm_lspe`;
- **beam2alm**: this module, in turn, converts the Stokes parameters of the beam into the $a_{\ell \mathrm{m}}$ coefficients.

Information on the scanning strategy and the beam pointing during the observation are encoded by the two input modules `simmission` and `focalplane_strip`, respectively, as reported in Figure 5.1.

- **simmission**: the output of this module is a table containing the position and orientation of the Strip telescope in fixed time intervals during the entire observation time. It accounts for the nominal scanning strategy: a constant zenith angle scanning (nominally 20°) from a 28° latitude, with 1 r.p.m. spin rate;
- **focalplane_strip**: this module converts a text file containing several information on the instrument focal plane into the `fits` format[1]. The focal plane database consists in forty-nine lines, corresponding to the forty-nine Q-band detectors of the instrument. Each line includes detector ID string, position in the focal plane, polarization angle, observing frequency and sampling frequency at which the final output TOD (Time Ordered Data) are sampled. The most important information for our analysis are the angles that describe the position of the detectors in the focal plane since they give the rotation of the beam pattern from a fiducial orientation (forward beam direction (z-axis) pointing along the telescope reference boresight, with y-axis aligned with the nominal scan direction) to their positions in the focal plane.

When all inputs to LevelS have been processed by the relevant modules, the convolution of the beam with the observed sky signal is performed in the spherical harmonics space (`totalconvole_cxx`), by taking into account for the Strip scanning strategy and resulting in the TOD of the Strip detectors (`multimod`).

- **totalconvolve_cxx**: this module takes as input the spherical harmonic coefficients of the simulated sky map and the beam $a_{\ell \mathrm{m}}$ of each detector. Then it computes the convolution of sky and beam for all possible directions and orientations of the beam relative to the sky;

---

[1] Flexible Image Transport System (`fits`) is a digital file format useful for storage, transmission and processing of scientific images and tables. `fits` files are most commonly used in astronomy. The input and output files used in the developed pipeline and shred between modules are all written and stored in this format.

- **multimod**: this module produces the time stream of the detector pointings at the wanted sampling frequency and the so-called *hits map*, giving the number of detector pointings falling in each pixel at the desired HEALPix Nside resolution. To obtain the detector pointings the telescope positions and orientations obtained with the `simmission` module are interpolated and rotated considering the actual position and orientation of each detector relative to the telescope coordinate frame. Giving the detector pointings and the output of the `totalconvolve_cxx`, the module calculates also the radiation falling into each detector (for the three Stokes parameter I, Q and U) producing the final TOD files, which thus take into account the convolution of the simulated sky with the beam. I, Q and U maps of the simulated observed sky can also be produced.

5.2 Main beam analysis

To characterize the impact of Strip main beams on CMB observations, we evaluate the *beam window function*. We recall that the finite angular resolution of an instrument $b\left(\hat{n},\hat{n}'\right)$ can be described through a convolution in real space as

$$T_{obs}\left(\hat{n}\right)=\int b\left(\hat{n},\hat{n}'\right)\,T\left(\hat{n}'\right)\,d\Omega, \tag{5.1}$$

which is equivalent to a low-pass filter in harmonic space, and whose effective action on the power spectrum can be written as

$$C_\ell^{obs}=W_\ell\,C_\ell\,, \tag{5.2}$$

where W_ℓ is the beam window function and $T\left(\hat{n}\right)$ is the usual temperature field defined in (1.24). In principle, for full-sky maps, the effective azimuthally averaged beam window function can be estimated directly by inverting equation (5.2):

$$W_\ell=\frac{\left\langle C_\ell^{obs}\right\rangle}{C_\ell}, \tag{5.3}$$

where C_ℓ^{obs} is the power spectrum of simulated CMB-only maps, C_ℓ is the fiducial model used as input, and the ensemble average is taken over the Monte Carlo simulations. However, in the realistic case we mask out some regions of the sky that are contaminated by foreground, and the above equation no longer applies.

Instead, using the same notation as in Hivon et al. (2002), we can write

$$\left\langle C_\ell^{obs}\right\rangle=\sum_{\ell'}M_{\ell\ell'}\,W_{\ell'}\,\left\langle C_{\ell'}\right\rangle, \tag{5.4}$$

where the coupling kernel $M_{\ell\ell'}$ encodes the geometric mode–mode coupling effect introduced by masking the sky and any instrumental noise contribution is neglected.

Strip will observe a fraction of the sky $f_{\mathrm{sky}}\approx 37\%$, thus most of the sky is masked. For this reason full-sky approximation should not be used, since such a strong masking has non-negligible effects on the calculation of the power spectrum. Nevertheless, we are not interested in recovering the *real* power spectrum, but in the evaluation of the beam window function, that is $B_\ell=\sqrt{W_\ell}$, so that we can write

$$B_\ell=\sqrt{\frac{\left\langle C_\ell^{obs}\right\rangle}{C_\ell^{\mathrm{mask}}}}, \tag{5.5}$$

Table 5.1: Cosmological parameters for the `CAMB` processing. All other parameters are set to the default standard of the April 2014 version of `CAMB` (see `http://lambda.gsfc.nasa.gov/toolbox/tb_camb_form.cfm` for further details).

Parameter	Value
Age of Universe (GYr)	13.938
$\Omega_b h^2$	0.02260
$\Omega_c h^2$	0.11200
$\Omega_\nu h^2$	0.000064
Ω_Λ	0.70924
Ω_K	0.000000
Ω_m $(1 - \Omega_K - \Omega_\Lambda)$	0.29076
100θ (CosmoMC)	1.03419
τ_{rec} (Mpc)	284.86
τ_{now} (Mpc)	14435.0

where C_ℓ^{mask} is the CMB power spectrum of the input sky model when it is masked as for the Strip scanning strategy. Therefore, the mode-mode coupling and the $f_{\mathrm{sky}} < 1$ due to the masking cancels out in our calculation.

We can distinguish between “optical beams” and “effective beams”. The optical beam is the optical response of the feedhorn coupled to the telescope. It is independent both from the radiometer response (bandshape and non-linearity) and from the telescope motion (spinning and scanning strategy). It represents the pure optical transfer function. The main beam properties of the optical beams have been evaluated in Section 3.5. On the other hand, we define the effective beam as the average of all optical beams that cross a given pixel of the sky map, given the Strip scanning strategy and the orientation of the optical beams themselves when they point to that pixel. The effective beams capture the complete information about the difference between the true and observed images of the sky. Their convolution with the true CMB sky produce the observed sky map. Similarly, the effective beam window functions capture the difference between the true and observed angular power spectra of the sky.

In the following, we evaluate both temperature and polarization beam window functions for the feedhorn I_0. The input sky map to our pipeline, including temperature and polarization anisotropies, has been produced with `CAMB`. Table 5.1 reports the set of cosmological parameters we have used for the calculation of the power spectra in Fig. 5.2.

Fig. 5.3 shows the beam window function for the I_0 main beams at 43 GHz. We can see that the shape of the function in temperature and polarization is due to the smoothing effect of the main beam angular resolution. To complete the analysis, Fig. 5.4 shows how the input power spectra is modified after the observation with the Strip optical system (there is no deconvolution of the beam window function).

Besides the effect of the optics on the CMB power spectrum, it would be of great interest to reconstruct the foregrounds power spectrum, since one of the goals of Strip is to map the synchrotron polarized emission. The knowledge of how the foreground measurement is affected by the window function is an invaluable information. However, the analysis reported in this chapter is only preliminary and we will not go further into it since the development of a new simulation pipeline completely devoted to the Strip instrument and not borrowed by other experiments is underway. Moreover, the effect

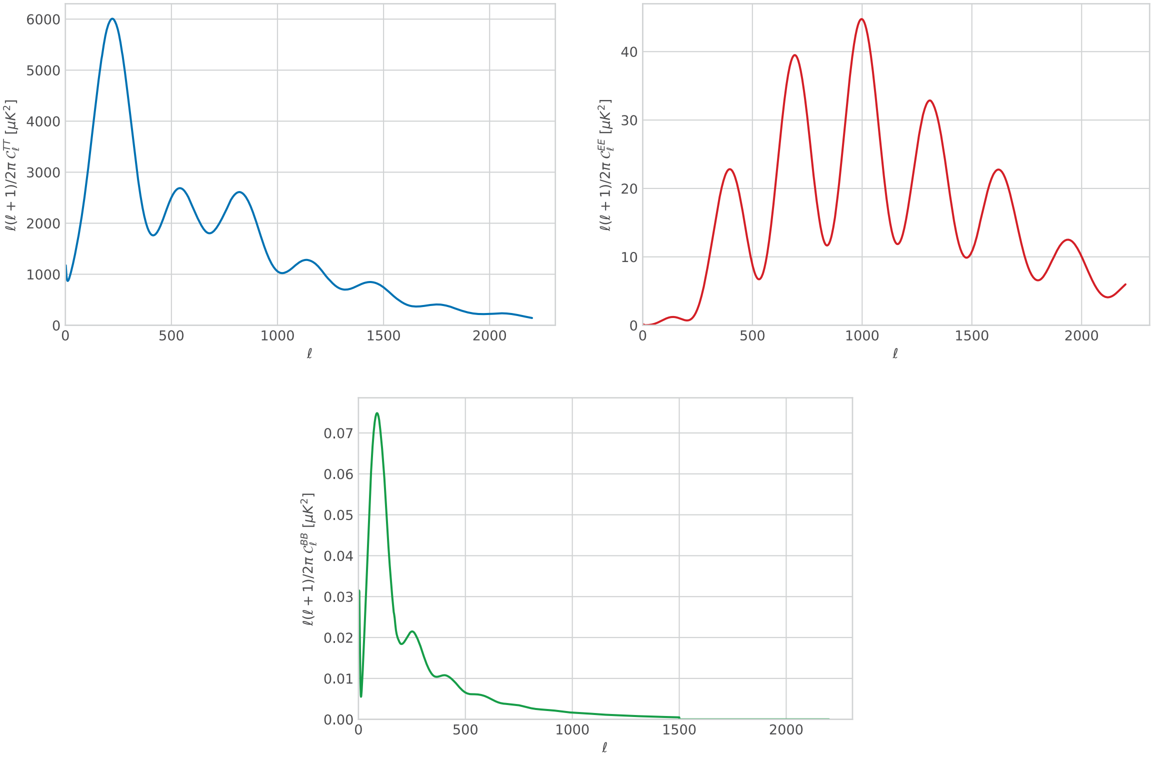

Figure 5.2: From left to right, C_ℓ^{TT}, C_ℓ^{EE} and C_ℓ^{BB} power spectra as computed by `CAMB` from the cosmological parameters in Table 5.1.

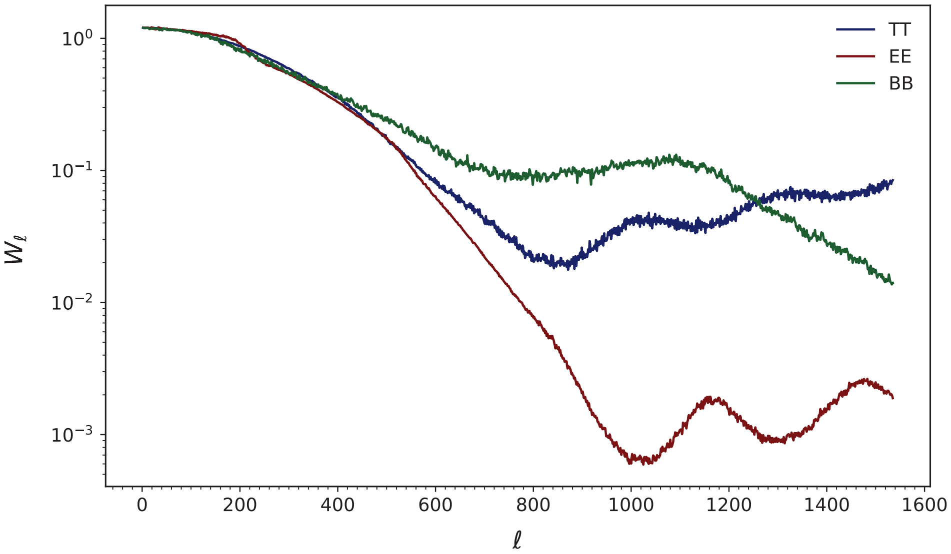

Figure 5.3: Beam window function for the I_0 beam at 43 GHz for the temperature (TT) and polarization (EE and BB).

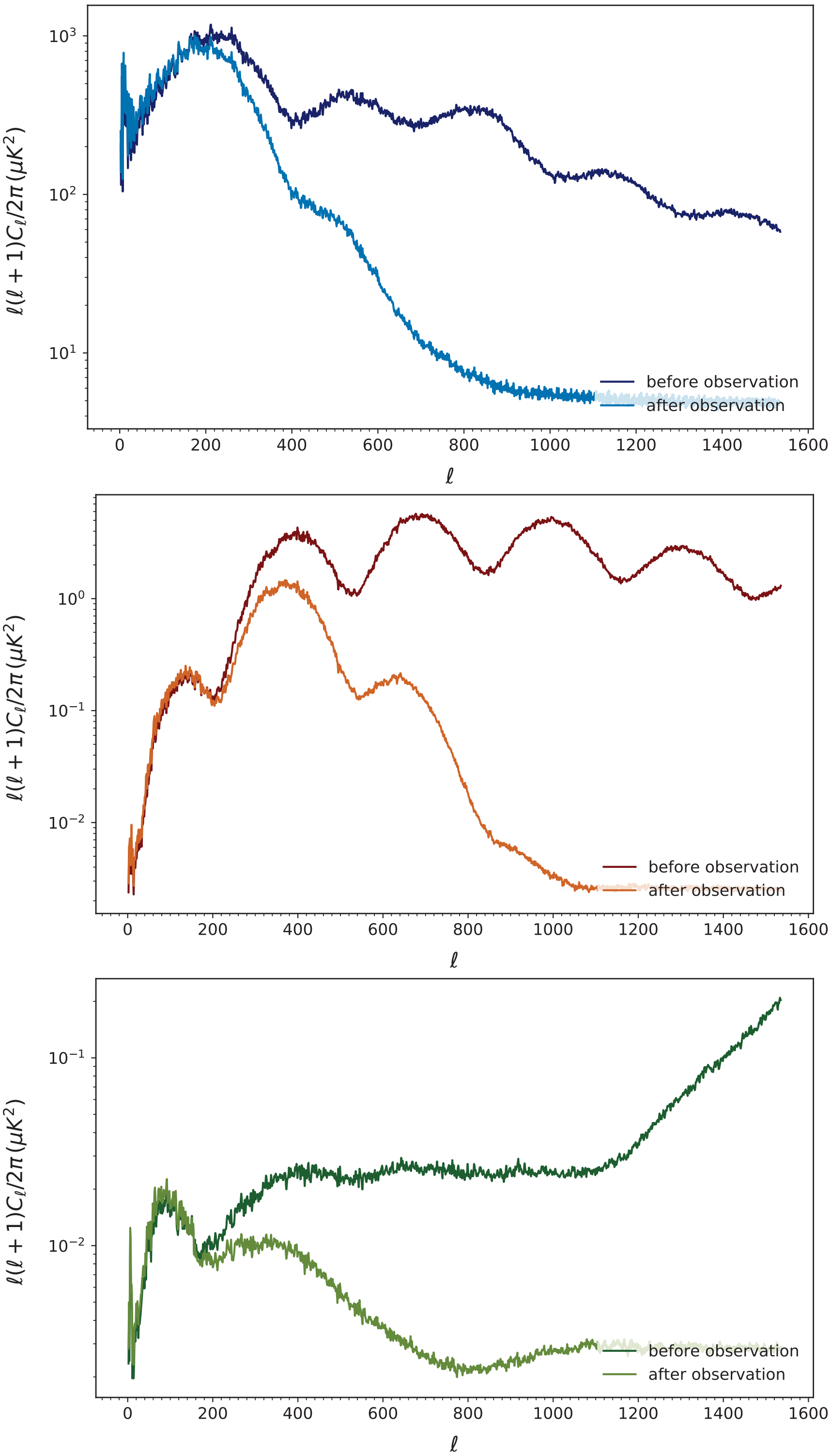

Figure 5.4: Comparison between the input power spectra (TT, EE and BB) and the spectra after the observation with the main beam feedhorn I_0. Notice that there is no deconvolution of the beam window function.

of the sidelobes should also be evaluated; however, it will be tricky to develop a tool for this analysis. In fact, for ground-based experiments, the sky map is combined with the Earth horizon and the result is that the observed map is continuously changing, so that we cannot perform a single convolution with the full-sky beam pattern. This is a specific problem for ground-based experiment which is still unsolved.

Conclusions and future perspectives

My thesis has been carried out in the context of the Strip instrument which is part of the LSPE experiment, a project with the aim to constrain the ratio between the amplitudes of tensor and scalar modes to ~ 0.03 at 99.7% confidence level and to study the polarized emission of the Milky Way. Strip is a coherent polarimeter array that will observe the microwave sky from the Teide Observatory in Tenerife in two frequency bands centred at 43 GHz (Q-band, 49 receivers) and 95 GHz (W-band, 6 receivers) through a dual-reflector crossed-Dragone telescope of 1.5 m projected aperture.

One of the major sources of systematic errors in CMB experiments is the non-ideal response of the optics. Main beam distortions and sidelobes may degrade the reconstruction of the power spectrum of the CMB anisotropies at high and low multipoles, respectively. For high precision CMB experiments the detailed knowledge of the telescope response is mandatory. While for the main beam regions Physical Optics gives accurate and well established results taking into account only the feedhorn and the telescope mirrors, for the sidelobe region also the surrounding structures should be considered. Robust optical simulations are also of primary importance in the understanding of the main beam response and the straylight rejection capability of the telescope, in particular in the far sidelobe region where the power levels are extremely low (but not negligible) and direct measurements become difficult and uncertain.

For this reason, the purposes of this thesis has been to develop a detailed electromagnetic model of Strip telescope using GRASP. This was mandatory to get a good characterization of the optical response and to address optical related systematic effects.

The model I have developed includes the feedhorns, the two mirrors, the shielding structure with a circular aperture, the IR filters and the cryostat window. I characterized the response of the optics both in the main beam and sidelobe region. The main beams analysis includes the effect of the IR filters and cryostat window, which have been modelled as lenses. I found that their effect is to reduce the full-width half-maximum of the nominal feedhorn radiation pattern. I studied also the effect of mirrors imperfections, modelled as random errors with a given rms and structured deviation described by means of Zernike polynomials expansion. I found that the effect of these imperfections on main beams parameters is lower than 1%, and thus they are negligible.

Then, I analysed the sidelobes of the telescope taking into account the presence of the comoving baffling structure, which significantly modifies the radiation pattern shape far from the telescope boresight. Using the Multi-Reflector Geometrical Theory of Diffraction method, I identified the sequences of reflections and diffractions which give a significant contribution to the sidelobes. In particular, I found that two contributions lead to a power level in the sidelobes that does not satisfy the requirements, even if marginally. Furthermore, I analysed the effect of the introduction of a forebaffle and an absorbing material inside the shielding structure.

To sum up, I have outlined the main characteristics and angular response of the Strip telescope so that now we have a first guess of its pros and cons. Moreover, simulations represent an invaluable tool for assessing the performance at system level. Systematic effects introduced by the Strip optics have been predicted with a preliminar study by means of optical simulations with GRASP and the LevelS pipeline, by taking into account for the optical response as combined to the instrument scanning strategy.

These last results call for the development of a more detailed analysis of the impact of optics on observations. In particular, the development of a data analysis pipeline devoted to the Strip instrument, which takes into account also the detector noise and the effect of the atmosphere, is already underway. This pipeline will be a real predictive tool and will be fundamental for the instrument data analysis.

Data obtained in this thesis will be useful for the data reduction pipeline. However, further improvements may be done depending on the on-going testing and integration activity. As an example, a deeper structural analysis which takes into account the telescope shielding structure will be soon available; hence, the effect on the main beam can be analysed again.

Besides the optical simulation activity, I also performed radiation pattern measurements of the six W-band feedhorn in the anechoic chamber of the Physics Department at the University of Milan. I compared all measurements to simulations in order to assess compliance to design requirements. I found that, even if there are some non-compliances in the measurement, the performance of the W-band horns is still good enough to use this channel for measurements of the Tenerife atmosphere.

In addition, I have been involved in a new project which uses the Strip optics as a reference case for the prediction of main beams parameters using neural networks. This project shows very promising preliminary results and it is explained in more detail in Appendix D.

Appendices

APPENDIX A

Optics concepts

A.1 Telescopes descriptive parameters

In order to describe an optical system, for example a two-mirror telescope, some terminology should be introduced, as well as the parameters which characterize the system.

For a single reflecting surface, the *focal length* is the distance over which initially parallel rays are brought to a focus. For a two-mirror telescope, we can define the equivalent focal length as a combination of the focal lengths of the two mirrors. For example, in the case of a two-mirror on-axis telescope the combined focal length f is found by using the following equation

$$\frac{1}{f} = \frac{1}{f_1}\left(1 + \frac{f_1}{f_2} - d\frac{1}{f_2}\right), \tag{A.1}$$

where f_1 and f_2 are the focal lengths of the two mirrors and d is the distance between the reflecting surfaces.

For a given optical system, the *focal surface* is a curved surface on which initially parallel rays come to a focus after passing through the optical system.

The *aperture stop* is an element of an optical system that determines the amount of light reaching the image. For most telescopes the primary mirror serves as the aperture stop. When we consider a bundle of parallel rays, we can refer to the *chief ray*, which is defined as the ray that passes through the centre of the aperture stop. The chief ray is representative of the bundle of rays.

Finally, we define another descriptive parameter used to describe an optical system: the f-number. The *f-number*, $F\#$ (or focal ratio), is the ratio of the focal length f to the diameter of the aperture D,

$$F/\# = \frac{f}{D}. \tag{A.2}$$

It is a dimensionless number which gives a quantitative measure of the system speed[1]. Note that rapid telescopes have small f-numbers. A smaller focal ratio means a wider field of view, hence it allows more light to reach the focal plane. At microwaves, small focal ratio means small feedhorn aperture, resulting in more compact focal plane units. Then, the more a telescope is rapid the more the feedhorn may be small in diameter. Moreover, a telescope with a small focal ratio is typically shorter and lighter than longer focal ratio telescopes.

---

[1] The f-number is sometimes spoken as the speed of the optical system since the photographic exposure time is proportional to the square of the f-number.

A.2 Elements of optics

A very powerful method in dealing with geometrical optics - the analysis of optical systems by tracing rays - is the Fermat's principle, also known as the principle of least time. Fermat's principle states that the actual path a ray follows is such that the time of travel between two fixed points has a stationary value with respect to small changes of that path. An equivalent statement of Fermat's principle is obtained by replacing the words "time of travel" with "optical path length". The term *optical path length* refers to the path length that the light wave travels in a given time. In vacuum the optical path length equals the geometrical path length.

Note that since Fermat's principle speaks only about the path and not the direction along it, a ray will trace the same route in both directions and this is true in all cases the rays travel a stationary optical path length in accord with the Fermat's principle. This is known as the *principle of reversibility*. Note that for antenna systems it can be reformulated saying that the ratio between the received and transmitted power is the same when the transmitter and the receiver in the antenna system are exchanged with each other. This is also known as the *reciprocity theorem* of antennas. Reciprocity implies that antenna properties when receiving and transmitting are the same, and specifically that an antenna's radiation and receiving patterns are identical.

A different way of looking at what a focusing system does is in terms of wavefronts. A wavefront is a surface on which every point has the same optical path distance from a point source of light. For an electromagnetic wave it can be defined also as the surface characterized by a constant phase. In a homogeneous medium this surface is a sphere whose center is the point object. In the same medium rays are radial lines directed outward, and at each point on a wavefront a ray is perpendicular to the wavefront[2].

A perfect system that satisfies Fermat's principle is therefore one that converts a plane wavefront to a spherical wavefront centred on the focus point. Conversely, if Fermat's principle is not satisfied for all rays over a large aperture, then the wavefront converging toward the image is no longer spherical and the image has aberrations.

Fermat's principle is concerned only with rays and ignores the wave nature of light. Due to the wave nature of light, no image is perfect in the sense that all light is brought to a single focus point of infinitesimal size. Since an optical system suffers from diffraction, the light will actually form a small disk surrounded by fainter rings, called diffraction rings. This is known as the Airy disk. The diffraction is caused by interference of light at the aperture of the telescope. In a perfect telescope (a telescope having no aberrations and no central obstruction), 84% of the light goes to the central Airy disk and 16% to the rings, and it is impossible for more light to go into the central disk.

This behaviour allows to introduce another telescopes descriptive parameter, which is the *angular resolution*. Due to diffraction, the angular resolution limit for a telescope is

$$\theta \simeq 1.22\,\frac{\lambda}{D}, \tag{A.3}$$

which is valid for a circular aperture uniformly illuminated.

---

[2] Notice that a ray is a line drawn in space corresponding to the direction of flow of radiant energy. It is a mathematical construct and not a physical entity. In a medium that is uniform (homogeneous), rays are straight, and if the medium behaves in the same manner in every direction (isotropic), the rays are perpendicular to the wavefronts.

A.2.1 Main beam and sidelobes

The *beam solid angle* $\Omega_{\rm A}$ of an antenna is given by

$$\Omega_{\rm A} = \int_{4\pi} P_n(\theta,\phi)\,{\rm d}\Omega = \int_0^{2\pi}\int_0^{\pi} P_n(\theta,\phi)\sin\theta\,{\rm d}\theta\,{\rm d}\phi, \tag{A.4}$$

where $P_n(\theta,\phi)$ is the *normalized radiation pattern*:

$$P_n(\theta,\phi) = \frac{P(\theta,\phi)}{P_{max}}, \tag{A.5}$$

and $P(\theta,\phi) = |\langle S\rangle|$, where S is the time average Poynting's flux transmitted by the antenna (or received, according to the reciprocity theorem).

For most antennas the normalized power pattern has considerably larger values for a certain range of both θ and ϕ than for the remaining part of the sphere. This range is called *main beam* or main lobe of the antenna:

$$\Omega_{\rm MB} = \int_{\text{main beam}} P_n(\theta,\phi)\,{\rm d}\Omega. \tag{A.6}$$

The remainder is called *sidelobes* or back lobes, as shown in Figure A.1.

Obviously the quality of an antenna as a direction measuring device depends on how well the power pattern is concentrated in the main beam. The received power that comes from the region outside the main beam is called *straylight* and it is one of the major source of systematic effects in CMB experiments.

A.2.2 Angular resolution and ellipticity of the main beam

Main beam aberrations degrade its angular resolution, which can be evaluated as the average Full-Width Half-Maximum (FWHM) of the distorted beam. It is calculated by taking the average value between the maximum and minimum of the FWHM of the distorted beam:

$$\text{FWHM} = \frac{\text{FWHM}_{min} + \text{FWHM}_{max}}{2}. \tag{A.7}$$

Given this asymmetry in the width of a real beam (i.e. a non perfectly Gaussian beam), it is natural to introduce a parameter that quantifies the beam *ellipticity* e:

$$e = \frac{\text{FWHM}_{max}}{\text{FWHM}_{min}}. \tag{A.8}$$

Usually ellipticity is given at the half power level, i.e. at -3 dB from the main beam peak, but it can be evaluated at lower power levels (typically at -6 dB, -10 dB and -20 dB), where the increasing asymmetries contribution strongly impacts on the ellipticity value.

A.2.3 Directivity

The *directivity* of an antenna quantifies the capability of the antenna to concentrate radiation within a solid angle in a particular direction. It can be defined as the ratio of the radiation intensity in a given direction from the antenna to the radiation intensity averaged over all directions. The average radiation intensity is equal to the total power

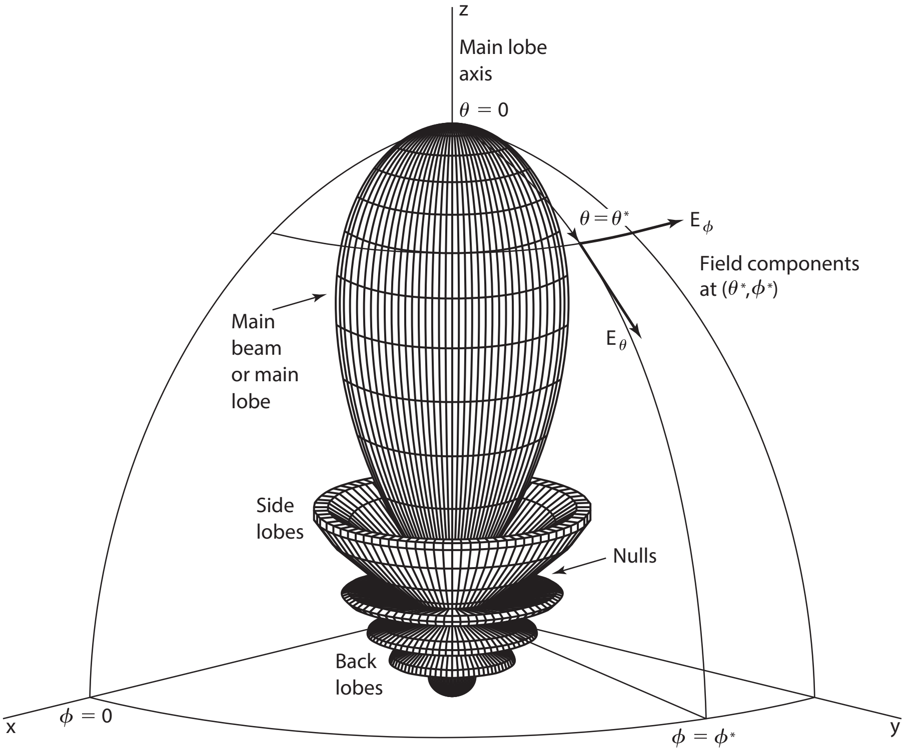

Figure A.1: Three-dimensional field pattern of a directional antenna with maximum radiation in z-direction at $\theta = 0$. Most of the radiation is contained in the main beam accompanied by radiation also in minor lobes (side and back). Between the lobes are nulls where the field goes to zero. The radiation in any direction is specified by the angles θ and ϕ (Kraus & Marhefka 2001).

radiated by the antenna divided by 4π. If the direction is not specified, the direction of maximum radiation intensity is implied:

$$\mathcal{D} = \frac{P(\theta,\phi)_{max}}{P(\theta,\phi)_{av}} = \frac{4\pi P(\theta,\phi)_{max}}{\int P(\theta,\phi)\,\mathrm{d}\Omega} = \frac{4\pi}{\int P_n(\theta,\phi)\,\mathrm{d}\Omega}, \tag{A.9}$$

where $P_n(\theta,\phi)$ is the normalized radiation pattern. The smaller the beam solid angle, the larger the directivity $\mathcal{D}$. Usually directivity is measured in dBi (i.e. decibels referenced to an isotropic radiator).

A.2.4 Cross polar discrimination factor

The cross polar discrimination factor (XPD, usually expressed in dB) has been computed as the ratio between the maximum directivity of the co– and cross– polar components:

$$XPD = 10 \cdot \log \frac{\mathcal{D}_{cp}}{\mathcal{D}_{xp}}, \tag{A.10}$$

where D_{cp} and D_{cx} are expressed as linear quantities. If the logarithmic scale is used, XPD is the difference between maximum co-polar and cross-polar components within the beam.

A.2.5 Depolarization parameter

Similarly to XPD, the depolarization parameter (d) gives an indication of the degree of polarization purity of an antenna. It is obtained computing the Stokes parameters in each point of the regular uv– grid (Kraus 1984):

$$\begin{aligned} S_I(u,v) &= E_{cp}(u,v)^2 + E_{xp}(u,v)^2 && \text{(A.11)}\\ S_Q(u,v) &= E_{cp}(u,v)^2 - E_{xp}(u,v)^2 && \text{(A.12)}\\ S_U(u,v) &= 2\cdot E_{cp}(u,v)\cdot E_{xp}(u,v)\cdot \cos[\delta\phi(u,v)] && \text{(A.13)}\\ S_V(u,v) &= 2\cdot E_{cp}(u,v)\cdot E_{xp}(u,v)\cdot \sin[\delta\phi(u,v)] && \text{(A.14)} \end{aligned}$$

in which E$_{cp}$ and E$_{xp}$ are the amplitude field of the co– polar and cross– polar components, respectively, and $\delta\phi$ is the phase difference between the co– polar and cross– polar fields. Then, over the whole uv– plane computed, each parameter has been summed as

$$S_N = \sum_{(u,v)} S_N(u,v)\cdot \Delta u \Delta v, \qquad \text{where N=I,Q,U,V} \tag{A.15}$$

and, finally we obtain

$$d(\%) = \left(1 - \frac{\sqrt{(S_Q^2 + S_U^2 + S_V^2)}}{S_I}\right)\cdot 100. \tag{A.16}$$

A.2.6 Rotation angle

The rotation angle of the polarisation ellipse (τ, which ranges from –90° to 90°, as shown in Figure A.2) is computed as in (Kraus 1984):

$$\begin{aligned} \tau(u,v) &= \frac{1}{2}\cdot \arctan\left(\frac{2\cdot E_{cp}(u,v)\cdot E_{xp}(u,v)\cdot \cos[\delta\phi(u,v)]}{E_{cp}(u,v)^2 - E_{xp}(u,v)^2}\right)\\ &= \frac{1}{2}\cdot \arctan\left(\frac{S_U(u,v)}{S_Q(u,v)}\right). \end{aligned} \tag{A.17}$$

The resulting uv-grid gives an indication of the discrepancy from the preferred polarization of the main beam, in the (u,v) extents.

A.2.7 Spillover

Through a simple ray-tracing the spillover can be evaluated quickly for each feedhorn model, taking into account the radiation pattern of the feedhorn and the geometry of the optical system. This is a first approximation to the real spillover since it takes into account only the rays reflected by the sub-reflector that do not hit the main reflector.

The spillover has been computed as $1 - W$, where W is the relative power hitting the main reflector. The power contained in the incident field on the main reflector is computed by integrating Poynting's vector over the surface. The Poynting vector is

$$\vec{P} = \frac{1}{2}\Re(\vec{E}\times\vec{H}^*), \tag{A.18}$$

where $\Re$ denotes the real part and * the complex conjugate. The power ΔW hitting a surface element with area Δs becomes:

$$\Delta W = -\overline{P}\cdot\hat{n}\Delta s, \tag{A.19}$$

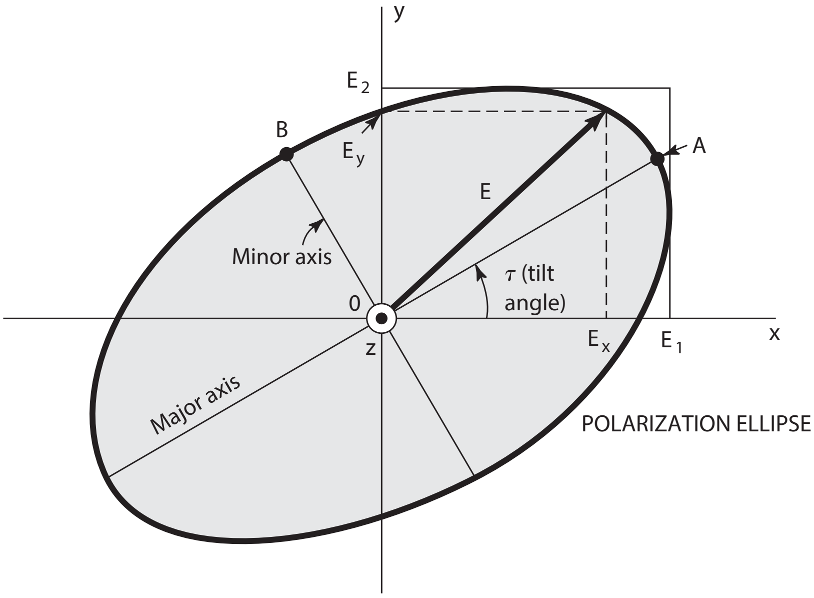

Figure A.2: Polarization ellipse at tilt angle τ showing instantaneous components E_x and E_y and amplitudes (or peak values) E_1 and E_2 (Kraus & Marhefka 2001).

where $\overline{P}$ is the Poynting's vector of the incident field and $\hat{n}$ is the normal unit surface pointing towards the illuminated side of the surface. The total power W on the surface becomes

$$W = -\int\int_S \overline{P}(\overline{r}') \cdot \hat{n}(\overline{r}')ds', \tag{A.20}$$

which is a surface integral with the integration variable $(\overline{r}')$.

APPENDIX B

GRASP simulation software

GRASP is a commercial software tool for design and analysis of reflector antennas, which can calculate the electromagnetic radiation produced by systems consisting of multiple reflectors with several feedhorns. The software is object-oriented, hence all reflector surfaces and feedhorn systems are described in terms of objects belonging to different classes. The input objects to be built by the user belongs to the following classes: Geometrical Objects, which describe geometrical entities (reflector, coordinate systems), or Electrical Objects, which describe electrical entities (frequencies, wavelengths, feedhorns).

All structural elements in GRASP are specified in a coordinate system, which defines the position and orientation of the element. Coordinate systems can be specified relative to any other coordinate system or to the *global coordinate system*. The global coordinate system is an inherent coordinate system with origin at (0,0,0) and unit vectors (1,0,0), (0,1,0) and (0,0,1).

Feedhorns belong to the electrical objects class and they are characterised by their radiation pattern. The most general way to specify a feedhorn is by means of its tabulated pattern.

A reflector is defined by means of a reflector surface and a reflector rim. Both of these two items are specified in the same coordinate system. Available shapes are ellipsoid, hyperboloids, paraboloids and plates. Otherwise, the z-values of the surface can be given at the nodes of a regular grid in x and y.

B.1 Coordinate systems

All structural elements in GRASP are specified in a coordinate system, which defines the position and orientation of the element. The origin of a new coordinate system is given by the x-, y- and z-value in the reference coordinate system. The orientation of the new coordinate system is defined by two orthogonal vectors along any two of the three coordinate vectors. An alternative option is to specify the three angles θ, ϕ and ψ in a spherical coordinate system (see Fig. B.1).

The new coordinate system is $x_1y_1z_1$ specified in the reference coordinate system xyz. First, the z-axis is tilted at the angle θ by rotating the xyz-coordinate system around the line in the xy-plane orthogonal to the line making the angle ϕ with the x-axis. This process generates the coordinate system $x'y'z'$. The $x_1y_1z_1$-coordinate system is then obtained by rotating the angle ψ around the z'-axis. The orientation definition described here is useful for specifying the direction of a feed. The first two coordinates, θ and ϕ, describe the pointing of the feed and the ψ-value controls the polarisation direction.

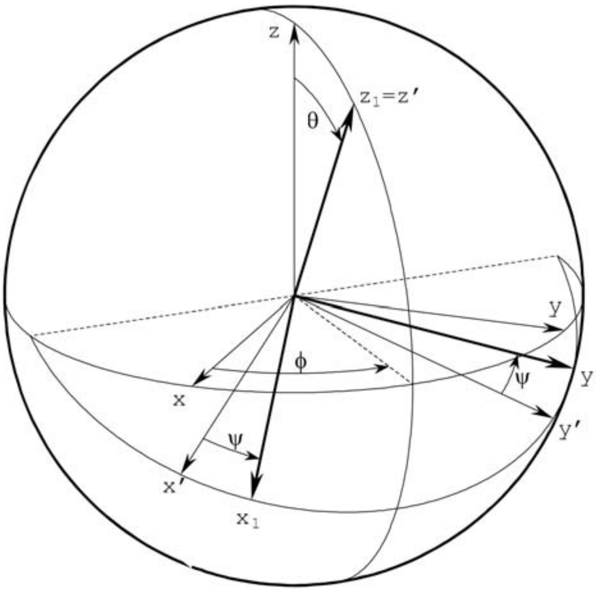

Figure B.1: Orientation of the new coordinate system $x_1y_1z_1$ relative to xyz specified by the angles θ, ϕ and ψ.

The unit vectors of the rotated coordinate systems are given by

$$\begin{aligned}
\hat{x}_1 &= \hat{\theta}\cos(\phi-\psi) - \hat{\phi}\sin(\phi-\psi),\\
\hat{y}_1 &= \hat{\theta}\sin(\phi-\psi) - \hat{\phi}\cos(\phi-\psi),\\
\hat{z}_1 &= \hat{r},
\end{aligned} \tag{B.1}$$

where

$$\begin{aligned}
\hat{\theta} &= \hat{x}\cos(\theta)\cos(\phi) + \hat{y}\cos(\theta)\sin(\phi) - \hat{z}\sin(\theta),\\
\hat{\phi} &= -\hat{x}\sin(\phi) + \hat{y}\cos(\phi),\\
\hat{r} &= \hat{x}\sin(\theta)\cos(\phi) + \hat{y}\sin(\theta)\sin(\phi) + \hat{z}\cos(\theta).
\end{aligned} \tag{B.2}$$

B.2 Analysis methods

The most fundamental analysis methods used in GRASP are the Physical Optics (PO) and the ray techniques given by Geometrical Optics (GO). The analysis can be considered as a three step procedure where the first step is to calculate the induced or equivalent surface currents, the second step is to calculate the field radiated by these currents and the third step is to add the incident and the scattered field to obtain the total field. Physical Optics is a method that gives an approximation to the surface currents valid for perfectly conducting scatterers. In the physical optics approximation it is assumed that the surface current in a specific point on a curved, but perfectly conducting scatterer is the same as the surface current on an infinite planar surface which is tangent to the scattering surface at this point. The induced currents are given by $\vec{J}^e = 2\hat{n}\times\vec{H}^{inc}$, which constitutes the physical optics approximation. Here $\vec{J}^e$ is the induced electric current, $\hat{n}$ is the unit surface normal (pointing outward on the illuminated side of the surface) and $\vec{H}^{inc}$ is the incident magnetic field. The Physical Optics integration grid is specified by the two variables $po1$ and $po2$. The values of these variables can either be determined automatically by GRASP or they can be set to suitable values by the user. Too small values of $po1$ and $po2$ will result in inaccurate fields since the PO integral has not converged, and large values, on the other hand, will take more computation time than necessary. When considering complex optical systems, for which a PO simulation requires an excessive computational time, the MUlti-GTD method can be used. This method applies the ray-tracing technique to compute the reflected and diffracted fields.

The physical quantities computed by GRASP are the electric field $\vec{E}$, the magnetic field $\vec{H}$, the surface electric current $\vec{J}_e$ and the surface magnetic current $\vec{J}_m$. The electric and magnetic fields in GRASP are measured in normalised units. The relation between the fields in the standard SI units and the units in GRASP is given by

$$\vec{E} = \frac{1}{k\sqrt{2\zeta}}\,\vec{E}_{\mathrm{SI}}, \tag{B.3}$$

$$\vec{H} = \frac{1}{k}\sqrt{\frac{\zeta}{2}}\,\vec{H}_{\mathrm{SI}}, \tag{B.4}$$

$$\vec{J}^{e} = \frac{1}{k}\sqrt{\frac{\zeta}{2}}\,\vec{J}^{e}_{\mathrm{SI}}, \tag{B.5}$$

$$\vec{J}^{m} = \frac{1}{k\sqrt{2\zeta}}\,\vec{J}^{m}_{\mathrm{SI}}. \tag{B.6}$$

The power flux per unit area of a propagating electromagnetic wave is given by Poynting's vector

$$\vec{P} = k^2\,\Re(\vec{E}\times\vec{H}^*), \tag{B.7}$$

where $\Re$ denotes the real part and * the complex conjugate.

The far field is defined as the limit

$$\begin{cases} \vec{E}_{far} = \lim\limits_{r\to\infty}\left(\vec{E}\,k\,r\,e^{ikr}\right) \\ \vec{H}_{far} = \lim\limits_{r\to\infty}\left(\vec{H}\,k\,r\,e^{ikr}\right) \end{cases} \tag{B.8}$$

where *r* is the distance from the origin of the coordinate system in which the fields $\vec{E}$ and $\vec{H}$ are calculated. The near field is a function of the location of the field point specified by three space coordinates, such as (x, y, z) or (r, θ, ϕ). The far field is a function of direction and can thus be specified by two coordinates, for example (θ, ϕ). In an observation point far away from the antenna the power flux per unit area reduces to

$$\vec{P} = k^2\,|\vec{E}|\,\hat{r} = k^2\,|\vec{H}|\,\hat{r}, \tag{B.9}$$

because of the plane wave relations

$$\begin{cases} \vec{E}_{far} = \vec{H}_{far}\times\hat{r} \\ \vec{H}_{far} = \hat{r}\times\vec{E}_{far} \end{cases} \tag{B.10}$$

A suppressed time factor $e^{i\omega t}$ is assumed for all GRASP outputs, where $\omega = 2\pi\nu$.

The optical system response is schematically based on three steps: first, the radiated field coming from the feedhorn is propagated until it reaches the reflector. Then the induced surface currents on the reflector surface are computed; second, the radiated field caused by the currents is computed; finally, the incident and reflected fields are summed up to obtain the total field. The total field can be computed as $\vec{E} = \vec{E}^i + \vec{E}^s$, where $\vec{E}^i$ is the incident electric field and $\vec{E}^s$ is the reflected field.

B.3 GRASP output plots

The two most common options to show the location of the output points in GRASP are the one-dimensional cuts and the two-dimensional field grids as presented in the following paragraphs. The output points are specified relative to a user-defined coordinate system.

B.3.1 One-dimensional cut

The one-dimensional cut shows the field power as a function of the angle θ, while ϕ is fixed. Three types of pattern cuts are available: spherical cuts, cylindrical cuts and planar cuts. A schematic representation of the spherical pattern cut can be seen in figure B.2. The spherical pattern cuts can be used for far field as well as near field points, whereas the cylindrical and the planar pattern cuts are only available for near field points.

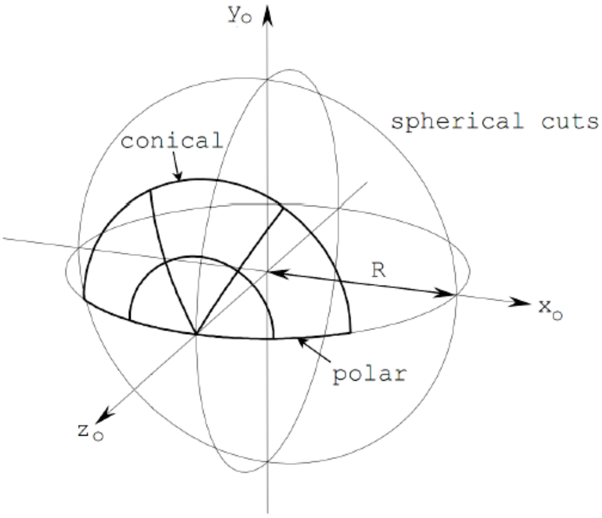

Figure B.2: Scheme of a spherical pattern cut.

B.3.2 Two-dimensional grid

The grid gives a two-dimensional view of the computed field power. The 2D grids are available in three forms: spherical for both near-field and far field points and cylindrical and planar for near field points only. For the spherical grids various types of output coordinates are available, but the most common is the uv-grid, which is illustrated in figure B.3. The grids are specified by the minimum and maximum value and the number of points for each of the two grid coordinates. The uv-coordinates are related to the spherical coordinates θ and ϕ by

$$\begin{aligned} u &= \sin\theta\cos\phi \\ v &= \sin\theta\sin\phi \end{aligned} \tag{B.11}$$

and the unit vector to the field point at (u, v) is given by

$$\hat{r} = (u, v, \sqrt{1 - u^2 - v^2}). \tag{B.12}$$

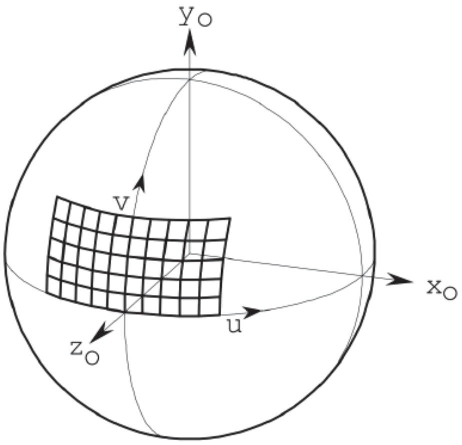

Figure B.3: Spherical two-dimensional output grids in the uv coordinates.

B.3.3 Two-dimensional surface grid

This type of grid is useful when we need to calculate the field directly at the surface of a scatterer. The field quantity on the surface can be the incident electric field, the reflected electric field, the incident magnetic field, the reflected magnetic field or the PO currents. The calculated field vectors at points on the surface of the scatterer will be resolved in components according to the axes of the coordinate system defined by the user (for a schematic representation see figure B.4). The surface points can be specified as a two-dimensional grid in x and y of the coordinate system of the scatterer.

B.4 Cross-polarization definition

For an experiment whose aim is to measure the CMB polarization it is important to reduce the spurious contribution to the incoming polarized signal introduced by the optical system. This contribution is known as *cross-polarization*.

It is a surprising fact that there is not a universally accepted definition of cross-polarization at the present, and at least three different definitions have been used in literature. The IEEE (Institute of Electrical and Electronics Engineer) standard definition is "the polarization orthogonal to a reference polarization" (IEEE Std 145-2013). For circular polarization this is adequate, but for linear polarization the direction of the reference polarization must be defined.

In the linear polarization case we can give various definitions; however, in GRASP, linear polarisation is calculated according to the so-called *Ludwig's 3rd definition* (Ludwig 1973).

B.4.1 Ludwig's 3rd definition of polarization

In 1973 Arthur C. Ludwig introduced a definition of co- and cross-polarization which is uniform on the forward hemisphere of a radiation pattern. This definition is widely used for directive antennas as it gives a well defined description of the polarization of the antenna pattern from the main beam direction to far out in the sidelobes. The polarization definition in the backward direction has, however, an unexpected behaviour, which becomes important when the backward radiation of the feedhorn in a reflector

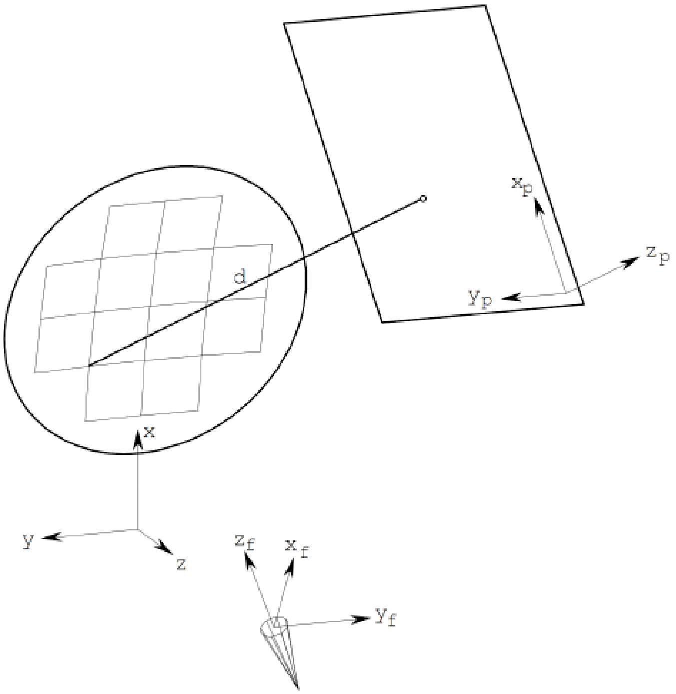

Figure B.4: Offset reflector with two-dimensional surface grid points.

antenna is considered. We are considering a directive antenna radiating in the direction of the positive z-axis as in figure B.5.
Usually any polarization definition has a pole in which the polarization is not defined. Ludwig's 3rd definition has only one pole, which is in the back hemisphere at $\theta = 180°$.

The near fields and far fields are treated separately because a near field has three vector components, whereas a far field can be completely characterised by two transverse components. A far field has no radial component and may be decomposed along any two polarisation vectors $\hat{e}_1$ and $\hat{e}_2$ which are mutually orthogonal and also orthogonal to the far field direction r,

$$\vec{E}_{\text{far}} = E_1\hat{e}_1 + E_2\hat{e}_2. \tag{B.13}$$

The two polarisation vectors $\hat{e}_1$ and $\hat{e}_2$ are functions of the far field direction (θ, ϕ). The polarisation components can be calculated as

$$E_1 = \vec{E}_{\text{far}} \cdot \hat{e}_1^*, \qquad E_2 = \vec{E}_{\text{far}} \cdot \hat{e}_2^*. \tag{B.14}$$

The polarisation components are related to the directivity of the antenna by

$$directivity = |E_1|^2 + |E_2|^2. \tag{B.15}$$

GRASP has different options for the definition of $\hat{e}_1$ and $\hat{e}_2$. All vectors are referred to the coordinate system in which the field is computed.

The most basic far-field polarisation, the $\theta\phi$ polarisation, is based on the spherical coordinates θ and ϕ with the polarisation components defined by

$$\vec{E}_{\text{far}} = E_\theta\hat{\theta} + E_\phi\hat{\phi}, \tag{B.16}$$

where $\hat{\theta}$ and $\hat{\phi}$ are the spherical unit vectors

$$\begin{aligned} \hat{\theta} =& \hat{x}\cos\theta\cos\phi + \hat{y}\cos\theta\sin\phi - \hat{z}\sin\theta \\ \hat{\phi} =& -\hat{x}\sin\phi + \hat{y}\cos\phi, \end{aligned} \tag{B.17}$$

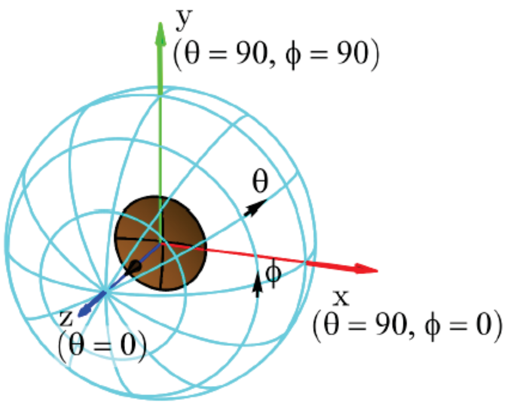

Figure B.5: A directive antenna radiating in the direction $\theta = 0^\circ$. A spherical $\theta\phi$-grid surrounds the antenna.

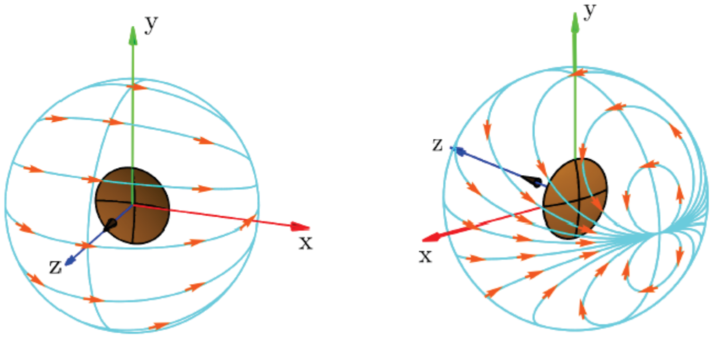

Figure B.6: The orientation of $\hat{e}_{co}$ over the front (left) and back (right) hemisphere.

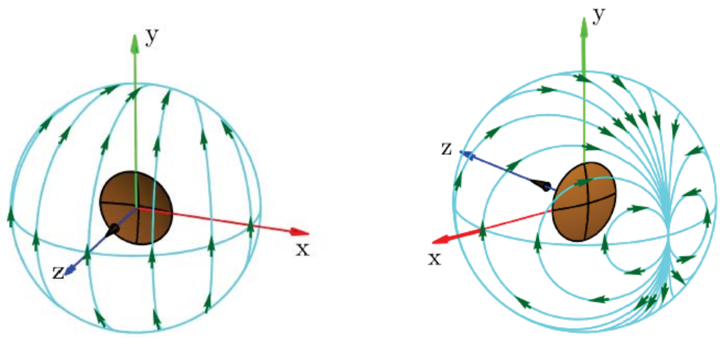

Figure B.7: The orientation of $\hat{e}_{cx}$ over the front (left) and back (right) hemisphere.

with $0^\circ \leq \theta \leq 180^\circ$ and $0^\circ \leq \phi \leq 360^\circ$. These components are discontinuous through the point $\theta = 0^\circ$ and $\theta = 180^\circ$. The co- and cross-polar unit vector according to Ludwig's 3rd definition are

$$\begin{aligned} \hat{e}_{co} =& \hat{\theta} \cos\phi - \hat{\phi} \sin\phi \\ \hat{e}_{cx} =& \hat{\theta} \sin\phi + \hat{\phi} \cos\phi \end{aligned} \tag{B.18}$$

therefore, we can write $\vec{E}_{\text{far}} = E_{co}\hat{e}_{co} + E_{cx}\hat{e}_{cx}$. The unit vectors in Eq. (B.18) are continuous at $\theta = 0^\circ$ and the only pole is located at $\theta = 180^\circ$. Figures B.6 and B.7 show the direction of the co-polar $\hat{e}_{co}$ and cross-polar $\hat{e}_{cx}$ unit vectors on a sphere surrounding the antenna.

APPENDIX C

Zernike polynomials

Zernike polynomials are a special set of orthonormal functions, continuous and orthogonal over a unit circle, which are widely used in representing the aberrations of optical systems. These optical aberrations can be a result of optical imperfections in the individual elements of an optical system and/or the system as a whole.

Using the normalized Zernike expansion to describe aberrations offers the advantage that the coefficient of each mode represents the root mean square (RMS) wavefront error attributable to that mode. The Zernike coefficients used to mathematically describe a wavefront are independent of the number of polynomials used in the sequence. This condition of independence or orthogonality, means that any number of additional terms can be added without impact on those already computed.

The Zernike polynomials expressed in polar coordinates ($x = \rho \sin\phi$, $x = \rho\cos\phi$) are given by

$$\begin{aligned} Z_n^m(\rho,\phi) &= R_n^m(\rho)\cos(m\phi) \qquad \text{for}\, m \geq 0, \\ Z_n^{-m}(\rho,\phi) &= R_n^m(\rho)\sin(m\phi) \qquad \text{for}\, m < 0, \end{aligned} \tag{C.1}$$

where ρ is restricted to the unit circle ($0 \leq \rho \leq 1$) and ϕ is measured clockwise from the y-axis. This is consistent with aberration theory definitions, but different from the conventional mathematical definition of polar coordinates. The normalization has been chosen to satisfy $R_n^{\pm m}(1) = 1$ for all values of n and m.

Occasionally a single indexing scheme is used for describing the Zernike expansion coefficients. Since the polynomials depend upon two parameters n and m, ordering of a single indexing scheme is arbitrary. To obtain the single index j, we can use the OSA/ANSI standard

$$Z_j(\rho,\phi) = Z_n^m(\rho,\phi), \qquad \text{where} \quad j = \frac{n(n+2)+m}{2}.$$

The results provided by BCV s.r.l., which have been used for the optical analysis in Sect. 3.6, adopt the standard definition listed in Table C.1 and represented in Fig C.1. The modes $m = n = 1$ and $m = 0$, $n = 2$ represent a tilt and an axial defocusing, respectively. The modes for which $m + n = 4$ are the primary aberrations in optical systems.

	j	Z_j	Name
Z_0^0	0	1	Piston
Z_1^{-1}	1	$\rho \sin \phi$	Tilt
Z_1^1	2	$\rho \cos \phi$	Tip
Z_2^{-2}	3	$\rho^2 \sin 2\phi$	Oblique astigmatism
Z_2^0	4	$2\rho^2 - 1$	Defocus
Z_2^2	5	$\rho^2 \cos 2\phi$	Vertical astigmatism
Z_3^{-3}	6	$\rho^3 \sin 3\phi$	Vertical trefoil
Z_3^{-1}	7	$(3\rho^3 - 2\rho) \sin \phi$	Vertical coma
Z_3^1	8	$(3\rho^3 - 2\rho) \sin \phi$	Horizontal coma
Z_3^3	9	$\rho^3 \cos 3\phi$	Oblique trefoil

Table C.1: Table of the radial polynomials $R_n^m(\rho)$ for $m \leq 3$ and $n \leq 3$ (Born & Wolf 1999).

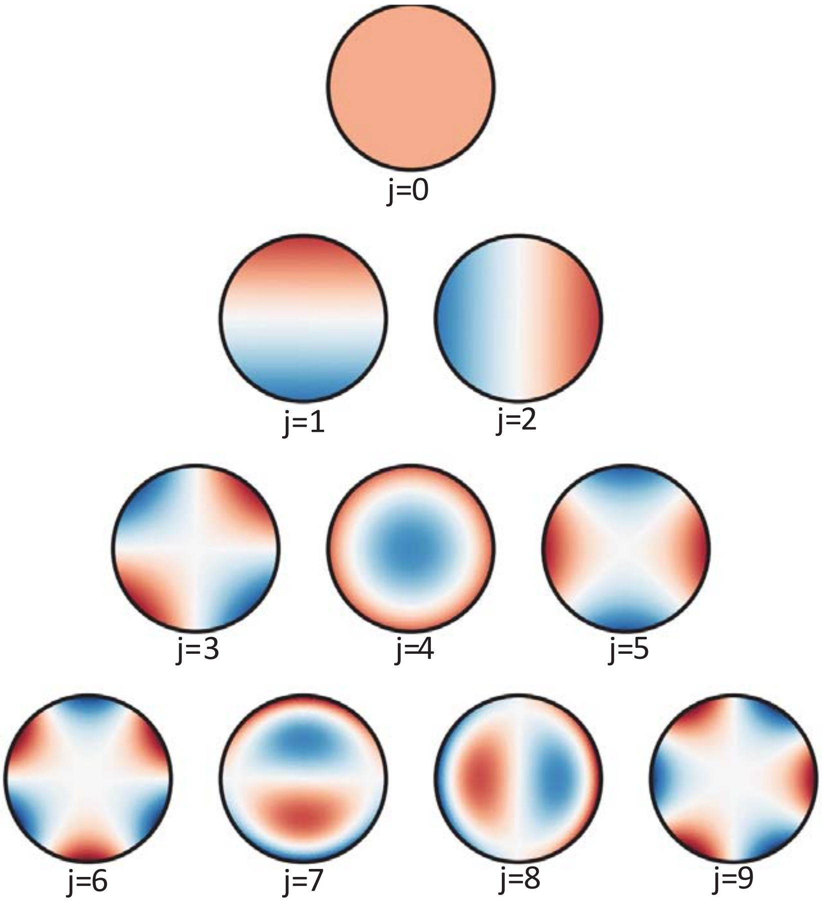

Figure C.1: The first 10 Zernike polynomials, ordered vertically by radial degree n and horizontally by azimuthal degree m.

APPENDIX D

Machine learning applications

During the last year of my PhD, I have been involved in a project for the study of possible applications of machine learning techniques for the prediction of the main beam parameters of an optical system. If applicable, this would be useful in the case of densely populated focal planes, for which is not feasible an accurate simulation for each receiving antenna.

Deep learning consists of building a system that can transform data from one representation to another and this transformation is driven by extracting commonalities from a series of examples that demonstrate the desired mapping. If we consider a dataset $A = (x_0, y_0), \ldots (x_N, y_N)$, where x_0 is the input and y_0 is the desired output, we should find a model that takes x (input domain) and predicts the output. Simple regression problems require a linear model, but we can generalize to non-linear models which can fit whatever function.

At the core of deep learning are neural networks, mathematical entities capable of representing complicated functions through a composition of simpler functions. The basic building block of these functions is the neuron, which is a linear transformation of the input followed by the application of a non-linear function called activation function. An example of neuron is the expression

$$o = f(wx + b), \tag{D.1}$$

where x is the input, o is the output, f is the non-linear activation function, w and b are the learned parameters (called weight and bias). If we consider multidimensional weights and biases, we can talk about a layer of neurons.

We should define a way to check the model performance, i.e. measure the difference with the desired output. This can be done with a cost or loss function. To optimize the parameters of the model, the change in the error following a unit change in weights is computed by using the chain rule for the derivative of a composite function (backward pass). Then the value of the weights is updated in the direction that leads to a decrease in the error. The procedure is repeated until the error falls below an acceptable level.

As a first analysis of the usefulness of neural network in the context of the prediction of main beams parameters, we compared the performance of the neural network with a simple interpolation. The reference case we used is the optical system of the Strip instrument, which has a high number of detectors but a simulation of each of them is still feasible. From the results reported in Chapter 3, we know the parameters of each main beam.

For testing interpolation performance, we can define two subsets: one will be used for the interpolation and the other to check the results. On the other hand, when we build the neural network, the dataset is divided into three subsets for training, validation and

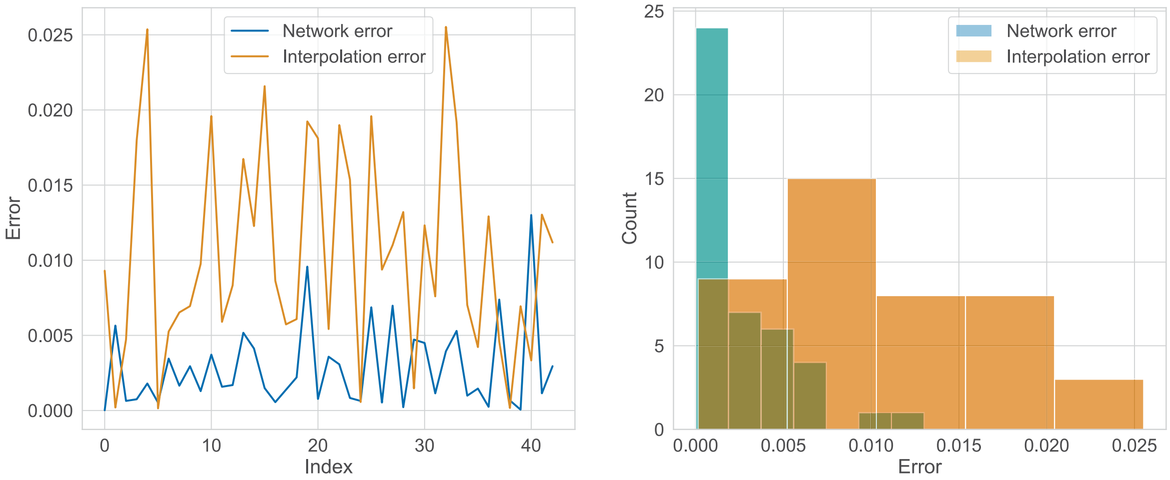

Figure D.1: Comparison of the error, i.e. the difference between true and predicted values, in the case of interpolation (orange) and neural network (blue). The architecture used has two hidden layers and the hyperbolic tangent as activation function.

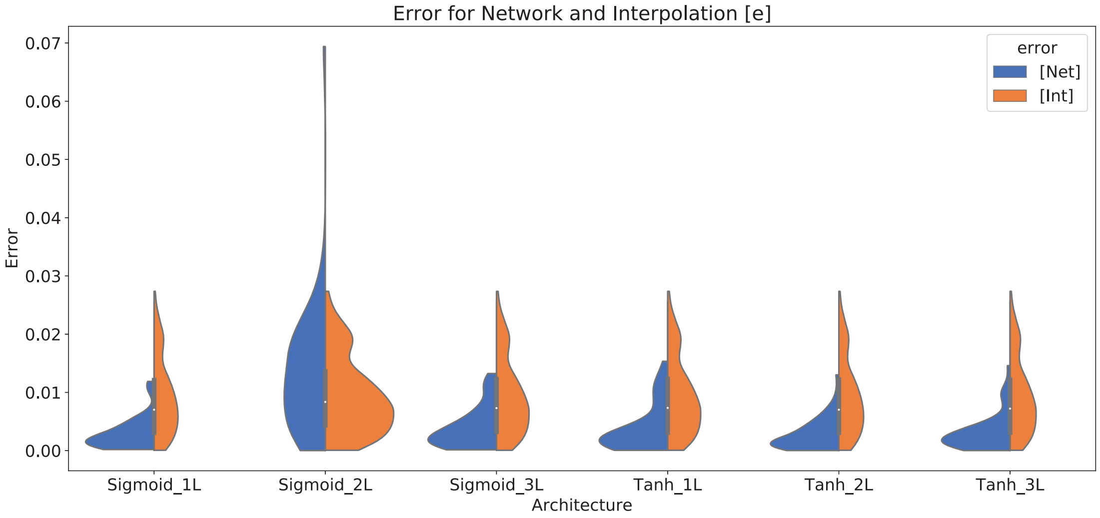

Figure D.2: Violin plot for the ellipticity obtained with different neural network architectures.

verification. We considered six different types of neural network architectures obtained changing the number of neurons, hidden layers or activation function.

Here we report the results obtained for the analysis of the beam ellipticity. Fig. D.1 shows the error between the true value and the predicted one for the interpolation and neural network cases.

The violin plot reported in Fig. D.2 shows the the probability density of the data at different values of the error. This representation is useful to compare the variables distribution. In our case, the more the distribution is peaked towards zero, the more the result is good. Therefore, we can see that the use of a neural network represents an improvement with respect to the simple interpolation.

This first analysis is showing very promising results, but the analysis is only at an early stage. A future development will be the application of these architectures to focal planes with different shapes, for example the one of the Planck telescope, to check whether the performance of the network is influenced by the peculiar shape of the Strip focal surface, which is extremely flat and symmetric.

Bibliography

Ade, P., Aguirre, J., Ahmed, Z., et al. 2019, Journal of Cosmology and Astroparticle Physics, 2019, 056

Ade, P. A. R., Ahmed, Z., Aikin, R. W., et al. 2016, Phys. Rev. Lett., 116, 031302

Alpher, R. A. & Herman, R. 1948, *Nature*, 162, 774

Baumann, D. 2009, arXiv e-prints, arXiv:0907.5424

Bennett, C. L., Halpern, M., Hinshaw, G., et al. 2003, *Astrophys. J. Suppl.*, 148, 1

BICEP2 Collaboration, Keck Array Collaboration, Ade, P. A. R., et al. 2018, *Phys. Rev. Lett.*, 121, 221301

Bischoff, C., Brizius, A., Buder, I., et al. 2013, *Astrophys. J.*, 768, 9

Born, M. & Wolf, E. 1999, Principles of optics : electromagnetic theory of propagation, interference, and diffraction of light

Carlstrom, J. E., Ade, P. A. R., Aird, K. A., et al. 2011, *Publ. Astron. Soc. Pac.*, 123, 568

Chen, Y.-L., Chiueh, T., & Teng, H.-F. 2014, *Astrophys. J. Suppl.*, 211, 11

Cleary, K. A. 2010, in Millimeter, Submillimeter, and Far-Infrared Detectors and Instrumentation for Astronomy V, ed. W. S. Holland & J. Zmuidzinas, Vol. 7741, International Society for Optics and Photonics (SPIE), 737 – 745

Dahal, S., Amiri, M., Appel, J. W., et al. 2020, Journal of Low Temperature Physics, 199, 289

de Bernardis, P., Aiola, S., Amico, G., et al. 2012, in Society of Photo-Optical Instrumentation Engineers (SPIE) Conference Series, Vol. 8452, Millimeter, Submillimeter, and Far-Infrared Detectors and Instrumentation for Astronomy VI, 84523F

Del Torto, F., Bersanelli, M., Franceschet, C., et al. 2013, in 2013 International Conference on Electromagnetics in Advanced Applications (ICEAA), 939–941

Del Torto, F., Franceschet, C., Villa, F., et al. 2015, in 36th ESA Antenna Workshop on Antennas and RF Systems for Space Science

Dragone, C. 1978, Bell System Technical Journal, 57, 2663

Einstein, A. 1915, Sitzungsberichte der Königlich Preußischen Akademie der Wissenschaften (Berlin), 844

Fixsen, D. J. 2009, *Astrophys. J.*, 707, 916

Fixsen, D. J., Cheng, E. S., Gales, J. M., et al. 1996, The Astrophysical Journal, 473, 576

Franceschet, C. 2016, PhD thesis, University of Milan

Franceschet, C., Realini, S., Mennella, A., et al. 2018, in Proceedings of SPIE - The International Society for Optical Engineering, Vol. 10708

Friedman, A. 1922, Zeitschrift für Physic, 10, 377

Gorski, K. M., Wandelt, B. D., Hansen, F. K., Hivon, E., & Banday, A. J. 1999, arXiv e-prints, astro

Gualtieri, R., Filippini, J. P., Ade, P. A. R., et al. 2018, Journal of Low Temperature Physics, 193, 1112

Guth, A. H. 1981, Physical Review D, 23, 347

Hivon, E., Górski, K. M., Netterfield, C. B., et al. 2002, *Astrophys. J.*, 567, 2

Hubble, E. 1929, Proceedings of the National Academy of Sciences, 15, 168

IEEE Std 145-2013. 2014, IEEE Standard for Definitions of Terms for Antennas, 1

Jackson, J. D. 1975, Classical electrodynamics; 2nd ed. (New York, NY: Wiley)

Kamionkowski, M., Kosowsky, A., & Stebbins, A. 1997, *Phys. Rev. D*, 55, 7368

Kamionkowski, M. & Kovetz, E. D. 2016, Annual Review of Astronomy and Astrophysics, 54, 227

Kovac, J. M., Leitch, E. M., Pryke, C., et al. 2002, *Nature*, 420, 772

Kraus, J. 1984, Radio astronomy (Cygnus-Quasar Books)

Kraus, J. D. & Marhefka, R. J. 2001, Antennas (3rd edition) (McGraw-Hill Education Singapore, U.S.A.)

Lewis, A. & Challinor, A. 2011, CAMB: Code for Anisotropies in the Microwave Background

Ludwig, A. C. 1973, IEEE Transactions on Antennas and Propagation, 21, 116

Nielsen, P. H. 2000, Manual for multi-reflector gtd (Ticra)

North, C. E., Johnson, B. R., Ade, P. A. R., et al. 2008, arXiv e-prints, arXiv:0805.3690

Planck Collaboration, Adam, R., Ade, P. A. R., et al. 2016, *Astron. Astrophys.*, 594, A9

Planck Collaboration, Aghanim, N., Akrami, Y., et al. 2018a, arXiv e-prints, arXiv:1807.06209

Planck Collaboration, Akrami, Y., Arroja, F., et al. 2018b, arXiv e-prints, arXiv:1807.06205

Polarbear Collaboration, Ade, P. A. R., Akiba, Y., et al. 2014, *Astrophys. J.*, 794, 171

Pontoppidan, K. 2008, GRASP Technical Description (Ticra)

Reichborn-Kjennerud, B., Aboobaker, A. M., Ade, P., et al. 2010, in Society of Photo-Optical Instrumentation Engineers (SPIE) Conference Series, Vol. 7741, Millimeter, Submillimeter, and Far-Infrared Detectors and Instrumentation for Astronomy V, 77411C

Reinecke, M., Dolag, K., Hell, R., Bartelmann, M., & Enßlin, T. A. 2006, *Astron. Astrophys.*, 445, 373

Robertson, H. P. 1935, *Astrophys. J.*, 82, 284

Rybicki, G. B. & Lightman, A. P. 1979, Radiative processes in astrophysics

Sandri, M. 2005, PhD thesis, University of Padua

Sandri, M., Villa, F., & Valenziano, L. 2012, in *Proc. SPIE*, Vol. 8449, Modeling, Systems Engineering, and Project Management for Astronomy V, 84491R

Silk, J. 1968, The Astrophysical Journal, 151, 459

Suzuki, A., Ade, P. A. R., Akiba, Y., et al. 2018, Journal of Low Temperature Physics, 193, 1048

Tartari, A., Aumont, J., Banfi, S., et al. 2016, Journal of Low Temperature Physics, 184, 739

Thornton, R. J., Ade, P. A. R., Aiola, S., et al. 2016, The Astrophysical Journal Supplement Series, 227, 21

Virone, G., Peverini, O. A., Lumia, M., Addamo, G., & Tascone, R. 2014, IEEE Transactions on Microwave Theory and Techniques, 62, 1487

Wald, R. M. 1984, General relativity (Chicago, IL: Chicago Univ. Press)
Walker, A. G. 1937, Proceedings of the London Mathematical Society, 42, 90
Wilson, M. L. & Silk, J. 1981, *Astrophys. J.*, 243, 14
Zaldarriaga, M. & Seljak, U. 1997, *Phys. Rev. D*, 55, 1830

List of Publications

As of 15th September 2020

Refereed publications
Lamagna, L. et al. “Progress Report on the Large-Scale Polarization Explorer.” Journal of Low Temperature Physics (2020).
Sugai, H. et al. “Updated Design of the CMB Polarization Experiment Satellite LiteBIRD.” Journal of Low Temperature Physics 199.3-4 (2020): 1107–1117.
Realini, S., Franceschet, C. and Mennella, A. “Modelling the Radiation Pattern of a Dual Circular Polarization System.” Journal of Instrumentation (2019).

Publications under review
The LSPE Collaboration “The large scale polarization explorer (LSPE) for CMB measurements: performance forecast.” submitted to JCAP (2020).

Publications in preparation
De Miguel Hernandez, J., Realini, S. andFranceschet, C. “One meta-Ring to communicate them all. A 5:1 wideband factor meta-material for applications in radioastronomy and satellite-communications.”
Realini, S. et al. “The optical system and performance of LSPE-STRIP.”

Publications in conference proceedings
Franceschet, C. et al. “The STRIP Instrument of the Large Scale Polarization Explorer: Microwave Eyes to Map the Galactic Polarized Foregrounds.” Proc. SPIE 10708, Millimeter, Submillimeter, and Far-Infrared Detectors and Instrumentation for Astronomy IX (2018).
Sekimoto, Y. et al. “Concept design of the LiteBIRD satellite for CMB B-mode polarization.” Proc. SPIE 10698, Space Telescopes and Instrumentation 2018: Optical, Infrared, and Millimeter Wave, 106981Y (2018).
Realini, S. et al. “Preliminary Analysis of the Optical System of the LSPE-STRIP Instrument.” Proceedings of the Fifteenth Marcel Grossman Meeting on General Relativity (2018).